Title

Structural Characterization and Kinetic Analysis of Formate Dehydrogenase DABG From C. Necator and Formate Dehydrogenase F From P. atrosepticum

Permalink

Author

Hakopian, Sheron

Publication Date

2023

Peer reviewed|Thesis/dissertation

UNIVERSITY OF CALIFORNIA
RIVERSIDE

Structural Characterization and Kinetic Analysis of Formate Dehydrogenase DABG
From *C. Necator* and Formate Dehydrogenase F From *P. atrosepticum*

A Dissertation submitted in partial satisfaction
of the requirements for the degree of

Doctor of Philosophy

in

Environmental Toxicology

by

Sheron Hakopian

June 2023

Dissertation Committee:

    Dr. Russ Hille, Chairperson
    Dr. Gregor Blaha
    Dr. Jikui Song

The Dissertation of Sheron Hakopian is approved:

_____

_____

_____

Committee Chairperson

University of California, Riverside

Acknowledgment

First and foremost, I would like to express my deepest gratitude and appreciation to my Ph.D. advisor, Dr. Hille, for his invaluable guidance, support, and mentorship throughout my doctoral journey. His unwavering commitment to academic excellence and his expertise in the field have been instrumental in shaping my research and personal growth. His patience, empathy, and support has been invaluable in helping me overcome challenges, both academically and personally. I am truly grateful for their genuine belief in my potential and their continuous encouragement.

I would like to extend my sincere appreciation and gratitude to my committee members, Dr. Blaha and Dr. Song. His support has greatly enhanced both my research endeavors and personal development. I also acknowledge and appreciate the collaborative atmosphere.

I am grateful to Dimitri Niks for the exceptional assistance and valuable advice as well as Dr. Dingwall and Dr. Debus for their continued support and encouragement.

I would also like to extend my heartfelt gratitude to my lab mates, Wayne, Jessica, Steve (Ortiz), Kevin and Derek, our postdoctoral researchers, Snow, Sophie, Duo and Alex as well as my previous lab mates, Adam, Steve (Diggs), Tim, Tynan, Jian, Jiuwei, Wendan, Box and Li Fang. Their constant support, stimulating discussions, and collaborative spirit have greatly enriched my research experience. I am grateful for the countless hours spent together in the lab, sharing ideas, troubleshooting experiments, and providing valuable feedback. Lastly, I am grateful for the enduring friendships that were forged during our

time together. The bonds we formed have transcended the boundaries of the lab, and I cherish the connections we have made.

The text of this dissertation, in part, is a reprint of the material as it appears in "The air-inactivation of formate dehydrogenase FdsDABG from *Cupriavidus necator*", June 2022 and "Crystallographic and kinetic analyses of the FdsBG subcomplex of the cytosolic formate dehydrogenase FdsABG from *Cupriavidus necator*", May 2020. The co- authors Dr. Russ Hille, Dr. Blaha and Dimitri Niks listed in these publications directed and supervised the research which forms the basis for this dissertation. The co-author Dr. Young conducted the X-ray crystallography data curation, analysis, and visualization in the second manuscript mentioned above.

Dedication

To my parents and my beloved hamster, Michiko

If we knew what it was, we were doing,

it would not be called research, would it?

Albert Einstein

ABSTRACT OF THE DISSERTATION

Structural Characterization and Kinetic Analysis of Formate Dehydrogenase DABG
From *Cupriavidus Necator* and Formate Dehydrogenase F From *Pectobacterium
Atrosepticum*

by

Sheron Hakopian

Doctor of Philosophy, Graduate Program in Environmental Toxicology
University of California, Riverside, June 2023
Dr. Russ Hille, Chairperson

Carbon dioxide (CO_2) is a potent greenhouse gas that has been building up in the
Earth's atmosphere since the beginning of the industrial revolution, resulting in
anthropogenic climate change that constitutes an existential threat to human society.
Adoption of renewable energies alone is likely to be insufficient to tackle this threat and
current methods of capturing CO_2 rely on the challenging and costly practice of burying
trapped CO_2 underground. In recent years, biological systems that can capture and convert
CO_2 to a much more practical compound have been the focus of many studies.
Molybdenum-containing formate dehydrogenases are very interesting as they interconvert
CO_2 with the so-called feedstock chemical formate. Elucidation of the highly efficient
catalytic mechanism by which enzymes catalyze this interconversion under mild conditions
is expected to lead to the development of new bio-inspired catalysts, providing a means to

effectively capture CO_2. Moreover, such catalysts will lead to an attractive means to store energy in the form of chemical bonds.

In the present work, the structure and function of the FdsDABG formate dehydrogenase from *Cupriavidus necator*, a cytosolic NAD^+-dependent enzyme, and the FdhF formate dehydrogenase from *Pectobacterium atrosepticum,* an NAD^+ independent formate dehydrogenase also found in the cytosol, have been investigated. Various techniques have been employed, including kinetic steady-state assays, rapid reaction kinetics, X-ray crystallography, electron paramagnetic resonance, extended X-ray absorption fine structure and electrochemical methods to investigate these formate dehydrogenases.

This work has revealed that for FdsDABG, acid/base catalysis does not have a significant impact on the mechanism of formate oxidation, consistent with this enzyme specifically catalyzing a hydride transfer reaction utilizing CO_2 as the substrate for reverse catalysis. In addition, inactivation of FdsDABG in air is shown to occur through a superoxide-mediated process which can be prevented by superoxide dismutase. X-ray crystal analysis of FdsBG has yielded information regarding the position and arrangement of its redox-active cofactors, including details of the NAD^+/NADH binding site. Finally, UV/Visible absorption and formate reduction experiments of FdhF confirm the recombinant enzyme's functionality and provide insights on how the electron transfer process occurs between the molybdenum center and its sole iron-sulfur cluster.

The robust findings of our investigations provide compelling evidence supporting a hydride transfer mechanism for molybdenum containing formate dehydrogenases.

Table of Contents

List of Figures

List of Tables

Chapter 1

Introduction

1.1. General background

1.1.2. Climate crisis on Earth

In 1988, climate scientists testified to the U.S. Congressional committee that increasing global temperatures were not natural but caused by the anthropogenic accumulation of greenhouse gases, mainly carbon dioxide (CO_2). In the early 1990s, reports in the scientific literature began mentioning the disastrous consequences of climate change and the many potentially catastrophic results it could have. It is not the survival of the planet Earth that is in question but the survival of a highly functioning civilization, a society with improved health conditions (Butler 2018).

Industrial lifestyle and human activities have accelerated the climate change gradually over decades. The general definition of climate change is progressive changes in the typical weather of a region. Nowadays, it has been taken to refer to the annual incremental increase in the average surface temperature. The terms climate change, global warming or even climate emergency are used more often in daily coverage by media and news outlets. Climate change has had a significant impact on planet Earth. Some of the major effects are retreat of mountain glaciers, loss of polar ice, rising temperatures in oceans with associated effects on weather patterns, and greater risk of flood in low-lying countries. In addition to these, rising sea levels contaminate drinking wells and rivers with salt and pose a serious threat to coastal communities worldwide (Santos and Bakhshoodeh 2021).

1.1.3. Causes of Climate change

Both natural and anthropogenic factors drive climate change. Natural factors include phenomena such as volcanic eruptions, forest fires and so on. Anthropogenic factors include burning of fossil fuels, clearing of rainforests and other man-made phenomena. The two cardinal culprits of the anthropogenic component of global warming are the greenhouse gases carbon dioxide and methane, which trap infrared radiation from the sun in the atmosphere. Methane is the more potent greenhouse gas, but its lifetime in the atmosphere is much shorter than CO_2. Together, billions of tons of anthropogenic carbon go into the atmosphere each year (Thompson, n.d.).

The prominent and urgent goal is to reduce emissions of greenhouse gases, and there are two main strategies to achieve this aim. The first is to replace fossil fuels with renewable green energy sources and the second is to develop atmospheric carbon capturing methods to lower the CO_2 levels (Santos and Bakhshoodeh 2021). Regarding the former strategy, fundamental changes are needed in our culture, technology, politics, and ecosystems to develop and deploy green energy. For the latter, there are several techniques currently being employed which will be discussed later in this study. Figure 1 depicts the different sources of greenhouse gases.
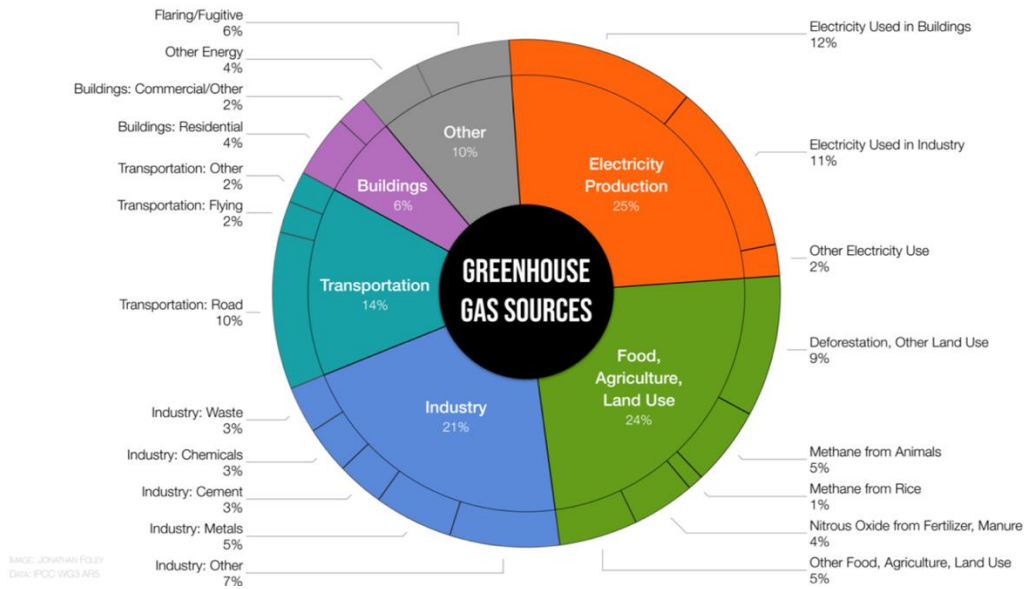
Figure 1. Sources of emission of greenhouse gases. Surprisingly transportation is in the third place while production of electricity and agriculture, although very close, occupying the first and second places respectively (Mailloux et al. 2021).

One of the first issues to address is how to maintain and enhance already existing carbon sinks such as forests, particularly tropical rainforests (Mailloux et al. 2021). Figure 2 shows some of the solutions to this crisis in terms of prevention and improvement of the situation (Mailloux et al. 2021).
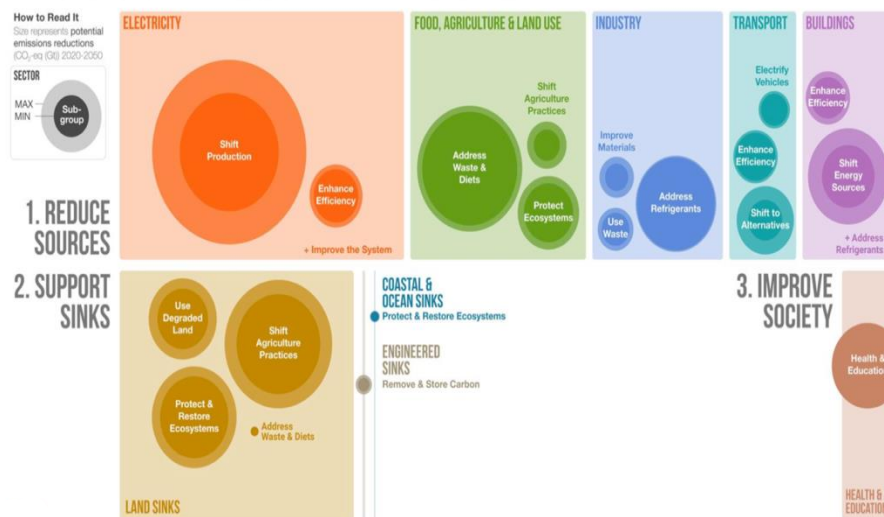
Figure 2. Approaches to reduce the sources of CO_2 emissions and support carbon sinks. One of the principal actions to take is to shift the way we produce electricity (Mailloux et al. 2021).

1.1.4. CO₂ capturing strategies

Another possible solution to this crisis, augmenting reduced production of greenhouse gases, is the large-scale removal of CO_2 from the atmosphere, a strategy recommended by virtually every Intergovernmental Panel on Climate Change (IPCC).

Capturing CO_2 is not a new idea. It has long been recognized that plants, soils and the oceans consume approximately 20% of anthropogenic CO_2 emissions (Griscom et al. 2017). A variety of technologies are being utilized to sequester CO_2 from the atmosphere or to capture it before being released to the atmosphere. These technologies are classified into three main groups based on the time point of capturing CO_2: 1. Pre-combustion 2. Post-combustion and 3. Oxy combustion (Khosroabadi et al. 2021).

1.1.4.1. Pre-combustion

This method involves, as the name suggests, separation of CO_2 prior to combustion. The fuel, coal or biomass, which is the source of carbon, is first heated to 1000-1700°C in the presence of steam and oxygen, followed by gas production in a gasifier under elevated levels of pressure. The gas produced in this step is called syngas which consists of hydrogen and carbon monoxide. A multi-step process converts the syngas to only hydrogen and CO_2 accompanied by steam. Finally, wet gas scrubbers separate the CO_2 from hydrogen (Kammerer et al. 2022).

1.1.4.2. Post-combustion:

In post-combustion processes, a cleansing step is added to the overall workflow in a power plant, utilizing solvents or solid scrubbers to sequester CO_2. CO_2 bound to the scrubbers can subsequently be removed by heating, utilized in other industrial processes or

stored. There are also gas-permeable membranes that can be utilized in this method (Kammerer et al. 2022). Currently, the solvent-based method is mainly used in fossil fuel applications, and is able to sequester most of the CO_2 generated (Kammerer et al. 2022). On the other hand, solid scrubbers are better suited for treatment of gases emitted from power station smokestacks as they have a much higher capacity to capture CO_2 as well as higher speed in absorption which is more fitting for industrial levels. The current most common post-combustion methods are direct air capture and carbon capture and utilization; both are discussed below in more detail.

Direct air capture (DAC):

This method operates based on selective chemical reactions pulling and trapping CO_2 directly from the air. It operates by employing liquid solvents or solid adsorbents. This is a better method in terms of no need for transferring large amounts of CO_2 from converters. Meaning, it can process CO_2 right after capture from any source, in any location, making it a very flexible and scalable method. One other advantage of DAC is that unlike other methods, it can reduce the CO_2 growth rate in the atmosphere alongside targeting significant sources. Although, it is still not a feasible approach as it is not that cost-effective. (Khosroabadi et al. 2021).

Carbon capture and utilization (CCU):

This procedure captures CO_2 and converts it to a raw carbon material such as chemical feedstocks (Styring et al. 2011). In other terms this technique turns CO_2 to a renewable source of energy source. Therefore, with this way of approach CO_2 can be a great replacement for conventional petrochemical feed materials. Although it requires an

additional step, hydrogenation, which as of today, the energy needed for that step exceeds the benefits (Khosroabadi et al. 2021).

1.1.4.3. Oxy-combustion

This process is also a post-combustion method, although it is different from a regular post-combustion method as it is applied in the oxygen atmosphere. The exhaust of this process is a mixture of CO_2, water vapor, and other components like SO_2. The vapor gets taken care of by condensation and additional cleaning steps to remove the SO_2. CO2 is captured and processed via post-combustion methods after the procedures mentioned above. The method retains all the CO_2 but unfortunately it is very energy- and cost-intensive (Kammerer et al. 2022).

There are myriad techniques to capture CO_2 in each of the above time points. One of them is by direct absorption, in which a liquid or solid acts as adsorbent and removes CO_2. This technique is divided into two categories based on the absorbent, chemical and physical absorption.

Chemical absorption:

This is a common method in post-combustion applications and involves a liquid absorbent separating the CO_2. One of the significant advantages of this method is that after the capture the product is CO_2 with high purity, meaning no other side compounds get captured. Hence, any further purification steps after capture get eliminated from the procedure and the captured CO_2 can be removed from the absorbent and stored. However, the maintenance and regeneration is very energy intensive (Kammerer et al. 2022).

Amine scrubbing is an examples of a chemical absorption method for separating and capturing CO_2. The main amines used in this method are monoethanolamine (MEA) and methyldiethanolamine (MDEA). This method also requires high pressures for operation. The gas is compressed then gets sprayed with droplets of amine absorber. The CO_2 undergoes a chemical reaction which results in binding to the amine compounds. To release the CO_2, the mixture is heated and decompressed, with the amine being recycled for another wash. This method works best when CO_2 is the major component of the gas being treated. High levels of nitrogen oxides or sulfurous gases reduce the efficiency of the amine scrubbers. In these cases, an extra purification step is required to remove these gases. Given that compounds like MDEA are kinetically not that efficient reacting with CO_2, another chemical activator, piperazine can be added to improve the yield. There are other alternatives for chemical absorption, for instance, amino acid salts or carbonates. For amino acids, strong bases like sodium or potassium hydroxide are required to neutralize and thus increase their solubility. With carbonates, the rate of the reaction is limited by the formation of hydrogen carbonate. Unfortunately, this process also requires high temperature and pressure. One last option for chemical absorption is ammonia which has the advantage of working at low temperature while absorbing CO_2, although regeneration is costly because high temperatures are required (Kammerer et al. 2022).

Physical absorption:

This way of removal takes place mostly in the pre-combustion stage and involves Van der Waals interactions. These interactions are not as strong as chemical bonds and are thus reversable and can be managed by changing pressure and temperature. The gas needs

to be dissolved in liquid, which demands high pressure, and is then washed with different detergents. One of the common physical absorbents is Selexol, the dimethyl ether of polyethylene glycol, which has the advantage of being highly energy efficient. However, it is ineffective in capturing CO_2 when the hydrocarbon content in gas is high. Another option is Rectisol, which does not have the limitation of Selexol but requires very low temperatures which can be energy-intensive (Kammerer et al. 2022).

Gas-solid reactions:

This is by far the most well-known method and involves the application of metal oxides such as zeolites or other metal organic frameworks (MOFs) to adsorb CO_2. MOFs are hydrocarbon frameworks with incorporated metal ions that impart selectivity (Kammerer et al. 2022). MOFs contain metal ions within an organic framework. Physically, they are crystalline and porous and very adjustable since the size, selectivity, even the pore shapes can all be tailored to a specific function. MOFs have high surface areas and modular compositions, but they do have disadvantages such as low stability, both chemically and physically. Accessing the active site of a MOF can also be challenging. Another specific issue in the synthesis and design of MOFs is optimizing the size and shapes of pores, a largely empirical process. Moreover, for MOFs to be selective when it comes to separating gases, a great level of precision is needed in the size exclusion selectivity of the pores, a non-trivial challenge to overcome (Wu and Lou 2017).

1.1.4.4. Bacteria

Many bacteria are able to fix CO_2 and can be useful in regard to capturing CO_2. One example is *Bacillus mucilaginosus* that possesses a carbonic anhydrase that can

convert CO_2 to bicarbonate which can be processed or stored. In *Escherichia coli*, the formate hydrogen lyase complex, and specifically its formate dehydrogenase component, FdhF, which can convert CO_2 and H_2 into formate is another example. Hence, bacteria can be a way to reduce the levels of CO_2 in the atmosphere (Kammerer et al. 2022).

Most industrial methods mentioned above are operating under extreme temperatures, pressure levels or are very costly when it comes to regeneration, both in terms of money and energy. In addition, these methods only store CO2 there once it has been sequestered. Some industrial methods that are currently being developed aim to utilize the captured CO_2. However, all currently considered chemical step beyond the CO_2 capturing are at the moment too resource intensive to be viable on a large scale.

1.1.5. Dawn of life on Earth

Water is essential for life. It is believed that the first living organisms on Earth arose from the primordial oceans. It has been estimated that around 4.5Ga (giga annum), Earth had a stable crust and hydrosphere. One of the approaches to investigate the exact time that liquid water was found on Earth is to study zircon crystals which were formed from magma in equilibrium with the primitive mantle. These zircon crystals have a narrow $^{18}O/^{16}O$ ratio. Once these crystals' parent rocks come in contact with low temperature liquid water, there is a preferential partitioning of ^{18}O into the minerals. Hence these crystals will have higher amounts of ^{18}O. The measurements of these ratios show values indicating that there was liquid water on Earth sometime from 3.91 to 4.4Ga. Since there are no discovered zircons older than 4.4Ga, there is no evidence that water existed prior to that time. The first living organisms on Earth must have arisen sometime after 4.4Ga (Pearce et al. 2018).

There are two prominent schools of thought regarding the origin of life on Earth. The "metabolism first" and the "genetics first" (Jheeta 2017). The former focuses mostly on non-biological chemical reactions which are the basis of metabolic pathways and cycles that subsequently lead to the rise of genetics. The latter claims that a replicable information-carrying polymer was present at the origin of life and created the RNA world (Anet 2004). According to many scientists, Spiegelman's experiment with bacteriophage Qβ (the ability of the virus to adapt and simplify its genetic material over time under selective pressure, leading to the emergence of faster-replicating, smaller RNA molecules

known as "Spiegelman's monster") demonstrated that RNA has evolutionary capabilities and can behave in a Darwinian manner (Higgs and Lehman 2015). However, there are many that oppose this theory, arguing that RNA is too complex of a molecule to have arisen prebiotically and that its instability makes it unsuitable as a precursor to life. Other theories, for example the "proteins first" hypothesis, have also been suggested (Bernhardt 2012). To date, there is no unanimous, irrefutable theory and no definitive evidence for the existing ones as to the origins of life on Earth.

Life undoubtedly started very simple, but over the years it evolved and became more and more complex. Many complicated metabolic pathways arose, and many complicated organisms came to existence. Nevertheless, they all came from the same root, the last universal common ancestor (LUCA). It must be taken into account that phylogenetic trees are ephemeral, as new data are obtained these trees are impacted and constantly "evolving" (Weiss et al. 2018).

1.1.6. The last universal common ancestor

Eukaryotes being viewed as the third domain of the tree of life, LUCA is considered to be the common ancestor of bacteria and archaea (Weiss et al. 2016). It is thought that LUCA existed roughly 3.85Ga based on carbon isotope evidence (Pearce et al. 2018). To learn about the properties of LUCA, identification of genes present in bacteria, archaea, and eukaryotes can come to our aid. In considering the distribution of genes, however, must always be borne in mind that the prevalence of some genes might be the result of

post-LUCA lateral gene transfer, which is common both within and between prokaryotic domains (Weiss et al. 2016).

On the basis of its likely metabolic capabilities, it appears that LUCA was an anaerobe. Its genes encompassed components of enzymes which metabolize carbon and nitrogen thus harvesting energy (Weiss et al. 2016). LUCA appears to have used one of the six known carbon fixation pathways called Wood-Ljungdahl pathway. Its metabolism included many oxygen-sensitive enzymes that contain iron-sulfur and other centers. The presence of carbon monoxide dehydrogenase (CODH) might indicate that LUCA could also have had heterotrophic lifestyle. The presence of reverse gyrase indicates that LUCA was a thermophile, which makes perfect sense regarding the elevated temperatures on Earth at the time that LUCA most probably arose (Weiss et al. 2018).

A diverse number of cofactor biosynthetic pathways trace back to LUCA. Pterin-containing centers are prominent, such as those found in molybdenum (Mo) and tungsten (W) containing cofactors. Iron-sulfur clusters and iron-nickel-sulfur clusters are the second most common cofactors in LUCA's proteins. Some of the important processes that iron-sulfur clusters play a significant role in are genome maintenance cofactor biosynthesis and anaerobic as well as aerobic respiration (Mayr, Mendel, and Schwarz 2021). Moreover, the abundance of transition metal- and iron-sulfur-containing proteins is evidence for a metal-rich environment, again consistent with the known geology of the early Earth (Pearce et al. 2018). The common element in these cofactors coordinated to the metal center is sulfur, which suggests that LUCA's environment was also abundant in sulfur. LUCA

utilized many of the cofactors that are being used by extant organisms, including ATP, GTP, flavin mononucleotide (FMN) as well as nicotinamide adenosine dinucleotide (NADH). Specific enzyme systems that genetically trace back to LUCA include the molybdenum- and SeCys-containing dehydrogenases, xanthine dehydrogenases, formylmethanofuran dehydrogenases, aldehyde ferrodoxin oxidoreductase, the FAD-containing subunit of NADH dehydrogenase and each of the enzymes found in the Wood-Ljungdal pathway that has been traced back to LUCA (Weiss et al. 2016). LUCA has left a clear legacy in the world of enzymology, and we have the chance to study them and effectively travel back in time.

1.1.7. The chemistry of molybdenum

The element molybdenum was first discovered in the form of molybdenite (MoS_2). Peter J. Hjelm isolated it and called it molybdenum from the Greek word, molybdos which means lead-like (Iobbi-Nivol and Leimkühler 2013). Molybdenum is a transition metal located in the second row of the periodic table, period 6 group 5 with an atomic number of 42 and atomic weight of 95.94 amu. According to PubChem compound summary, it doesn't occur in pure metallic form but rather as oxide or sulfide complexes. Its electronic configuration $[Kr]4d^55s^1$ allows it to possess a relatively decent range of oxidation states from -2 to +6 (Kim et al. 2023). Biologically, this element is prominent as a biocatalyst in molybdoproteins, such as the DMSO reductase, xanthine oxidase, sulfite oxidase, aldehyde ferredoxin oxidoreductase and nitrate reductase families (Kisker, Schindelin, and Rees 1997). Table 1 shows the families and the organisms containing these enzymes. On

the other hand, in humans, there are only four types of molybdenum possessing enzymes known to exist, xanthine oxidoreductase, aldehyde oxidase, sulfide oxidase and the mARC system which is very recent discovery (Russ Hille, Nishino, and Bittner 2011). Depending on its oxidation state, molybdenum has approximately identical affinity for oxo or sulfido ligands (Majumdar and Sarkar 2011).

Enzyme	Organism	Subunit composition
DMSO reductase family		
DMSO reductase	*Rhodobacter sphaeroides*	α
	Rhodobacter capsulatus	α
	Escherichia coli	$\alpha\beta\gamma$
Trimethylamine-N-oxide reductase	*Escherichia coli*	α
	Rhodobacter sphaeroides	α
Biotin sulfoxide reductase	*Escherichia coli*	α
Nitrate reductase (dissimilatory)	*Escherichia coli (narGHI)*	$\alpha\beta\gamma$
	Escherichia coli (narZYW)	$\alpha\beta\gamma$
	Paracoccus denitrificans (napABCD)	$\alpha\beta\gamma\delta$
Formate dehydrogenase	*Escherichia coli (fdnGHI)*	$\alpha\beta\gamma$
	Escherichia coli (fdoGHI)	$\alpha\beta\gamma$
	Wolinella succinogenes	$\alpha\beta\gamma$
Formate dehydrogenase (W containing)	*Clostridium thermoaceticum*	$\alpha_2\beta_2$
N-formylmethanofuran dehydrogenase (W containing)	*Methanobacterium wolfei*	$\alpha\beta\gamma$
Xanthine oxidase family		
Xanthine oxidase/dehydrogenase	*Bos taurus*	α_2
	Homo sapiens	α_2
	Gallus gallus	α_2
Aldehyde oxidase	*Homo sapiens*	α_2
	Oryctolagus cuniculus	α_2
Aldehyde oxidoreductase	*Desulfovibrio gigas*	α_2
Sulfite oxidase family		
Sulfite oxidase	*Homo sapiens*	α_2
	Rattus norvegicus	α_2
	Gallus gallus	α_2
	Thiobacillus novellis	α
Nitrate reductase (assimilatory)	*Neurospora crassa*	α_2
	Chlorella vulgaris	α_4
	Spinacea oleracea	α_2
Aldehyde ferredoxin oxidoreductase family		
Aldehyde ferredoxin oxidoreductase	*Pyrococcus furiosus*	α_2
Formaldehyde ferredoxin oxidoreductase	*Pyrococcus furiosus*	α_4
Glyceraldehyde-3-phosphate ferredoxin oxidoreductase	*Pyrococcus furiosus*	α
Carboxylic acid reductase	*Clostridium formicoaceticum*	α_4
Aldehyde dehydrogenase	*Desulfovibrio gigas*	α_4
Hydroxycarboxylate viologen oxidoreductase	*Proteus vulgaris*	α_8

Table 1. Representatives of molybdenum containing enzymes (Kisker, Schindelin, and Rees 1997).

16

1.1.8. Molybdenum in biology

Molybdate salts are very soluble in water making molybdenum the most abundant transition metal in oceans and seawater. Hence, molybdenum is readily available to biological systems despite the fact that it constitutes a minor portion of Earth's crust. Another transition metal required by life forms is tungsten which lies immediately below molybdenum in the periodic table (Russ Hille 2002). Hot springs and hydrothermal vents contain high concentrations of tungsten. Solubility of molybdenum and tungsten depends on the oxidation state of the metal, and thus the reduction potential of the mineral-forming solution. Tungsten is soluble in the form of WS_4^{2-} or WO_4^{2-} whereas molybdenum precipitates in sulfur-rich environments in the form of MoS_2. Under physiological conditions, molybdenum and tungsten are redox-active ranging between IV and VI (Russ Hille 2002). Bortels discovered the first biological function of molybdenum, being involved in fixation of nitrogen. Molybdenum is the only 4d transition metal required by biological systems that executes prominent transformations in the metabolism of nitrogen, sulfur and carbon compounds (Iobbi-Nivol and Leimkühler 2013).

1.2. Molybdenum enzymes

The versatile redox chemistry of molybdenum is taken advantage of in enzymes depending on it. With the right environmental conditions, these enzymes can catalyze two-electron oxidation/reduction reactions. The regeneration step of the active site sometimes results in a paramagnetic Mo(V) intermediate, which is EPR (electron paramagnetic resonance) active. Molybdenum containing enzymes are widely distributed in biology, a

notable exception being members of the genus *Saccharomyces (Schwarz, Mendel, and Ribbe 2009).* Molybdenum enzymes have significant roles in both eukaryotes and prokaryotes. Xanthine oxidase, aldehyde oxidase, nitrate reductase, and sulfite oxidase are prominent enzymes from eukaryotic sources, the first two catalyzing the hydroxylation of carbon centers and the last two a simpler oxygen atom transfer (Russ Hille, Nishino, and Bittner 2011). In prokaryotes, once molybdenum enters the cell, there are two sorts of cofactors to be formed. One is the [$MoFe_7S_9$] cluster known as the M cluster or the FeMo cofactor. The other category is the pterin based molybdenum cofactors.

The M cluster is fundamentally different from the pterin based cofactors. In the nitrogenase, where the M cluster can be found, the molybdenum is the last component inserted and has more of an auxiliary role. First, a pair of [4Fe-4s] clusters are formed due to the interaction of NifS and NifU which will be inserted in NifB. These precursor iron-sulfurs, called the K-cluster will be fused into the L cluster by radical s-adenosylmethionine reactions. Afterwards, the L-cluster gets inserted into the NifEN and NifH with the aid of M cluster maturase which inserts the molybdenum and the homocitrate (Hu et al. 2008). In the pterin based category, molybdenum is coordinated to a pyranopterin cofactor via a dithiolene side chain and has the main role in catalysis. There are three main types in this category based on the number of pterin moieties the metal is coordinated to. The molybdopterin cofactor (MPT), which is a mononucleotide, molybdopterin dinucleotide and the bis-molybdenum guanine dinucleotide. Examples of this system would be xanthine oxidase, sulfite oxidase and DMSO reductase family of molybdenum enzymes. The first two families contain a simple MPT. On the contrary, members of the DMSO reductase

family, the molybdenum is coordinated to two pterins, each carrying a guanosine monophosphate which form a MPT-guanine dinucleotide cofactor (Schwarz, Mendel, and Ribbe 2009).

1.2.1. Biosynthesis of molybdenum cofactors

There are three steps to the biosynthesis of molybdenum cofactor: 1. Cyclization of GTP which results in the formation of cyclopyranopterin monophosphate (cPMP). This step is catalyzed by MoaA, a member of the radical SAM (S-adenosyl-L-methionine) family of enzymes, and MoaC in *E. coli (Russ Hille, Nishino, and Bittner 2011)*. 2. Sulphuration of cPMP to generate the mature pyranopterin. MPT synthase catalyzes this step. 3. Coordination of molybdate to the enedithiolate sidechain (molybdate being carried inside bacteria cells by specific high affinity transporters). The majority of molybdoenzymes in prokaryotes are members of the DMSO reductase family. These enzymes contain two of the dithiolene moieties from two equivalents of MPT that have been converted to the dinucleotide of guanosine (or, less frequently, adenosine or cytosine), forming the bis-MGD cofactor (Leimkühler 2020).

1.2.2. Insertion of cofactors into apoenzymes

In the sulfite oxidase family, the cofactor insertion is relatively straightforward and simple since it is not deeply buried in the holoenzyme. The energy needed for the necessary conformational changes is quite low. Unlike this group of enzymes, in the DMSO reductase family, the insertion is a much more convoluted process. Here, in addition to

MobA, a chaperone is needed in order to stabilize a specific apoprotein configuration before the cofactor can be inserted. In xanthine oxidase family, it is even more complicated since the channel leading to the active site is laced together by multiple polypeptide chains and appears to be too narrow to accommodate the cofactor. However, it has been found that the enzymes that sulfurate the cofactor are also responsible for the insertion of it in both prokaryotic and eukaryotic systems. The insertion happens after the sulfur has been incorporated in the cofactor. It appears that there is a highly conserved structural motif in the xanthine oxidase family that is accountable for recruiting the machinery for sulfuration in order to complete the cofactor insertion process into the apo-protein successfully (Russ Hille, Hall, and Basu 2014).

1.2.3. Mononuclear molybdenum enzymes

The molybdenum enzymes other than nitrogenase are classified into three main groups, categorized based on the structure of their metal centers: xanthine oxidase (XO), sulfite oxidase (SOx) and dimethyl sulfoxide reductase (DMSOR). Some W-containing enzymes are closely related to the DMSOR family, possessing essentially the same active site and same overall protein fold (Niks and Hille 2019). Each family of mononuclear molybdenum enzymes is considered further below.
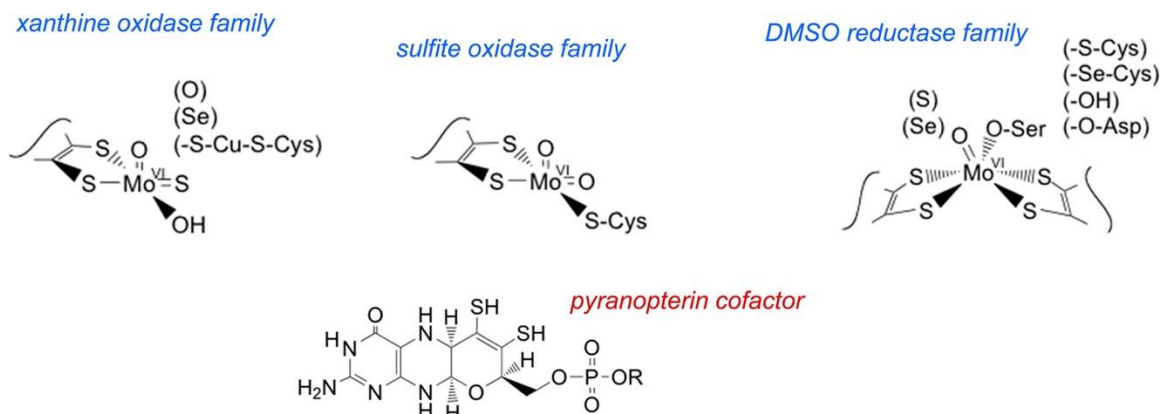
Figure 3. Active sites of the families of mononuclear molybdenum containing enzymes. From left to right, the structures of xanthine oxidase, sulfite oxidase and DMSO reductase are demonstrated. At the bottom, the pyranopterin cofactor is shown which is common among all three groups (Russ Hille, Hall, and Basu 2014).

1.2.3.1. The Xanthine oxidase Family

Xanthine dehydrogenase catalyzes the final two steps in purine metabolism, the oxidative hydroxylation of hypoxanthine to xanthine and xanthine to uric acid and is widely distributed in biology. In mammals, under certain conditions, a conformational change is induced leading to the conversion of xanthine dehydrogenase to xanthine oxidase (Russ Hille, Hall, and Basu 2014). This form of xanthine oxidoreductase's principal electron acceptor is molecular oxygen rather than NAD^+ (Okamoto, Kusano, and Nishino 2013). The X-ray crystal structure of both forms of the enzyme from bovine milk has been characterized. The enzyme is a homodimer which each monomer consisting of five domains, two domains possessing ferredoxin-like [2Fe-2S] clusters, a third domain containing FAD and two large C-terminal domains that together bind the molybdenum active site at their interface. The redox-active centers of the two monomers are well

21

insulated from one another and appear to function independently. Many bacterial enzymes of the xanthine oxidase family have heterodimers or heterotrimers with the iron-sulfur clusters and/or flavin-containing domains in separate subunits (Russ Hille, Nishino, and Bittner 2011). Specific thiols of the mammalian dehydrogenase can be oxidized to disulfides which leads to a reversible conversion of the dehydrogenase to an oxidase. Both O_2 and NAD^+ react at the FAD site of the protein, which becomes reduced as electrons are passed via the intervening [2Fe-2S] from the molybdenum center. The mechanism of xanthine oxidoreductase involves a proton abstraction of the equatorial Mo−OH followed by a nucleophilic attack on the carbon that will be hydroxylated. This step is accompanied by a hydride transfer to the Mo=S which results in the formation of a $LMo^{IV}O(SH)(OR)$ intermediate. This intermediate breaks down once the product is displaced by a hydroxide from the solvent followed by electron transfer out of the Mo center and deprotonation of the Mo−SH back to Mo=S of the oxidized enzyme (Russ Hille, Hall, and Basu 2014).

1.2.3.2. The Sulfite oxidase Family

Sulfite oxidases and dehydrogenases from eukaryotes and prokaryotes, respectively, are the second major family of molybdenum-containing enzymes, which also includes the eukaryotic nitrate reductases. These enzymes catalyze oxygen atom transfer to or from their substrates. The active site of members of sulfite oxidase family is depicted in Figure 3 and shows that they have a $LMo^{VI}O_2(S-Cys)$ coordination sphere (Russ Hille, Hall, and Basu 2014).

Chicken sulfite oxidase is the best understood enzyme of this family. As in xanthine oxidase, the oxidative and the reductive halves occur at physically separate locations in the chicken sulfite oxidase. Sulfite is reduced at the molybdenum center, with the reducing equivalents passed on to a b-type cytochrome-containing domain and on to the oxidizing substrate cytochrome *c* (Russ Hille, Hall, and Basu 2014). Both chicken and plant (*A. thaliana*) sulfite oxidases have been structurally characterized by X-ray crystallography. Despite lacking a heme domain, the molybdenum-containing domain of plant sulfite oxidase closely resembles the vertebrate sulfite oxidase. It is certainly easier to investigate the molybdenum center by studying the plant sulfite oxidase since there are no other cofactors to interfere in spectroscopic analysis (Russ Hille, Nishino, and Bittner 2011). Although the reductive half of the catalytic cycles of the plant and vertebrate sulfite oxidases proceeds essentially the same way, the oxidative half is different since there is a heme missing in the plant enzyme. The immediate product of the oxidative half in the plant sulfite oxidase is superoxide which noncatalytically disproportionates to hydrogen peroxide. The O_2 reactivity of the enzyme is unusual for this family of enzymes, and it has not been fully elucidated as to why that is. It has been noted, however, residue Tyr49 of the plant protein (a Phe in the vertebrate enzyme) with its greater polarity may influence activity (Russ Hille, Hall, and Basu 2014).

1.2.3.3. The DMSO Reductase Family

The DMSO family of enzymes are only found in bacteria and archaea and constitute an extremely diverse and widely distributed group of enzymes. More than 90% of

organisms which utilize molybdenum have enzymes of this family (Miralles-Robledillo et al. 2019). Many of these enzymes, such as the eponymous DMSO reductase, catalyze oxygen atom transfer while others catalyze reduction/oxidation, hydroxylation, and hydration.   As mentioned above, members of this family resemble those of the aldehyde:ferrodoxin oxidoreductase family of tungsten containing enzyme (Russ Hille 2002). The molybdenum center is composed of two pyranopterin molecules which are typically present as the dinucleotide of guanosine. In the molybdenum family, the metal has four sulfur ligands coming from the enedithiolates of the two equivalents of MGD, and terminal ligand which can be Mo=+, Mo=S or (rarely) Mo=Se. A final ligand comes from serine, aspartate, cysteine or selenocysteine from the polypeptide, or water/hydroxide. Depending on the amino acid, this family is categorized into type I, where cysteine or selenocysteine are coordinated to the molybdenum, aspartate is type II and serine residue brings us to type III (Miralles-Robledillo et al. 2019). The members of this family include nitrate reductases, formate dehydrogenases, trimethylamine-N-oxide reductases, DMSO reductase and biotin sulfoxide reductase.   Some of the members of this family are membrane associated whereas some are found in the periplasm and others in the cytosol (Iobbi-Nivol and Leimkühler 2013). There is a great diversity regarding the subunits contributing and cofactors which are also used to classify the members of this family. The monomeric proteins, for instance the periplasmic DMSO reductases from *R. Sphaeroides* and *R. capsulatus* have only one redox-active center, the molybdenum center. The next enzyme in terms of complexity is periplasmic formate dehydrogenase H from *E. coli*, again a monomer but in addition to the molybdenum, it contains a cubane iron-sulfur cluster as

another redox center. Then there is the formate dehydrogenase N (FdnGH) which is coexpressed with nitrate reductase (NarGH). Together, they form a respiratory chain, transferring electrons from formate to nitrate. FdnGHI possesses a bis-molybdopterin guanine dinucleotide and a [4Fe-4S] cofactor. An interesting fact about these two enzymes is that their catalytically active subunits are positioned on the opposite sides of the cell membrane resulting in NarGH being cytosolic and FdnGH being periplasmic. Finally, FdsDABG from aerobic *R. eutropha* or *C. necator*, which is a cytoplasmic NAD^+-dependent formate dehydrogenase has the greatest complexity, possessing the molybdenum center, seven iron-sulfur cluster and a flavin mononucleotide (FMN). It appears the segregation of the clades is based on number of redox centers, but it does not necessarily mean that the ligands coordinated to the molybdenum are exactly the same in one clade (Russ Hille, Hall, and Basu 2014).

1.3. Formate dehydrogenases

There are both molybdenum- and tungsten-containing formate dehydrogenases that catalyze the reversible oxidation of formate to CO_2. In this process they generate two electrons and two protons. They are distinct from the formate dehydrogenases found in many aerobic organisms, which are devoid of redox-active centers and catalyze direct hydride transfer between formate and $NAD(P)^+$. The Mo- and W-containing enzymes are typically very oxygen sensitive, although some, *e.g.*, the FdsDABG enzyme from *C. necator* or FDH2 from *Desulfovibrio vulgaris* Hildenborough are notably less so (Yu et al. 2019). Several mechanisms have been proposed for Mo and W containing formate

dehydrogenases and due to their similarities in their active sites it is expected to be able to explain that they will act via the same mechanism of action. It is clear that the mechanism these enzymes follow is not an oxygen transfer pathway since the oxygen from the solvent is not incorporated into the product CO_2. Some of the proposed mechanisms had difficulties with the pKa of the C_α proton since they were suggesting the abduction of a proton from C_α. The pKa for C_α proton is so high that it is not clear how a simple histidine or in one of the mechanisms, a dissociated SeCys would reach to that pKa to deprotonate the C_α. The X-ray crystal structure of FdhF from *E. coli* and kinetic experiments done with FdsDABG from *C. necator* have resulted in a mechanism that is now widely, if not generally, accepted, based on the experimental observation that the C_α-hydrogen of formate is transferred directly to the molybdenum center in the course of the reaction (Niks and Hille 2019). In this mechanism, as demonstrated in Figure 4, the hydrogen of the C_α is transferred via a simple hydride mechanism to the sulfido ligand coordinated to the metal center which is strongly coupled with the Mo(V) determined by EPR. This indicates that there will be a Mo−SH species formed which gives the fully reduced metal center i.e. Mo (IV) and release of CO_2. The molybdenum is subsequently reoxidized in one-electron. Formate is known for being a good hydride donor on the one hand, and the Mo=S group is known to be a good hydride acceptor on the other. A prominent point in this mechanism is the fact that throughout the entire reduction process, the molybdenum coordination sphere is stable, remaining six-coordinate, meaning that there is no dissociation of either the Mo=S or Mo−Se(Cys) ligands as claimed in other mechanisms (Niks and Hille 2019).
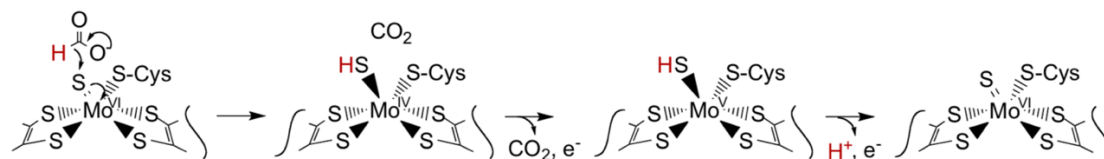
Figure 4. The hydride transfer mechanism for formate dehydrogenases. The hydrogen from C_α is transferred to the sulfido ligand attached to the metal center through a hydride process. This results in the formation of a Mo-SH species, leading to the generation of a Mo (IV) center and the release of CO2. Following this, the molybdenum is subsequently reoxidized through a one-electron process. (Yu et al. 2017).

1.3.1. FdsDABG

Cupriavidus necator (*Ralstonia eutropha*) is an aerobic facultative chemoautotrophic bacterium, capable of both lithotrophic and heterotrophic growth. The genome of this bacterium encodes four formate dehydrogenases, all of which are metal-dependent but only one, encoded by the *fdsGBACD* operon, is cytosolic (Yu et al. 2017). FdsDABG catalyzes the oxidation of formate to CO_2, reducing NAD^+ to NADH and is a member of the NADH dehydrogenase superfamily (Niks et al. 2016). It is a (FdsDABG)$_2$ dimer of tetramers, with a molybdenum center, seven iron-sulfur clusters and a flavin mononucleotide. In Figure 5, the model for FdsDABG from *C. necator*, built based on the structure of NADH dehydrogenase is depicted on the right, whereas on the left is the structure of the highly homologous FdsDABG from *Rhodobacter capsulatus* as determined by cryoelectron microscopy. FdsA, the largest subunit at 105 kDa, has a C-terminal region that exhibits approximately 60% sequence similarity to a variety of molybdenum containing formate dehydrogenases, including the highly conserved residues Cys 378 and His 379 and a [4Fe-4S] cluster. The N-terminal region of FdsA has an additional four [4Fe-4S] and one [2Fe-2S]. The 55 kDa FdsB includes the NAD^+ binding site and the FMN. The 19 kDa FdsG has one [2Fe-2S] which connects the electron pathway from the

27

FMN to the molybdenum center. FdsC is not part of the holoenzyme, but it is involved delivering freshly matured and sulfurated cofactor into the enzyme's active site. Each subunit of FdsDABG has significant sequence similarities to a corresponding subunit of NADH dehydrogenase, and the overall structures are thought to be very similar; the spatial layout of the several redox active centers is particularly highly conserved. FdsA is very similar to Nqo3 of *T. Thermophilus* NADH dehydrogenase which its structure has been crystallographically characterized. One thing to note, is that in the NADH dehydrogenase, the molybdenum center as well as one of the [4Fe-4S] in the C-terminal region of FdsA have been lost over the course of evolution. The N-terminal thioredoxin like domain of FdsB has 45% sequence similarity to the N-terminal domain of Nqo1 and the C-terminal of FdsG has 34% sequence similarity to the C-terminal of Nqo2 of the NADH dehydrogenase, respectively (Young et al. 2020).
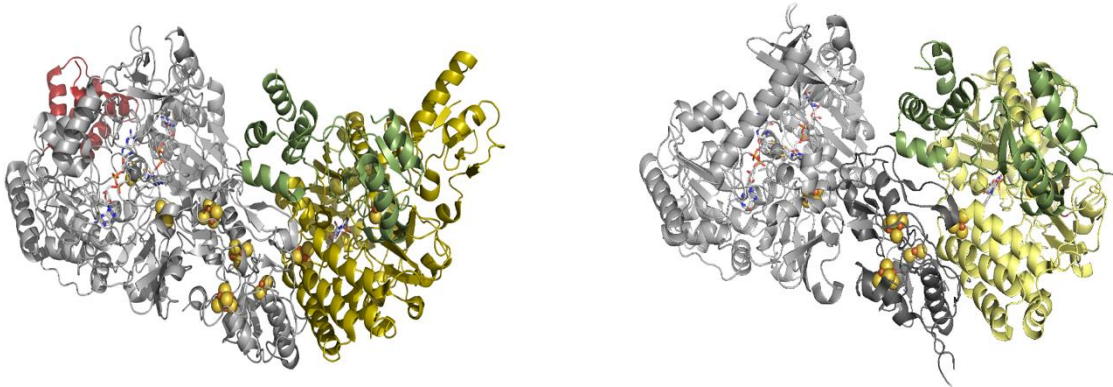
Figure 5. Structure models for FdsDABG. On the right, the model for FdsDABG structure based on the homology to the NADH dehydrogenase (Russ Hille, Hall, and Basu 2014). On the left the Cryo-EM structure of FdsDABG from *R. capsulatus* (Radon et al. 2020).

FdsDABG absorbs throughout the visible region, with a well resolved 450 nm absorption indicative of the FMN cofactor (Russ Hille, Hall, and Basu 2014). The visible absorption bleaches significantly upon reduction by formate, NADH or sodium dithionite, and the reduced enzyme exhibits multiple EPR signals. The g values for three out of the seven expected EPR signals for the iron sulfur-clusters have been reported (Niks et al. 2016).

Unlike the several membrane- or periplasm-localized formate dehydrogenases that are highly oxygen sensitive, FdsDABG is expressed under aerobic conditions. The molybdenum site in FdsDABG is of the DMSO reductase variety, with two equivalents of the pyranopterin cofactors coordinated to the molybdenum via enedithiolate side chains. The fifth position is occupied by Cys-378 with the sixth ligand being a terminal Mo=S

29

(Russ Hille, Hall, and Basu 2014); the overall geometry of the oxidized enzyme is trigonal prismatic (Niks et al. 2016). As shown in Figure 6, the oxidized enzyme has a $L_2Mo^{VI}S(S-Cys)$ structure where L is the pyranopterin cofactor. The FdsC has been shown to be a sulfurase essential for enzyme activity, delivering the mature sulfurated molybdenum cofactor to the apoenzyme. The reduced form of the enzyme is $L_2Mo^{IV}SH(S-Cys)$, with the Mo=S group becoming protonated upon reduction of the metal. FdsDABG operates via a ping-pong mechanism with a limiting rate constant at high [formate] k_{red} of 140 s^{-1} at 10°C and a $K_d^{formate}$ of 82 μM (Young et al. 2020). FdsDABG also catalyzes the reverse reaction, reduction of CO_2 using NADH as electron donor, with a k_{ox} of 10 s^{-1} and $K_M^{CO_2}$ of 2.7 mM (Yu et al. 2019).
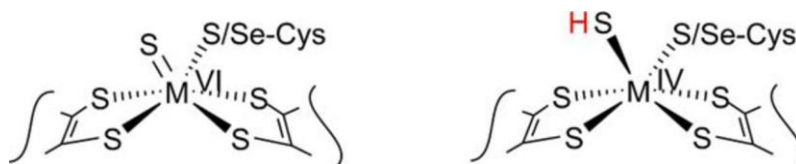
Figure 6. Mo cofactor in the active site of FdsDABG. From left to right, the oxidized and reduced states of the Mo cofactor in the active site of FdsDABG and several members of DMSO reductases.

1.3.2. FdsBG

FdsBG is a subcomplex of FdsDABG formate dehydrogenases that can be isolated separately during purification of the holoenzyme. After the first step of purification, running the supernatant through a column with beads made of streptavidin and agarose, a mixture of FdsDABG and FdsBG is loaded on TMAE, a relatively strong anion exchanger which separates the FdsBG from FdsDABG which itself gets separated in to two to three peaks with varying intensities depending on the growth conditions. The structure of FdsBG has been resolved by X-ray crystallography as demonstrated in Figure 7. The structure revealed some interesting facts about the cofactors' positions in the subcomplex. For instance, the [4Fe-4S] in FdsB and [2Fe-2S] in FdsG are closer to the FMN compared to their position in NADH dehydrogenase (Young et al. 2020).
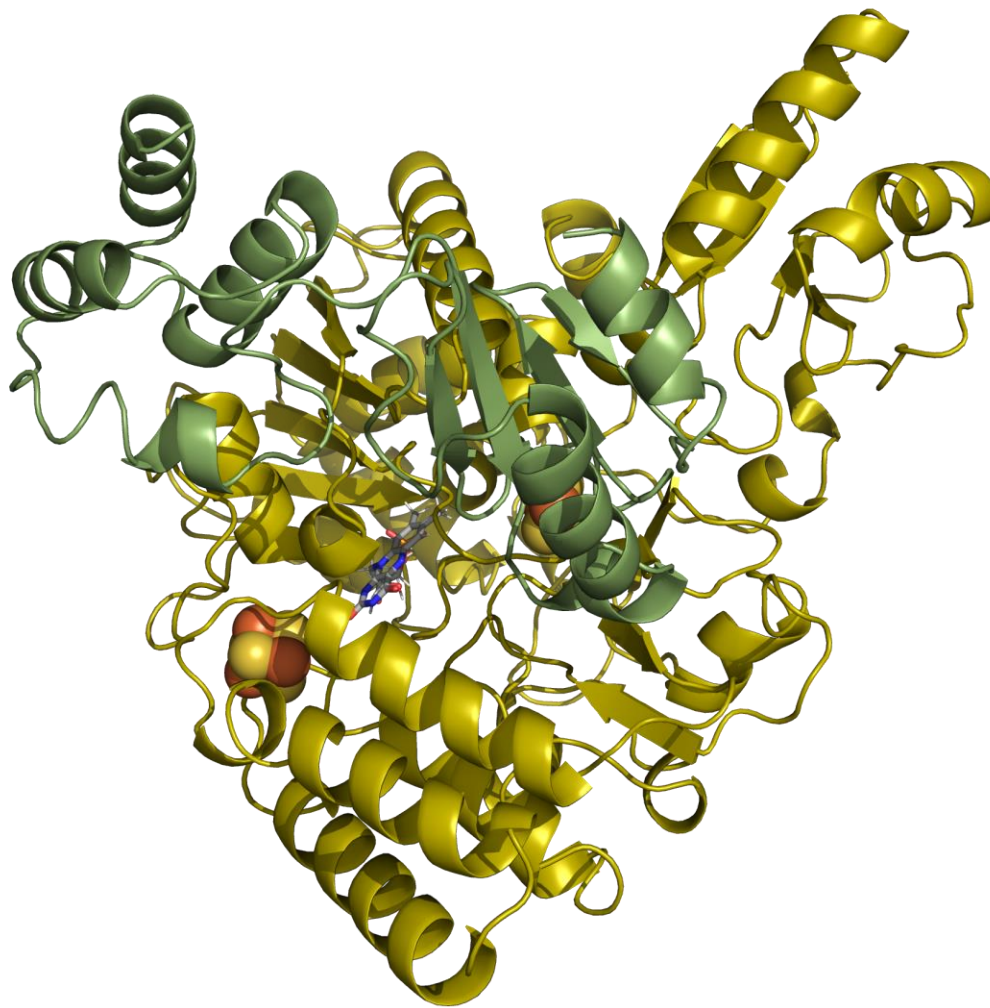
Figure 7. Protomer of FdsBG complex from *C. necator*. In yellow is the FdsB subunit containing the FMN and a cubane iron-sulfur cluster. In green is the FdsG subunit with 2Fe-2S iron sulfur cluster (PDB 6VW8) (Young et al. 2020).

32

EPR spectroscopy has been conducted to study the iron-sulfur clusters in this subcomplex. The reduced form of FdsBG only has EPR signal for the iron-sulfur clusters as the dithionite reduced hydroquinone form ($FMNH^-$) has none. FMN does not contribute any signals to the EPR spectrum of the oxidized form of FdsBG either. At liquid nitrogen temperature (80 K), there is one signal which corresponds to the [2Fe-2S] in the G subunit. At liquid helium temperatures (below 50 K) a signal is obtained which is generated by the [4Fe-4S] present in the FdsB subunit. Figure 8 illustrates the EPR spectra of FdsBG. The g values for the [2Fe-2S] are: $g1,2,3$ = 2.000, 1.948, and 1.920. The g-values for the [4Fe-4S] are $g1,2,3$ = 2.039, 1.955, and 1.891 (Niks et al. 2016).
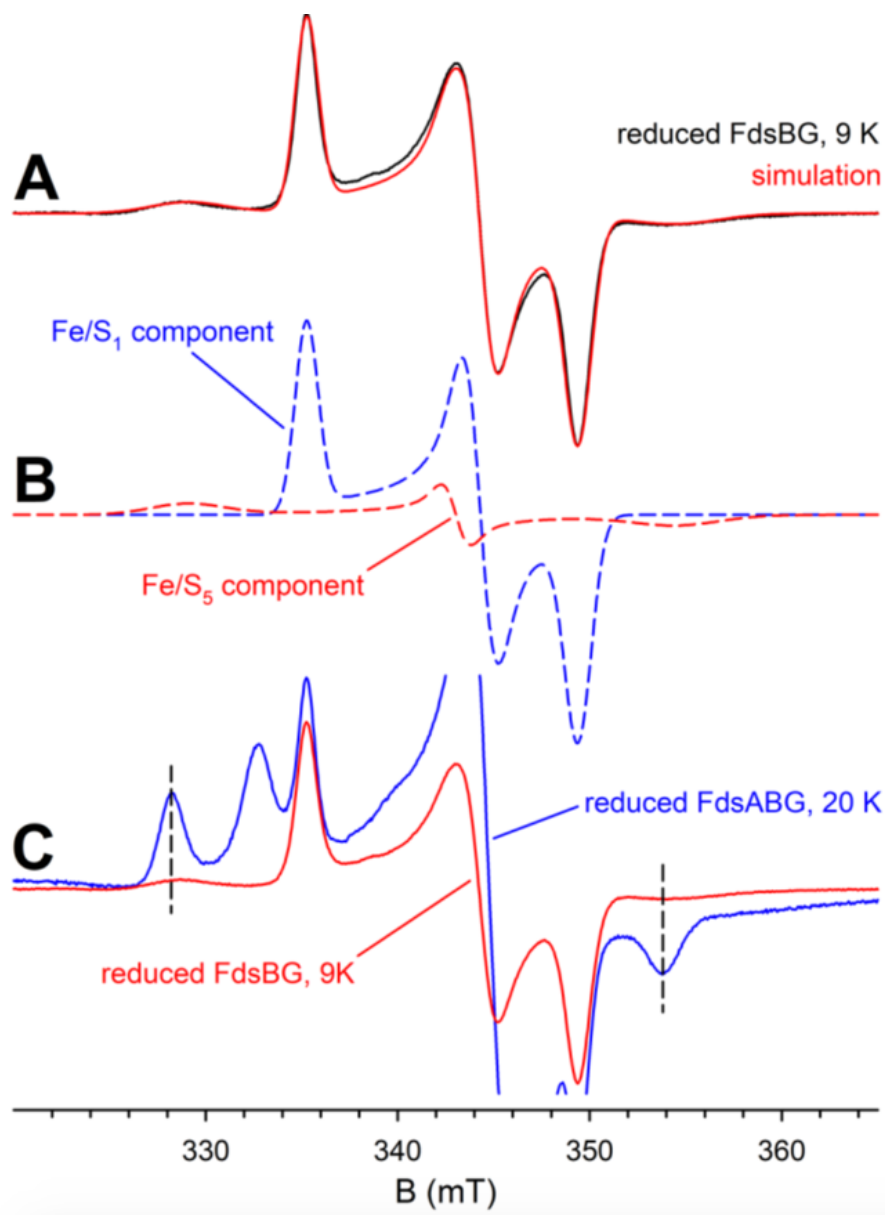
Figure 8. EPR spectra of FdsBG. In black, the observed EPR spectrum and in red the simulated spectrum of dithionite reduced iron-sulfur of 125 μM FdsBG in 100 mM K-PO$_4$, at pH 7.0. FdsBG was incubated at room temperature under anaerobic condition for an hour with 2mM of buffered sodium dithionite prior freezing. The data was collected at modulation amplitude of 8 Gauss and microwave power of 2 μW at 9 K. B. Individual components of the simulated spectra in figure A. FeS$_1$ was previously assigned (Niks 2016) in blue dash spectrum and the red dash trace represents the signal for FeS$_5$ that is only apparent in the FdsBG complex EPR spectrum. C. Graphical alignment of the red trace in A with the spectrum corresponding to dithionite reduced FdsDABG at 20 K.

34

Rapid-reaction kinetic studies have also been employed to investigate FdsBG. The electron transfer reaction of FdsBG while getting reduced by NADH was the focus of this study. It yielded a k_{red} of 680 s^{-1} at high concentration of NADH and a k_d^{NADH} of 190 μM (Figure 9).
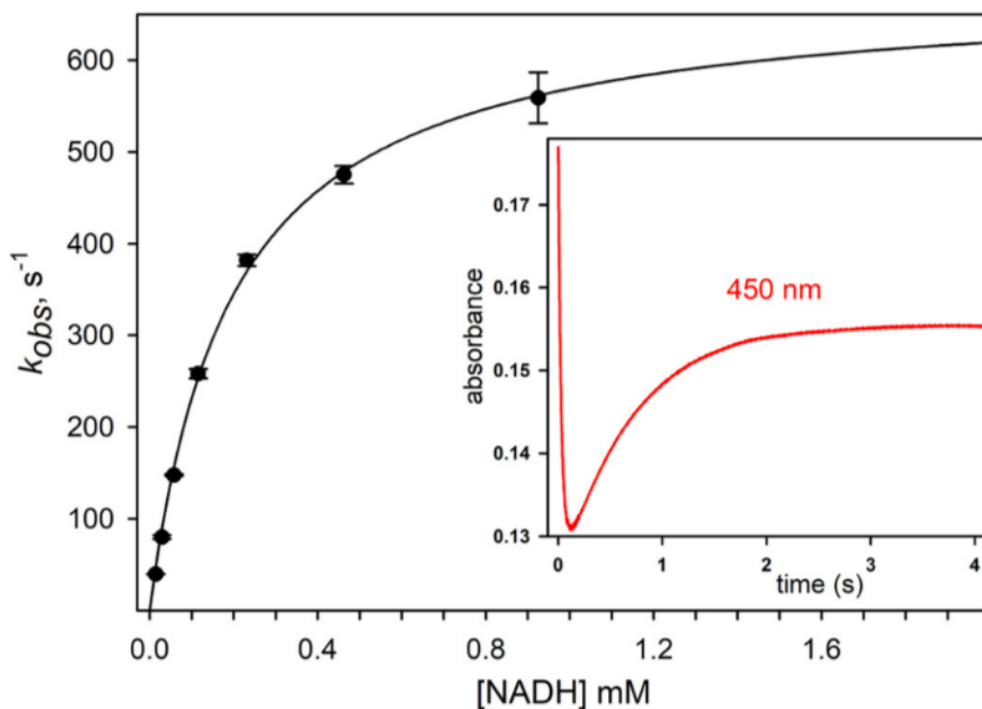
Figure 9. Rapid reaction kinetic analysis of FdsBG. Reduction of 9 μM FdsBG by 14 μM NADH was monitored at 450 nm. In black is the hyperbolic fits which resulted in k_{red} of 680 s^{-1} and a k_d^{NADH} of 190 μM. The inset represents a kinetic trace at 450 nm. The reactions were done at 5 ºC in 100 mM KPO$_4$ pH 7.0 under anaerobic condition.

1.3.3. FdhF of *Pectobacterium atrosepticum*

Polysaccharides, including pectin, contribute critically to the extracellular structure of plant cell walls. In food processing industries, it is often necessary to eliminate these pectic substances, which are degraded by pectolytic enzymes. These enzymes vary based on their substrate specificity, and are obtained from a variety of plants and microorganisms

(Naidu and Panda 1998). In tropical areas the main reason of tuber and stem rot in potatoes are soft rotting pectinolytic enterobacteria. There are two major groups of these type of bacteria. Strains formerly classified under *Erwinia carotovora* are assigned to the *Pectobacterium* and the ones described by *Erwinia chrysanthemi* are assigned to the genus *Dickeya* (Ngadze et al. 2012). Historically, *Pectobacterium atrosepticum* was considered the main pathogen causing black leg disease in potatoes. Recently, it has been known that there are many species and subspecies of *Pectobacterium* that induce the rotting of stems in plants, specifically potatoes. For instance, *P. carotovorum* subsp. *Brasiliensis* in Brazil, Israel, Netherlands, Canada, South Africa, New Zealand, and Zimbabwe and *P. wasabiae* in United states, Iran, South Africa and New Zealand were major causes of black leg potato outbreaks in those countries. Studies have shown that these different *Pectobacterium* species may share common virulence determinants which cause stem infection (Panda et al. 2016).

   Pectobacterium atrosepticum SCRI1043 is a Gram-negative enterobacterium. Genomic analysis has reported that under anaerobic conditions in this bacterium, genes for respiration and fermentation are being expressed. When *P. atrosepticum* is under respiratory conditions, same as in other model bacteria studied so far such as *E. coli*, endogenously produced formate acts as an electron donor. Although, in fermentation mode, excess amount of formate gets accumulated in the extracellular region and drops the pH as a consequence. A formate re-uptake is necessary to go back to normal condition which induces the production of formate hydrogen lyase complex (FHL). Understanding the function of FHL complex is crucial since it is responsible for providing almost all the

H_2 generated during glucose fermentation by *P. atrosepticum*, *E. coli,* and related species (Finney et al. 2019).

FHL disproportionates the excess formate from mixed-acid fermentation into H_2 and CO_2, according to the reaction below (McDowall et al. 2014) :

$$HCOO^- \rightarrow CO_2 + H^+ + 2e^- \ (E_0' = +432 \text{ mV})$$

$$H^+ + 2e^- \rightarrow H_2 \ (E_0' = -414 \text{ mV})$$
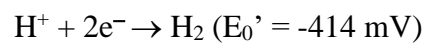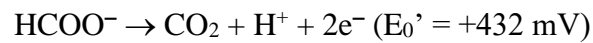
Figure 10 demonstrates a predicted structure for FHL in *E. coli*. This figure illustrates an assembly of proteins including the one being investigated in this study, formate dehydrogenase F (FdhF). FdhF (a molybdenum dependent formate dehydrogenase and HycE (a [NiFe] hydrogenase) are involved in the reaction above.
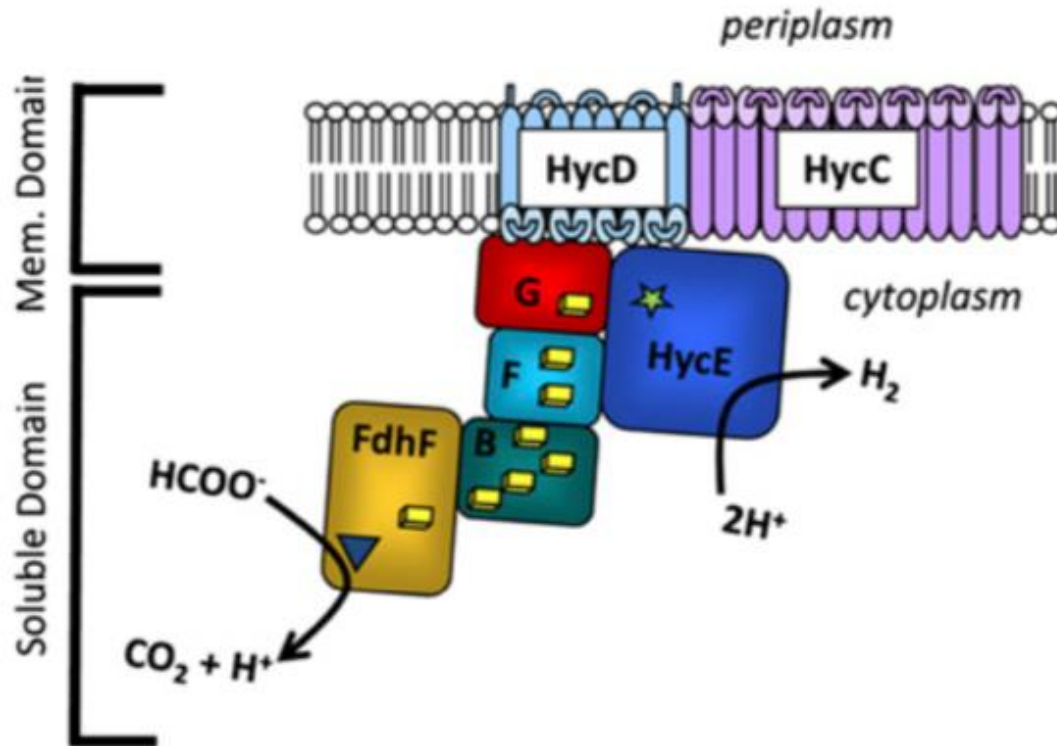
Figure 10. Predicted architecture of formate hydrogen lyase complex (FHL). FdhF and HycE disproportionate excess formate to H_2 and CO_2 (McDowall et al. 2014)

Like the molybdenum center of FdsDABG, the molybdenum or tungsten centers of the formate dehydrogenases F as well as formylmethanofuran dehydrogenases are coordinated to two pyranopterin cofactors, now referred to as metallopterin , elaborated as the dinucleotide of guanine (Russ Hille, Hall, and Basu 2014). Some of these enzymes utilize tungsten rather than molybdenum and some have selenocysteine rather than cysteine coordinated to the metal. Regardless, the overall protein folds of the subunits possessing

the Mo/W centers are virtually identical and all include the terminal sulfido ligand which is essential for catalytic activity.

At present these enzymes can be categorized based on: (1) whether they are a formate dehydrogenase or formylmethanofuran dehydrogenase; (2) whether the metal is molybdenum or tungsten; and (3) whether the ligand provided by the polypeptide is cysteine or selenocysteine. A final level of variation is the overall subunit architecture, as these enzymes can range from having a single [4Fe-4S] in addition to the Mo/W center in a monomeric FdhF to the extremely complex (FwdABCDFG)$_4$ formylmethanofuran dehydrogenase from *Methanothermobacter wolfeii* possessing four Mo/W centers and 46 [4Fe-4S] clusters (Niks and Hille 2019).

Selenocysteine-containing formate dehydrogenases seem to be faster than their cysteine-containing counterparts, although the enzymes that possess cysteine natively exhibit faster kinetics relative to their Cys-to-Sec variants (Niks and Hille 2019). There are three formate dehydrogenases expressed in *E. coli*, two of which are periplasmic respiratory enzymes. The third is FdhF, which functions physiologically as part of the formate-hydrogen lyase complex and is a selenocysteine-containing formate dehydrogenase.

After reinterpretation and re-analysis of the X-ray crystal structure of FdhF (Shown in Figure 11) it has been shown that there is an apical sulfur ligand coordinated to the molybdenum. In addition to the bis-MGD, FdhF possess a [4Fe-4S] cofactor (Leimkühler 2020) .
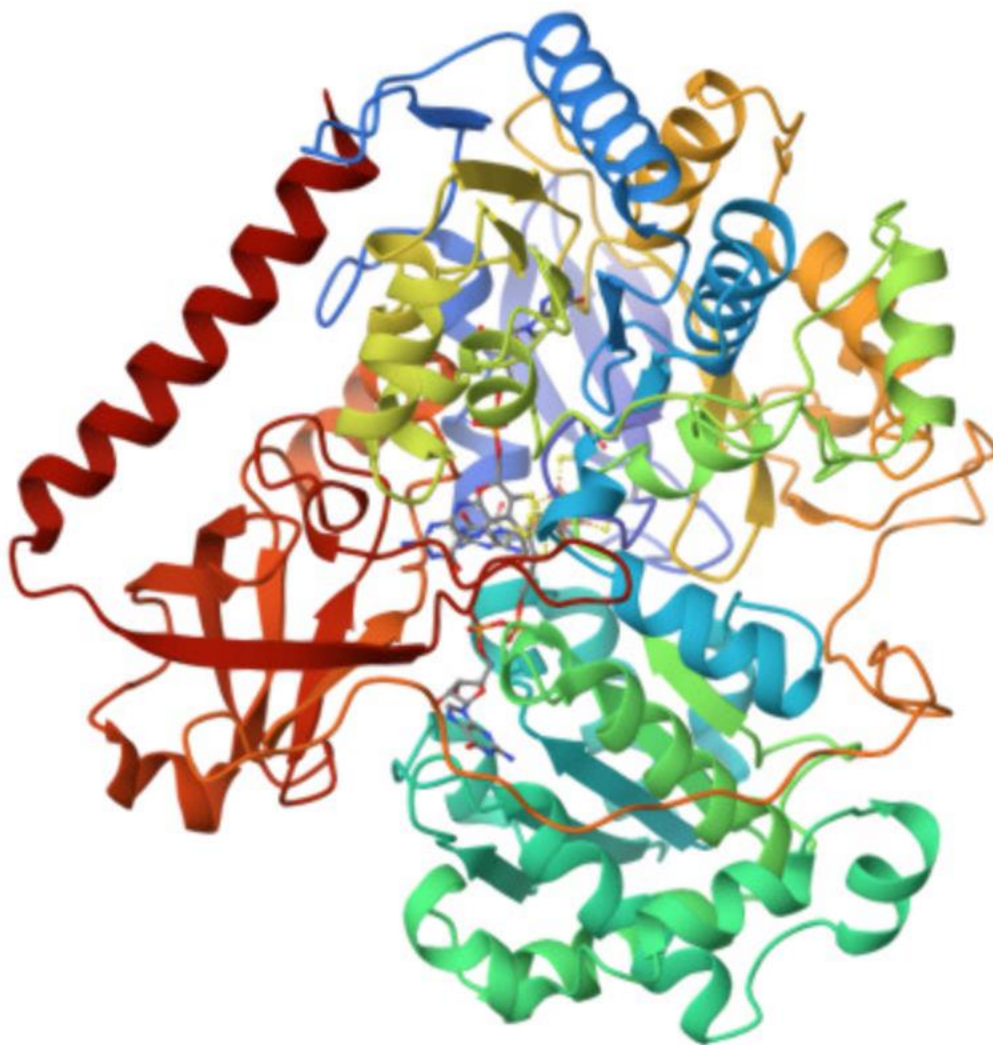
Figure 11. X-ray crystal structure of FdhF from E. coli (PDB 1FDO) (Gladyshev et al. 1996).

The molybdenum center of FdhF is sulfurated by the FdhD sulfurase, which is thought to sulferate and then insert the molybdenum cofactor, using sulfur provided by the L-cysteine desulfurase IscS. The process involves transfer of sulfur from a persulfide-lscS to a new persulfide group on a conserved cysteine on FdhD. As mentioned earlier, the Mo=S group thus introduced is catalytically essential (Iobbi-Nivol and Leimkühler 2013). In the absence of FdhD, FdhF is expressed in an inactive form, although it can be activated

by chemical sulfuration upon incubation with Na_2S (Leimkühler 2020). There are two EPR signals observed upon reduction of the *E. coli* FdhF with formate, as depicted in Figure 12. The first is a Mo(V) observed at temperatures below 130 K and the second a signal from the reduced [4Fe-4S], which appears only below 50 K. The g values for these signals are $g_{1,2,3} = 2.094, 2.001, 1.989$ and $g_{1,2,3} = 2.045, 1.957, 1.840$, respectively. The Mo(V) signal exhibits coupling to a proton with $A_{1,2,3} = 7.5, 19$ and 21 MHz. When deuterated formate is used, this coupling is not observed initially, but does grow in over 30-300 s as the Mo-SH of the now-reduced molybdenum center exchanges with solvent (Russ Hille, Hall, and Basu 2014).
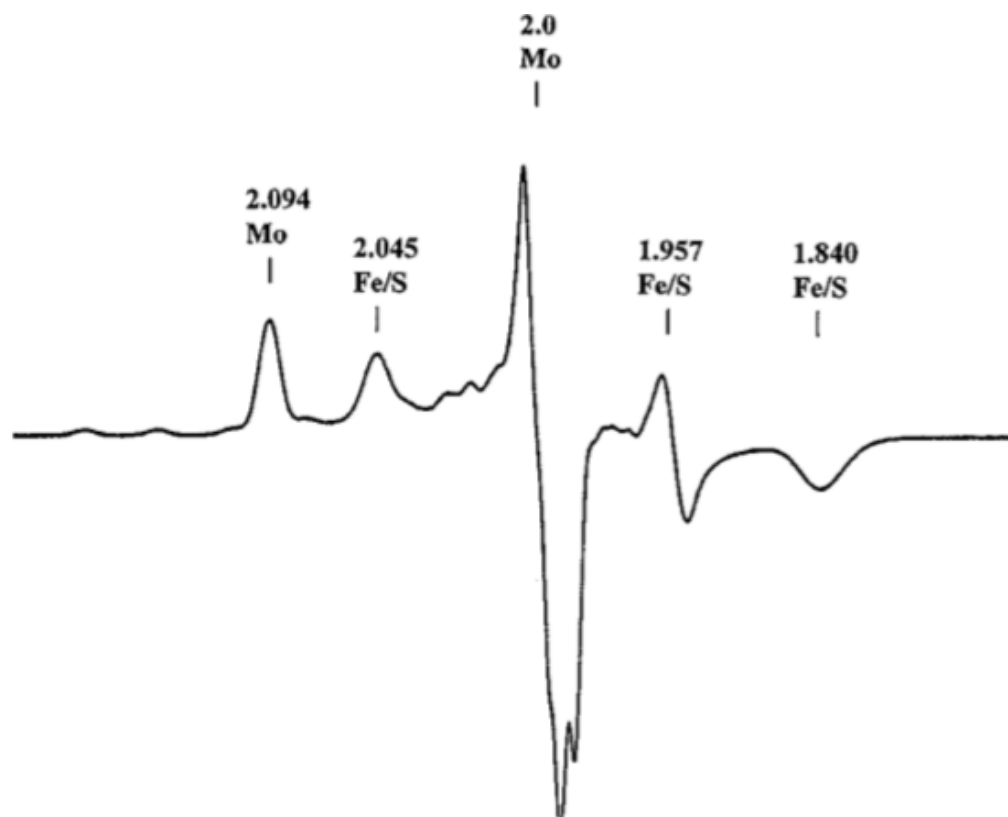
Figure 12. EPR spectra of FdhF from *E. coli*. EPR spectra of FdhF at two different temperatures were recorded. A. FdhF incubated with 10 mM sodium formate for 1 minute. This spectrum is a superposition of two signals which can be achieved at different temperature. One is signal belongs to 2Fe-2S cluster with g values of 1.840, 1.957 and 2.04. This signal appears at below 50 K. The other signal which appears at 130 K or below represents the Mo(V).

1.4. X-ray crystallography

1.4.1. Brief history of X-ray crystallography

Humans have been fascinated by crystals forever. However, two dates are significant for our understanding of crystals. The first, 1895, when Wilhelm Conrad Rontgen discovered X-rays in Germany. The second, 1912, when Max Laue shone X-rays on a copper sulfate pentahydrate crystal producing a distinct, regularly spaced pattern as shown in the right panel of Figure 13. Although Laue came up with a physical explanation for the observed diffraction pattern, it was Sir William Henry Bragg and Sir William Lawrence Bragg who realized that X-ray diffraction is intimately linked to the structure of the crystal. This insight allowed the Braggs to develop the now famous equation, $n\lambda = 2d\sin\theta$, also known as Bragg's law. The details of the equation will be discussed a bit later in this study (Jaskolski, Dauter, and Wlodawer 2014). Bragg's law shows how the structure of a crystal can be extract from its the X-ray diffraction pattern (Aitipamula and Vangala 2017). The important findings of Laue and the Bragg father and son team were honored with a Noble prize in physics in 1914 and 1915, respectively.
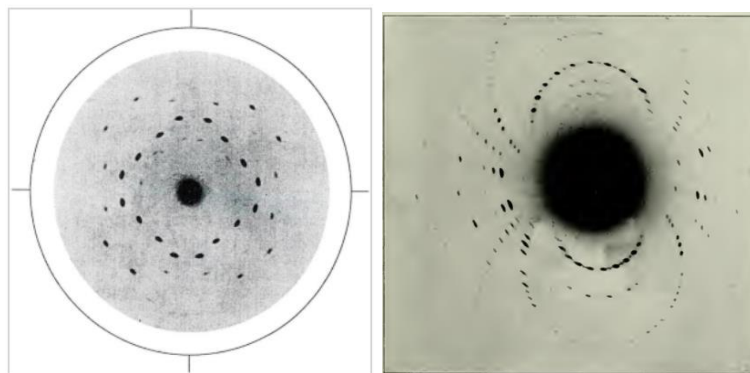
Figure 13. X-ray diffraction patterns. X-ray diffraction pattern of ZnS is shown on the left side. Photo was taken by Max Lau. On the right side is the x-ray diffraction pattern of nickel sulfate (Thomas 2012)

Since then, X-ray crystallography has developed into a comprehensive method to investigate the position of atoms, and thus the interactions between them within a crystal. This progress had a significant impact on many areas of science, such as geoscience, material sciences and pharmaceuticals. For instance, the atomic structures of medical reagents and drugs have aided in improving their medical efficacy and in the designing of new drugs (Aitipamula and Vangala 2017). X-ray crystallography started to have a greater impact on microbiology and related fields as well, after it was shown that proteins could be crystalized. The very first protein to be crystalized was urease, an enzyme that breaks Urea down into carbon dioxide and ammonia. This provided evidence that enzymes and proteins can be studied via X-ray crystallography.

1.4.2. Crystallographic terms and concepts

X-ray Crystallography encompasses a wide range of terms and concepts that are essential to the study of crystals and their structures. In this section some of the key crystallographic concepts and crystal properties will be discussed.

1.4.2.1. Unit cell

X-ray crystallography allows the study of the three-dimensional structures of small molecules and macromolecules, such as proteins. The smallest repeating unit, that makes up a crystal is called a unit cell. A unit cell is characterized by three vectors a, b, and c which form the edges and three angles α , β, and γ as depicted in Figure 14 (Ali, Chiang, and Santos 2022). Although the unit cell is repeated throughout the crystal, the repetition

does not extend to the same degree in all directions. The more a unit cell is repeated in one direction the higher quality of X-ray data can be collect in that direction.
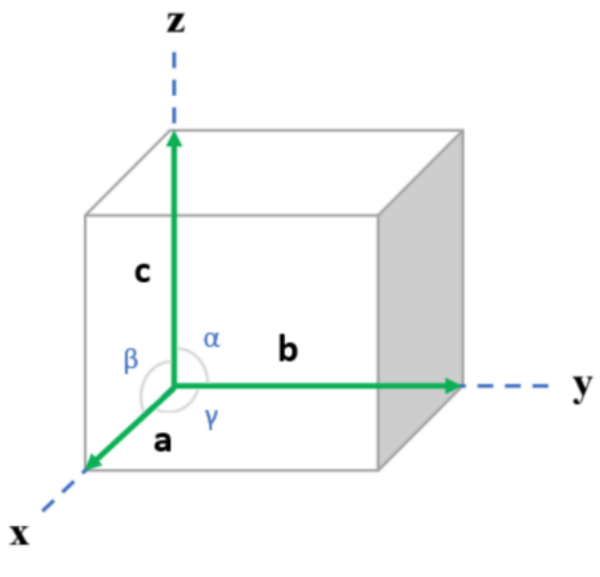
Figure 14. Parameters of a unit cell (Ali, Chiang, and Santos 2022)

1.4.2.2. Asymmetric unit

The smallest building block from which a unit cell can be constructed is the asymmetric unit. It contains all essential information to describe the entire crystal lattice. The unit cell can be built from the asymmetric unit by one or more symmetry operations such as rotation, and translation. This is also how the asymmetric unit relate to subsequent units (Brito and Archer 2020).

1.4.2.3. Crystal lattice system

A crystal lattice refers to a three-dimensional arrangement of points (atoms or molecules) within a crystal. The unit cell serves as a building block to generate a crystal lattice. Each point represents a unique position in the crystal (Souza, Selistre-de-Araujo,

and Garratt 2000). There are seven lattice systems, each of them is defined by a set of specific symmetry operations. A crystal needs to possess this set of elements as a minimum requirement to be part of one of the systems. Figure 15 represents all seven systems (Shirokanev, Kirsh, and Kupriyanov 2019).
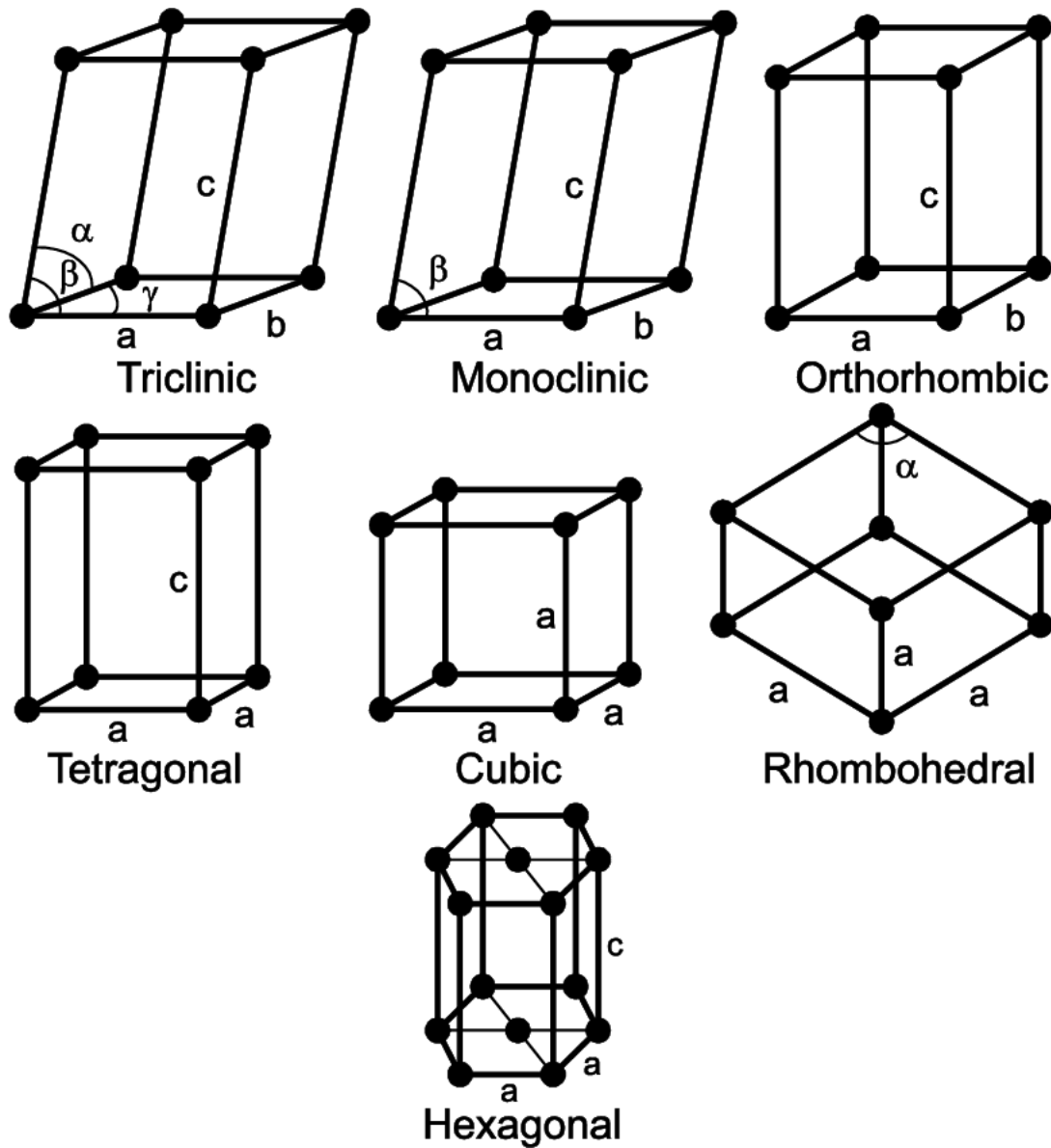
Figure 15. Seven crystal system (Shirokanev, Kirsh, and Kupriyanov 2019)

1.4.2.4. Crystal centering

Crystal centering describes how multiple lattices can be staggered into each other. There are five possibilities for centering crystals: no center (primitive or P), body centered (I), all the faces centered (F), one centered face (A, B or C, according to Figure 14, face A lies in the bc plane (gray area) and etc.), rhombohedral indexed on hexagonal axes (R). The combination of the seven crystal systems and how to center a crystal result in fourteen Bravais lattices shown in Figure 16 (Rissa 2002)
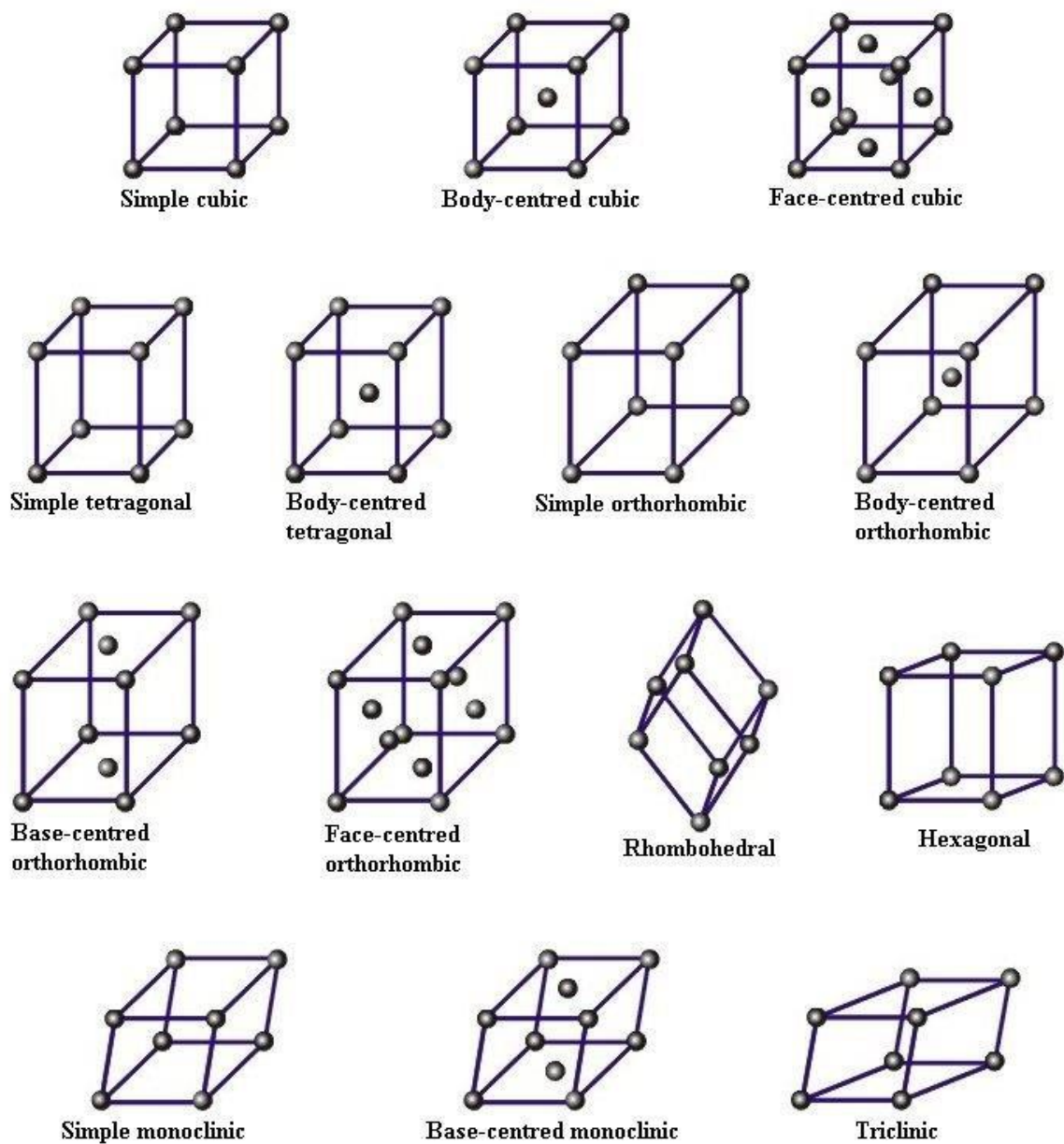
Figure 16. Fourteen Bravais lattices. Bravais lattices are a set distinct three-dimensional lattice structures that describe the arrangement of points in a crystal lattice. (Rissa 2002).

1.4.2.5. Miller indices

The Miller indices indicate the relative position of a Miller plane within the crystal lattice by showing the point of intersection of the plane with the unit cells' axes. Miller planes, also known as lattice planes, are represented by Miller indices, demonstrated in Figure 17. The plane with the Miller indices (h,k,l) creates the interceptions a/h, b/k and c/l with unit cell axis. Miller indices must be integer numbers to preserve crystal symmetry, provide a simplified representation, and align with the principles of Bragg's Law in X-ray diffraction. (Clegg,1998).
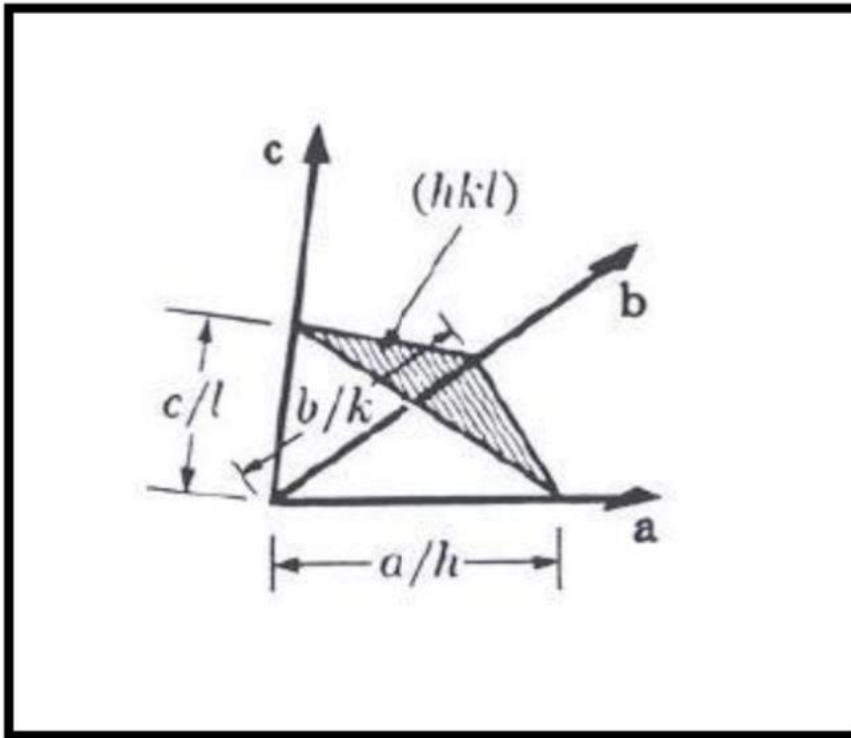
Figure 17. Miller indices. Miller indices are a system of notation used in X-ray crystallography to represent the orientation and planes of crystal faces. (Clegg, 1998).

1.4.2.6. Bragg's law

Bragg's law is a fundamental principle in X-ray crystallography that describes the relationship between the angles at which X-rays are diffracted of a crystal lattice and the distances between the Miller planes. For an X-ray diffraction to occur, the Miller planes of the crystal and the incident X-ray beam must abide by the following equation:

$$n\lambda = 2d \sin\theta \quad (1)$$

Each set of planes acts as a refracting surface for the incident X-ray beam. d is the distance between parallel planes, θ is the angle between incident beam and the diffracting plane, n is an integer and λ is the wavelength. A refracted beam will appear as a diffraction spot on a detector distant to the diffracting crystal. Figure 18 is a simplified figure to show the parameters at play in Bragg's law.
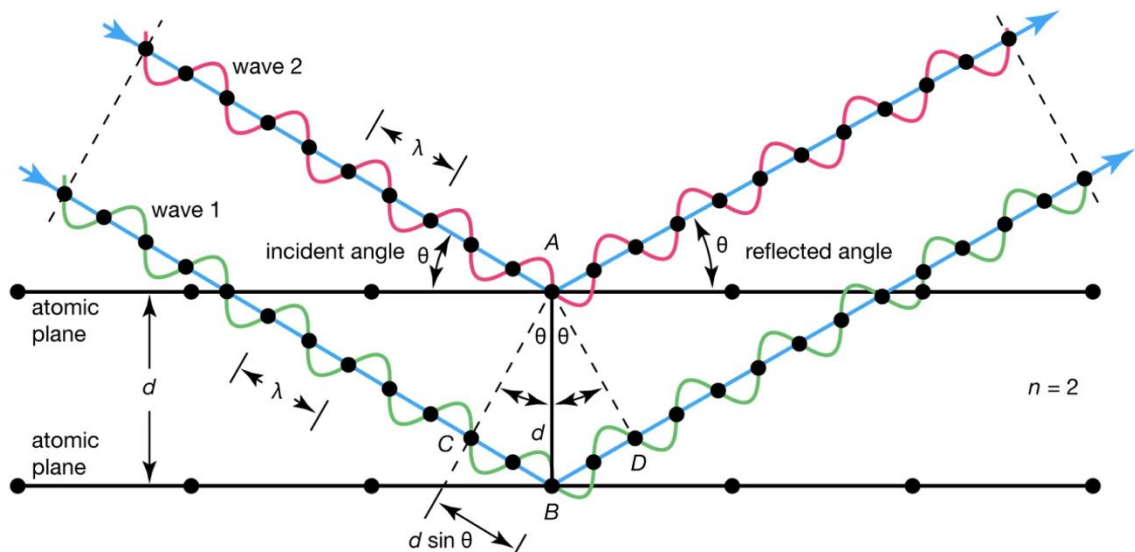
Figure 18. Parameters of Bragg's law. Bragg's law describes the relationship between the wavelength of X-rays diffracted by a crystal lattice and the angle of incidence, allowing for the determination of the interatomic spacing within the crystal.
https://www.britannica.com/science/Bragg-law.

1.4.3. Preparation of protein crystals

To grow protein crystals, a protein is coaxed to transition from being dissolved in aqueous solution into the solid state. Under ideal conditions, crystals will form during this transition. The chances to identify such conditions are significantly improved when sufficient amounts and purity of the protein are at hand. In the early days, proteins were isolated from natural sources, such as specific animal organs or products. This approach is now rare, as genetic engineering of bacteria has disburdened the process of obtaining pure protein at the quality and quantity suited for crystallography.

The transition of the protein from being dissolved in solution to solid crystal can be broken into three steps: supersaturation of the protein in solution, nucleation of the protein crystals, and growth of these nuclei. To accomplish these steps, many approaches are available. Several of these approaches can be reformatted to enable automatization thus allowing the screening of crystallization conditions in a high throughput manner. The most common methods to drive a proteins solution into the supersaturated state are by vapor diffusion and batching. Each method is unique in terms of what route they follow in the phase diagram (see Figure 19 for a typical phase diagram of a protein).

In the vapor diffusion approach, the initial state of the protein solution is undersaturated. The protein solution is incubated over the reservoir solution. Over the course of incubation, water diffuses from the protein solution to the reservoir solution, concentrating the protein solution and thereby driving it towards saturation and eventually supersaturation (see route (ii) in Figure 19).

In the batch method, the protein solution is mixed with a crystallization solution. At the moment of mixing both solutions, the protein solution reaches the supersaturated state. As the protein transitions to the solid phase, its concentration in solution decreases until it establishes the equilibrium between proteins binding and dissociating form the crystal (see route (i) in Figure 19; (Govada and Chayen 2019)).
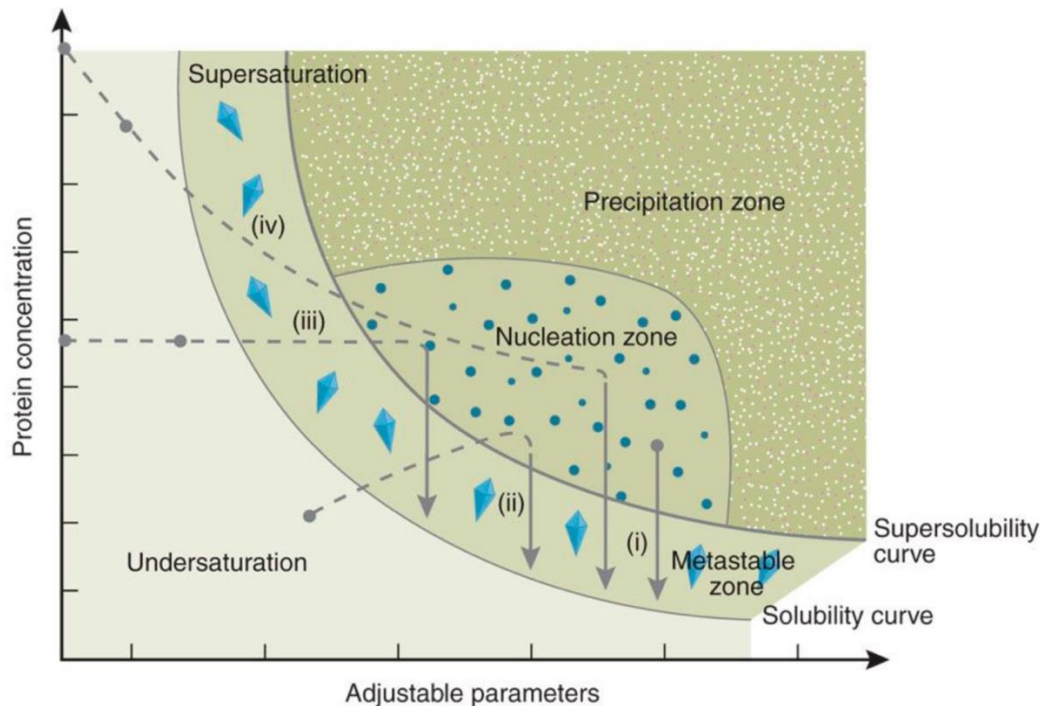
Figure 19. Phase diagram. Different routes that each method takes in a phase diagram. (i) Batching (ii) Vapor diffusion (iii) Dialysis (iv) Free interface diffusion (Chayen and Saridakis 2008).

The vapor diffusion method is categorized into two sub-methods: sitting drop and hanging drop. Although both methods use vapor diffusion to drive a protein solution to supersaturation, the crystals produced via hanging drop are usually larger and have a better appearance with fewer cracks than those produced via sitting drop. However, because of

its simplicity and its ease of automatization, sitting drop is the method of choice for high throughput screening of crystallization conditions (Hou et al. 2019).

1.4.4. X-ray data collection and processing

A synchrotron beamline is used in X-ray crystallography for generation of intense and focused radiation, manipulation of them for optimal performance, collection of diffraction data, and analysis of the data to determine the crystal's atomic structure. A synchrotron beamline consists of a source of radiation, optical elements such as focusing mirrors and monochromators and a detector (Dauter 1996). A synchrotron is an evacuated hollow ring in which electrons move at the speed of light. To constrain the electron within the ring, magnetic fields are applied (Clegg et al. 2009). As the high-energy electrons travel along their curved paths within the storage ring, they experience acceleration and change in direction due to the magnetic fields produced by bending magnets and insertion devices. This acceleration of charged particles results in the emission of electromagnetic radiation known as synchrotron radiation. Synchrotron radiation spans a wide range of wavelengths, including X-rays, ultraviolet (UV) light, and infrared (IR) radiation, depending on the energy of the accelerated electrons. A monochromator consisting of a crystal or a grating that will selectively diffract X-rays of a particular wavelength while allowing other wavelengths to pass through or be absorbed. This process narrows down the X-ray beam to a desired wavelength range (Petrov 2021). The monochromator the X-rays are directed towards a crystal. At the crystal the X-rays have two possibilities: they can pass through the crystal without interacting with it, or they can interact with the crystal

the crystal and thereby being redirected into a different direction. The second scenario is called diffraction. The diffracted beam forms a pattern of spots (Figure 13) from which the following information can be extracted:

Position of the spots: An individual scattered X-ray beam is diffracted off one Miller plane. Therefore, each spot is assigned the Miller index of the plane that produces it (I_{hkl}).

Symmetry of diffraction pattern: The combination of the spots results in a pattern. The symmetry of the pattern is related to the symmetry of the unit cell of the diffracting crystal.

Intensity of each spot: Each spot has its own intensity, which is related to the position of the atoms within the unit cell (Clegg et al. 2009).

1.4.4.1. Data collection strategies

Various data collection strategies are employed to obtain high-quality diffraction data from a crystal. Factors such as the crystal size, crystal quality, radiation sensitivity, and the desired level of resolution have a significant impact on the decision of what method to employ. The commonly used strategy of data collection is the rotation method. In this method, the crystal is rotated continuously while X-ray images are collected at regular intervals. This technique provides data from different crystal orientations, increasing the accuracy for the calculations of intensities (Powell 2017).

1.4.4.2. Data processing software

X-ray crystallography relies on a range of software packages and computational methods to process and analyze the collected diffraction data and determine the atomic structure of a crystal. These software tools and methods aid in the transformation of diffraction patterns into information about the arrangement and orientation of atoms within

the crystal lattice. CCP4 (Collaborative Computational Project Number 4), Phenix, Coot, the CCP4i2 graphical interface, HKL2000, XDS, and MOSFLM are examples of these software which provide a collection of programs for data processing, model building, refinement, and validation (Powell 2017).

1.4.4.3. Structure determination

Once the diffraction data are collected, the recorded intensities undergo processing steps such as background subtraction, integration, and scaling to extract the spot intensities. Next, the spot intensities are converted into structure factors. These are complex numbers comprising amplitude and phase components. The amplitudes are obtained directly from the intensities of the reflections, whereas the phases cannot be measured directly which is referred to as the phase problem. This topic will be addressed in more detail at a later point. Once both amplitudes and phases are obtained the electron density map of the unit cell can be calculated. This map serves as a basis for constructing the structural model of the unit cell. The map is calculated by a Fourier transform of the structure factors. The equation below (equation 2) shows how the electron density map is calculated from the structure factors (F_{hkl}).

$$\rho(xyz) = \frac{1}{V} \Sigma \; |Fhkl| e^{i\alpha hkl} \, e - 2i(hx + ky + lz) \quad (2)$$

$|F_{hkl}|$ are the amplitudes which are derived from the intensities, α_{hkl} are the phase angles and $\rho(xyz)$ is the electron density (Taylor 2003).

In crystallography, the term "phase problem" describes the limitation determining the phase of the diffracted beam directly yet it is required for determine the electron density of the unit cell. Resolving the phase problem is essential for generating the electron density

map and ultimately obtaining a model for the crystal's structure. Small molecules contain fewer atoms and the diffraction data collected of crystal of them have generally high resolutions. This simplifies the problem of overcoming the phase problem as the phases can be directly estimated from the diffraction data. This method is called the direct method and is based on estimation of phases from strong reflections. Based on those estimations, phases for the rest of the reflections are deduced. Unfortunately, this approach is not suitable for diffraction pattern of large molecules. To overcome the phase problem of large molecules additional methods have been developed. One of these methods is molecular replacement (Ooi 2010).

1.4.4.4. Molecular replacement

This method requires the known structure of a homologous protein. In this approach the structure of the homologous protein goes through a series of rotations and translations to find the best orientation of the unknown structure within the unit cell. If the steps are performed correctly, the structure factors calculated from the model will match those of unknown structure close enough that a sensible electron density map for the unknown structure can be calculated. Many factors affect the success of this method, such as the quality of the model chosen, the completeness and resolution of the collected diffraction data (Taylor 2003).

1.4.4.5. Model building, refinement, and validation:

This step consists of fitting the backbone and side chains of the amino acid residues of the crystalized protein into the electron density map. In other words, building a model

involves constructing an initial representation of the atomic structure of the unit cell of the crystal.

During the refinement process the crystallographer or the software iteratively adjusts and refines the atomic positions to improve the fit between the model and the experimental data (Brünger 1992). During this refinement process various restraints, on the possible bond lengths, bond angles, and dihedral angles within the model are applied to maintain the physical plausibility of the model during refinement. In addition, prior knowledge as well as chemical constraints are employed to ensure that the final model is a realistic representation of the structure of the protein in the crystal (Bergmann, Oksanen, and Ryde 2022).

1.5. Electron paramagnetic resonance (EPR)

Yevgeny Zavoisky recorded the very first EPR spectra of copper and manganese more than 70 years ago on a home-built spectrometer. EPR is used in various fields such as chemistry, biological sciences, physics and material sciences. EPR shares the same fundamental principles as NMR as both methods involve the absorption of light as a magnetic moment in an applied magnetic field. The differences arise when considering the target of these electromagnetic radiation: NMR involves the nuclear magnetic moment whereas EPR involves the magnetic moment of one or more unpaired electrons. In NMR, it is the nuclear spin states that are being studied and it is much more common to find an NMR-active nucleus, (meaning $I \geq 1/2$). On the other hand, not many molecules are EPR-active as most have all their electrons paired up in chemical bonds, although transition metal complexes often are EPR-active. Another significant difference between NMR and

EPR is that EPR requires higher frequency when it comes to electromagnetic radiation. As a result, microwave frequency radiation is used in EPR instead of radiofrequency radiation used in NMR. In EPR, the microwave frequency is designated in terms of "bands": "X-band" is most common and uses a microwave frequency of approximately 9.5 GHz and the applied field is typically around 0.3 T. "Q-band" is another frequency region, conducted at ca. 35GHz. The sensitivity limit for EPR depends on experimental conditions (particularly temperature), the specific spin system under investigation, and the linewidth of the EPR spectrum. Since there is a requirement of at least one unpaired electron, only a relatively small group of molecules and compounds that can be studied, particularly organic radicals and transition metal complexes, although many macromolecules can be modified with stable radical species termed spin-labels. Even with EPR-silent (diamagnetic) compounds, EPR-active states can be generated by reduction, oxidation or photoexcitation (Roessler and Salvadori 2018). There are two fundamental physical principals regarding EPR which will be described briefly below.

1.5.1. The electron Zeeman interaction

The interaction between applied magnetic field and the unpaired electron is described by a parameter called the "g" value. Electronic ground state and molecular environment are the main factors for g values. If g values do not change with changing the magnitude of the magnetic field, it indicates that the interaction between the centers are negligible. The g value can be used as a fingerprint to identify a paramagnetic species and the value of it depends on the molecule which that unpaired electron is attached to. The free electron g value is $g_e \sim 2.0023$. The shift from g_e depends on the extent to which the intrinsic "spin"

magnetic moment of the electron interacts with any magnetic moment associated with the orbital in which the electron is found. This shift can be quite large for transition metals and lanthanides, where the unpaired electrons are localized in d or f orbitals. Due to their partially occupied d orbitals, transition metals quite often possess unpaired electrons and are paramagnetic hence a good subject to investigate in the world of EPR (Roessler and Salvadori 2018). g values are independent of the frequency of the microwave radiation and describe the intrinsic resonance state of the unpaired electron relative to its environment. Equation 3 describes the spin angular momentum that electrons possess due to spinning around themselves, S is the quantum number; h is Planck's constant (6.626 x 10^{-34} Js).

spin angular momentum $= h/2\pi[S(S+1)]1/2$ (3)

The magnetic moment associated to the spin angular momentum, modified for only along the z direction is described as follows:

$\mu_z = -g_e\mu_B M_S$ (4)

μ_B represents the Bohr magneton, g_e is the g-factor for free electron. M_S is equal to $S(S+1)^{1/2}$ where S is equal to $\frac{1}{2}$ for a single unpaired electron. Thus, the spin angular momentum for that unpaired electron holds a value of $\pm \hbar/2$. The plus-negative sign means that the spin angular momentum for a free electron has two possible orientations which are in opposite directions. This leads to two different magnetic momentum and as a consequence, two different spin states. These two states are degenerate in the absence of an external magnetic field. Once a magnetic field is applied, these states will interact with

the field which is called the Zeeman interaction and will have different energy levels. Equation 5 describes this interaction.

$$E = - \mu_z B \ (5)$$

B represents the strength of the magnetic field applied. If μ_z in equation (4) is replaced with the corresponding value from (3) and plug in the values for a single unpaired electron equation (6) is yielded:

$$E = \pm \frac{1}{2} g_e \mu_B B \ (6)$$

These two energy levels are called the Zeeman levels and the difference between these levels is known as the Zeeman splitting. In Figure 20, the Zeeman effect, which is the lift of degeneracy of the spin states in the presence of an external magnetic field is illustrated (Rowlands and Murphy 1999).

Energy

$M_s = \frac{1}{2}$ α spin ↑

$E_1 = \frac{1}{2} g_e \mu_B B$

$\Delta E = E_1 - E_2 = g_e \mu_B B = h\nu$

$M_s = -\frac{1}{2}$ β spin ↓

$E_1 = -\frac{1}{2} g_e \mu_B B$

$B = 0$ Applied magnetic field B (mT)
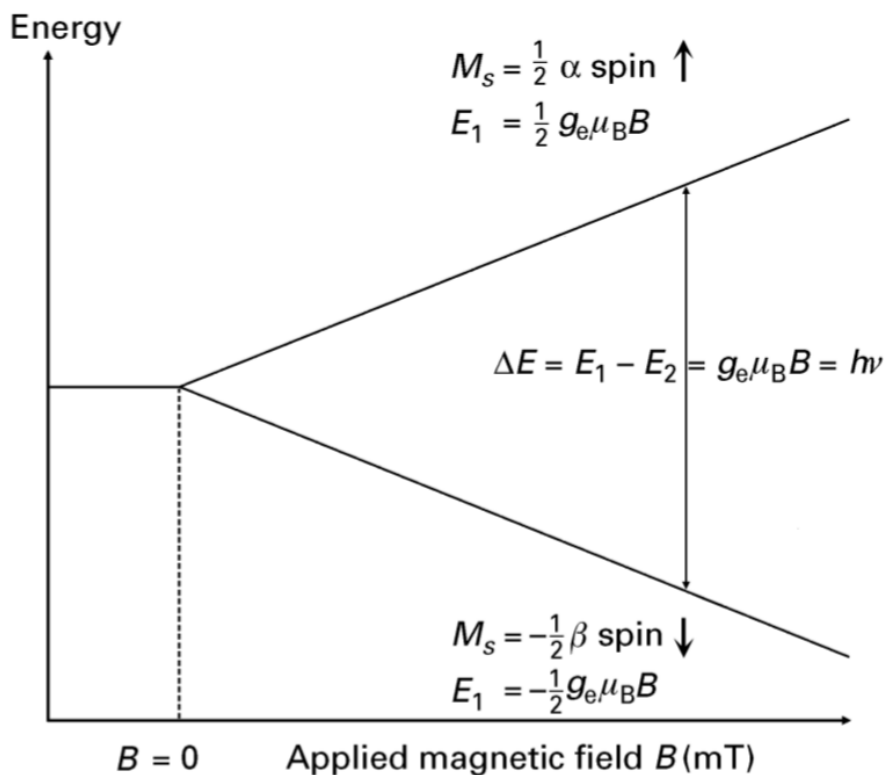
Figure 20. The Zeeman effect. After the application of the magnetic field the energy levels of the two different spin states $(\pm\frac{1}{2})$ are no longer degenerate. The different directions of the spins are shown with α for up and β for down (Rowlands and Murphy 1999).

The Zeeman interaction between the magnetic moment of the electron and the applied magnetic field is dependent on the strength of the applied magnetic field. EPR experiments at different fields can help distinguish between field-dependent and independent interactions in complex spectra. EPR samples are typically either powder or frozen solutions in the solid state, hence, g values can have three components, (g_1, g_2, g_3) or (g_x, g_y, g_z) depending on the asymmetry of the paramagnetic species and the orientation of a given molecule in the magnetic field. Highly symmetric molecules typically yield isotropic EPR signals where all three g components have the same value ($g_x = g_y = g_z$). Planar molecules can yield axial EPR signals with two identical g values and a third unique

one ($g_x = g_y \neq g_z$). Finally, highly asymmetric molecules (or more symmetrical ones in an asymmetrical environment) give rhombic EPR signals in which $g_x \neq g_y \neq g_z$. In solution, the tumbling and random motions of molecules lead to an average g value.

1.5.2. The electron-nuclear hyperfine interaction

The electron-nuclear hyperfine interaction is the interaction between the magnetic moment of the unpaired electron and the nuclear moments of nearby nuclei and has two contributions. The first is the isotropic hyperfine interaction is due to polarization of inner s orbitals by the magnetic moment. The isotropic hyperfine provides information on spatial and nature of the orbitals the unpaired electron will be in. The second contribution is the anisotropic hyperfine interactions (*A*), which is a magnetic dipole-dipole interaction. *A* depends on several factors, including the orientation and distance between the unpaired electrons and the nucleus. Like the g tensor, *A* can have as many as three components (A_x, A_y, A_z) and can be very useful in providing spatial information. Hyperfine interactions split energy levels and simplify extracting information from an EPR spectrum (Roessler and Salvadori 2018).

1.5.3. Electron-electron coupling

When there is more than one unpaired electron in a transition metal complex, it is important to consider so-called zero-field interactions when $S > \frac{1}{2}$. These arise because each electron will have dipolar and spin-orbit coupling interactions which remove the (2S+1) degeneracy expected in the ground state. This is called zero-field splitting, and as the name suggests is present even when no magnetic field is applied. Zero-field splitting

has two parameters, the average distance between the unpaired electrons and the deviation from the cubic symmetry (Roessler and Salvadori 2018).

1.5.4. Relaxation time (T_1 and T_2)

There are two types of relaxation times that impact EPR results, the spin-lattice relaxation time (T_1) and spin-spin relaxation time (T_2). The spin-lattice or longitudinal relaxation time reflects the transfer of energy from the excited magnetic moment to its environment through thermal vibrations of the lattice. The spin-spin or transverse relaxation time T_2 occurs with no net energy charge and simply shows the distribution of energy among the spins. Relaxation is important since in its absence the distribution of spins in the ground and excited states equalizes and the net microwave radiation absorption becomes zero and thus, no EPR signal is observed. At room temperature, relaxation rates are typically very fast, which can lead to broadening of the EPR signal, and again no signal is detected. Cryogenic temperatures are used to slow down both T_1 and T_2 (Roessler and Salvadori 2018).

There are two main types of EPR experiments: continuous wave (CW) and pulsed EPR. CW is used more generally, whereas pulsed EPR is used to analyze specific interactions, particularly weak ones, in detail.

1.5.5. CW EPR

In CW EPR, low-intensity monochromatic microwave-frequency light is irradiated on the sample continuously. The magnetic field will be swept over a specific range and when the energy gap between ground and excited spin states matches the energy of the microwave light, the sample will resonate. The spectrum is typically presented as

derivatives because the field sweep is modulated to improve signal-to-noise. CW EPR is a very convenient way of studying paramagnetic species, but it has a very limited resolution and might not be enough for many in-depth study cases. If the samples for CW are in fluid state, then all the tumbling and motions of the molecules are averaged out and only the isotropic components will show up as a result. On the contrary, when the samples are in solid state (frozen), the orientation of each of the individual molecules is fixed relative to the magnetic field which results in different grade of interactions. In CW data, only the hyperfine couplings are not masked because their electron-spin interactions are very large relative to the remainder interactions which get lost due to broad linewidths.

1.5.6. Pulsed EPR:

The samples in pulsed EPR are irradiated with high intensity square-wave microwave pulses (representing a broad range of frequencies) and the magnetic field is kept constant. New methods in pulse EPR enable the isolation of specific interactions which contribute to CW EPR data. For instance, even with a simple pulsed EPR, it is impossible to attain a complete set of magnetics parameters without simulation of the spectra at different field positions. This is due to orientation selection. However, shaped and composite pulses provide the chance to independently tune the amplitude and the phase of the pulses and thus resolve the orientation selection issue and improve excitation bandwidths. Pulsed EPR is done at cryogenic temperatures since the relaxation times are too short at room temperature. Unlike CW, the data are shown as absorption spectra in Pulsed EPR.

1.6. X-absorption spectroscopy

One of the very effective ways to study the correlation of structure and function of metal containing active sites in metalloenzymes is X-ray absorption spectroscopy (XAS). In a typical experiment, absorption of X-rays excite core (e.g., 1s) electrons into a bound excited state or, if there is sufficient energy, into the continuum which then produces a photoelectron. Absorption is typically monitored indirectly by the X-ray fluorescence as higher-shell electrons fill the core "hole" created by the primary ionization event. The wavelength dependence of the X-ray absorption is dependent on the identity of the absorbing nucleus, its oxidation state, chemical environment and the nature of chemical bonding to it. Ionization of an electron from a 1s orbital gives rise to the K-edge. The L-edge is due to ionization of an electron from 2s or 2p orbitals, as illustrated in Figure 21 (Yano and Yachandra 2009).
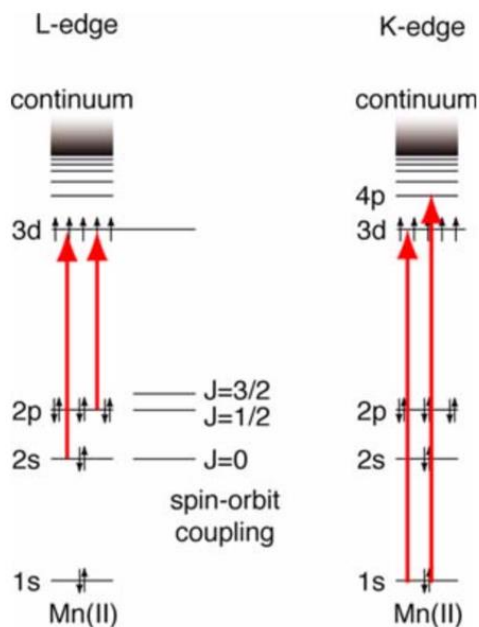
Figure 21. The energy level diagram. On the left, the transition of the L-edge and on the right the energy level diagram for K-edge are shown in this example for Mn(II). (Yano and Yachandra 2009).

The data from an XAS experiment is presented in a form of a graph of X-ray absorption coefficient versus energy. The X-ray absorption coefficient is directly proportional to the probability of absorption of a photon, and it is a decreasing function of energy. It is displayed as μ. If the sample is a monoatomic gas or if the absorbing atom is isolated in space, then the absorption has a uniform decreasing trend in respect to energy and the photoelectron will propagate as an unperturbed isotropic wave (Figure 22). Whereas in any other type of sample, there are oscillations that begin right after the edge and continue for thousand eV (Figure 23). Each of the neighboring atoms of the absorbing atom in this specific chemical environment, will backscatter the emerging photoelectron wave, each scatterer contributing a pattern of damped oscillations due to alternate constructive and destructive interference. The sum of the original and all scattered waves gives the final state of the photoelectron (Vlaic and Olivi 2004). For XAS, it is crucial to have models of known structures of similar compounds, which aid in understanding the impact of the environment on the absorption edge energy.
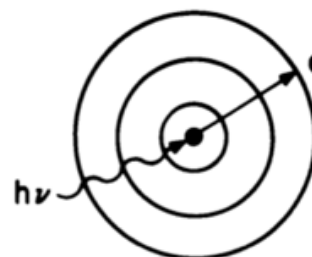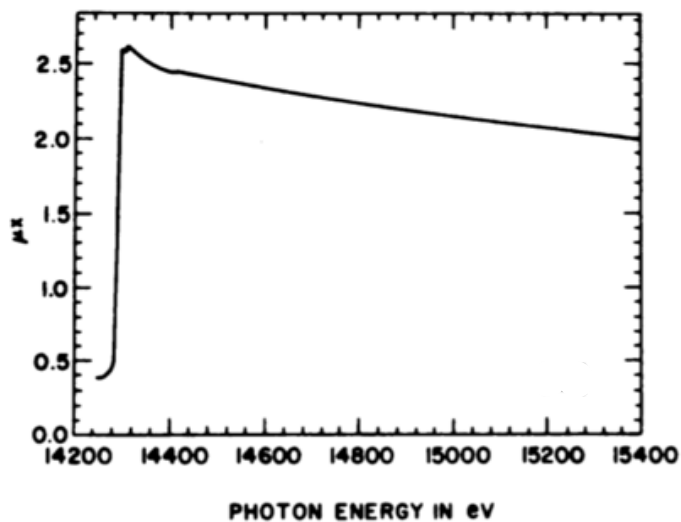
Figure 22. XAS spectrum of a monoatomic gas. This spectrum obtained will be in the absence of other scatterers (Teo 1981).
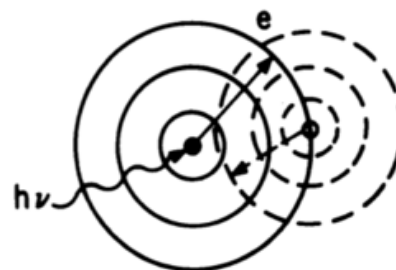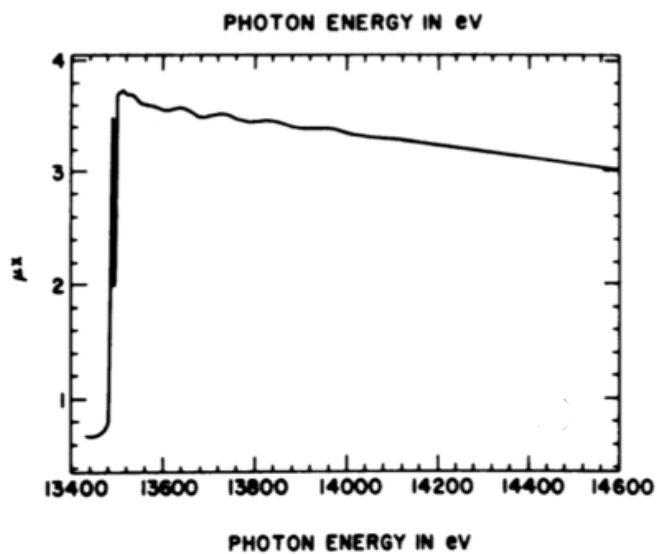
Figure 23. XAS spectrum of a polyatomic gas. The spectrum will be obtained in the presence of other scatterers in the vicinity of the original scatterer such as a diatomic gas (Teo 1981).

Compared to X-ray crystallography, XAS has a major advantage in that the samples do not need to be in the form of a crystal in order to obtain structural information, as a

matter of fact they can be in solution or in powder form. Also, XAS is relatively less invasive and damaging to the samples. Moreover, very small changes in geometry and structure in relation to the transitions are detectable. One of the major advantages that XAS has compared to EPR, or many common methods is the fact that the element of interest is never silent. In XAS, lower temperatures are preferred to avoid the diffusion of hydrated electrons and free radicals. One of the best solutions to this problem is using liquid He temperatures and He gas atmosphere. Indeed, like any other scientific approach, this method has also its very own limitations. A very common issue comes up regarding atoms with very similar atomic numbers such as N, O and S as distinguishing between these is very challenging with XAS (Yano and Yachandra 2009).

1.6.1. XANES

X-ray near edge structure (XANES), is due to bound state transitions where the photoionized core electron is promoted to a higher level orbital, giving rise to absorption bands just below the X-ray absorption edge, reflecting ionization into the continuum. Electronic structure and symmetry of the metal center are types of information that XANES delivers. The information related to the electronic structure is a result of a direct relationship between the energy for K-edge and oxidation state. The position of the absorption edge is dependent on the positive charges. The higher the oxidation state of an atom, the more positive charges, thus higher levels of energy required for excitement of an electron. On the contrary, if the negative charges are more dominant then lower levels of energy are needed. 1s to np is the main contribution to the K-edge. By investigating the K-edge, not only information is provided about allowed transitions ($\Delta l=l$) which are intense

but also some of the weaker, traditionally forbidden transitions (Δl=2) (Yano and Yachandra 2009).

Figure 24 represents a simple XAS plot. The pre-edge area provides useful information about orbitals, electron configurations and the symmetry (XANES) whereas the edge reveals information about the charge on the absorber. Beyond the absorption edge is designated as EXAFS.
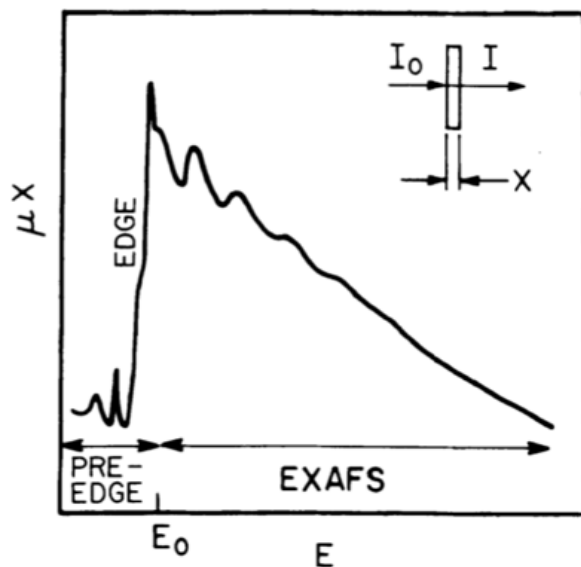
Figure 24. X-ray absorption spectrum for a K-edge transmission. The energy level of the X-ray is higher than the energy threshold (Teo 1981)

1.6.2. EXAFS

Beyond the absorption edge, the absorption intensity is modulated by back-scattering of the emerging photoelectron wave of the ionized core electron by nuclei in the immediate environment of the absorbing nucleus, which gives rise to extended X-ray absorption fine structure (EXAFS).

EXAFS has been around for quite a while, although being utilized to extract structural information from it is relatively a recent development (Teo 1981). Each scattering nucleus at a given distance from the absorbing nucleus will contribute a damped sine-wave oscillation in the absorption as the X-ray energy is increased, this is because of alternate constructive and destructive patterns of interference due to the back-scattered wave. EXAFS provides information about the identity, number and distances of ligands coordinated to the absorbing nucleus, but provides little direct information about coordination geometry under normal circumstances (Vlaic and Olivi 2004).

If the energy levels are higher than ground state to LUMO transition, it will be sufficient to release an electron to the continuum or in other words ionize the atom. The excess amount is in the form of kinetic energy. The effects can be seen in the wavelength associated with the electron (Yano and Yachandra 2009). Once the photoelectron is ejected, it goes through a phase shift. If there is a similar compound available as a model that has similar phase shifts, then the distances of the back scatterers (the atoms surrounding the absorber) can be obtained from that model. The amplitude of each wave depends on multiple factors including the number of the back scatterers, their power of back scattering, and the distance they have from the absorber. By obtaining these data, one can assess the number and distance of the surrounding atoms from the atom of interest (Yano and Yachandra 2009). The advantage that EXAFS has relative to other structural studies is the fact that if there are impurities or other material that are not directly bound to or in the vicinity of the absorber then they have zero influence on the data since the energy of the X-ray can be tuned to match the absorption edge of the atom of interest. (Teo 1981).

1.6.2.1. Sources for EXAFS

All the recent work in EXAFS utilizes synchrotron radiation which has a great signal to noise level relative to other traditional methods (Teo 1981). Synchrotron radiation has been described in more detail in section 1.4.4.

1.6.2.2. EXAFS data analysis

For analysis of EXAFS data, it is necessary to resolve the data so that there are individual waves for each type of neighboring atoms. In order to do so, there are two methods: Fourier transform or curve-fitting. Curve-fitting requires a model, that the structural parameters of it are known. Fourier transform produces a photoelectron scattering profile as a function of radial distance from the absorbing atom. In this profile, the positions of the peaks are related to the distance between the back scatterers and the absorber. The other most important information these peaks provide is that their size is related to the number of atoms and their types surrounding the absorber (Teo 1981).

In both methods, absorption coefficient (μx) vs energy (E) data is converted to $\chi(k)$ in reference to k. k represents the wavenumber in the reciprocal space. $\chi(k)$ gets multiplied by some power of k, hence the diminishing the amplitudes at high k values. $k^n\chi(k)$ where n is 3 is the most common factor used.

In FT method, the $k^n\chi(k)$ gets transformed (in momentum (k)) which gives a radial distribution function ρ_n (r') in distance (r') as demonstrated in the equation below (Teo 1981).

$$\rho_n(r') = \frac{1}{(2\pi)^{1/2}} \int_{k_{min}}^{k_{max}} k^n \, \chi(k) e^{i2kr'} dk$$

(Teo 1981)

71

In this equilibrium, there is a shift from the true distance by α. α depends on the element and can vary from 0.2 to 0.5 Å. Moreover, α can be obtained from a model and used for unknown samples.

Meanwhile, the curve fitting method is all about finding the best fit, meaning the least refinements needed curve, where it is $k^n\chi(k)$ spectra in k space. There are different ways of refinement such as least-square or absolute-difference minimization (Teo 1981).

Both curve fitting and Fourier transform have their strong advantages. Fourier transform provides radial distribution function whereas curve fitting has much higher resolution and accuracy. This is especially true for samples with very small interatomic spaces. Naturally both techniques have weaknesses as well. With the Fourier transform, you will need to deal with the side lobes and the shape. Moreover, the location of the peaks can be affected by weighting schemes. On the other hand, the curve fitting approach is overflowing with number of variables to analyze. The solution is to compromise between these two methods which would mean to transform the data followed by fitting with the most suited model (Teo 1981).

Chapter 2

Methods

2.1. FdsDABG from *Cupriavidus necator*

2.1.1. Plasmid construction, cloning and expression of FdsDABG from *Cupriavidus necator*

The plasmid currently used to express FdsDABG was attained by modifying the pTrc12HLB-FdsGBAD construct. The 6xHis-linker-6xHis tag at the N-terminus of FdsG was replaced with Twin-Strep tag (IBA, Gottingen, Germany). The 28 amino acids assembling the tag are: WSHPQFEKGGGSGGGSGGSAWSHPQFEKSG, and the plasmid designated pTrc-strep-FdsDABG. The construction of this plasmid was outsourced (Epoch Life Science, Sugar Land, TX). Overexpression of the recombinant protein was accomplished by transforming pTrc-strep-FdsDABG into *E. coli* DH5α cells. 50 mL of preculture consisting of TB (terrific broth) medium described in Table 2, supplemented with 1 mM sodium molybdate and 100 μg/mL of ampicillin was inoculated and grown for 6 hours at 37°C, shaking at 300 rpm in a mini shaker. This pre-culture was used to inoculate four 6 L Erlenmeyer flasks containing 2 L of TB medium each with the supplements, i.e., 1 mM sodium molybdate, 100 μg/mL of ampicillin and 24 mg of ferric ammonium citrate (the initial OD_{600} was 0.002). The cultures were induced with 45 μM of IPTG (isopropyl-β-D-1-thiogalactopyranoside) immediately after inoculation and were shaken at 25 °C, 160 rpm for 24 hours, then left standing without shaking overnight. If the OD_{600} was lower than 0.5 at this point, the cultures were left at room temperature, otherwise chilled to 4 °C. Finally, the cells were shaken for an additional 8 to 12 hours approximately,

at 25°C and 180 rpm until they reached OD_{600} between 7 to 10 and then harvested by centrifugation. Cell pastes were flash-frozen in liquid nitrogen and stored at -80°C freezer until used (Hakopian, Niks, and Hille 2022).

TGYEP (2 L)	TB (2 L)
Tryptone (40 g)	Tryptone (24 g)
Yeast (20 g)	Yeast (48 g)
$NaHPO_4$ (10 g)	K_2HPO_4(dibasic) (18.8 g)
Glucose (8 g)	KH_2PO_4(monobasic) (4.8)
Glycerol (50% stock) (32 mL)	Glycerol (50% stock) (16 mL)
1 mM Na_2MoO_4	1 mM Na_2MoO_4

Table 2. Medium for *E. coli*, bacterial growth. TB was used for both FdsDABG and FdsBG. TGYEP was used for FdhF.

2.1.2. Cell lysis and purification

Frozen cells were thawed and resuspended in 50 mM HEPES buffer with 10 mM potassium nitrate (KNO_3) pH 7.5 supplemented with DNase I, lysozyme, 1 mM sodium fluoride (NaF), 1 mM benzamidine HCl and 1 mM PMSF (phenylmethylsulfonyl fluoride) at 4 ℃ and lysed using a French press at a pressure of 15000 psi. The lysate was spun down in the ultracentrifuge at 179200xg for 45 minutes to an hour at 4°C to remove the cell debris. The supernatant was flash frozen in liquid nitrogen and stored in -80°C freezer until needed. The supernatant was thawed on ice at 4°C. 12 mL Strep Tactin® XT

Superflow® resin (IBA, Gottingen, Germany) was used in a 2.5-cm diameter gravity column to purify. The column was equilibrated with 50 mM HEPES buffer pH 7.5 with 10 mM KNO_3. With a flow of less than 0.5 mL/min, the supernatant was loaded on the column by gravity. 30 to 40 column volumes of the binding buffer was used to wash the bound enzyme after loading. The enzyme was eluted off the column with 50 mM HEPES buffer pH 7.5 with 10 mM KNO_3 and 50 mM biotin. Next, the crude protein was loaded onto a 2.6 × 11 cm Fractogel TMAE 650 (S) anion exchange column (Sigma-Millipore) equilibrated with 40 mM potassium phosphate (KPO_4) pH 7.0 with 10 mM KNO_3 on an Akta FPLC apparatus (GE healthcare) with a flow rate of 0.8 mL/min in order to separate active FdsDABG from inactive enzyme as well as a FdsBG subcomplex. The column was washed with 0.5 column volumes of the same buffer overnight and eluted with a linear gradient of 0.15 – 0.25 sodium chloride over six column volumes. The fractions associated with the peaks in the chromatogram, monitoring elution at 280 nm were assayed for enzyme activity (see below). Active fractions corresponding to the peak that contained active FdsDABG were combined, made 50% in ammonium sulfate and centrifugated 5488xg for 20 minutes. The pelleted protein was resuspended in a minimum amount of 50 mM HEPES buffer pH 7.5 with 10 mM KNO_3. For kinetic experiments the enzyme was exchanged into 50 mM HEPES buffer pH 7.5 with 10 mM KNO_3 using a PD-10 column, concentrated by ultrafiltration with an Amicon Ultra with a MWCO of 50,000 Da and flash-frozen in liquid nitrogen and stored in under liquid nitrogen until needed. For X-ray crystallography, the protein was loaded on a 1.6 × 60 cm Superdex 200 PG gel filtration column (GE healthcare) to separate the monomer and dimer FdsDABG. Fractions were

collected separately, concentrated by ultrafiltration and flash frozen in liquid nitrogen and stored in liquid nitrogen Dewar.

2.1.3. Activity assay

All activity measurements and absorbance spectra were carried out using a Hewlett-Packard 8452A diode array spectrophotometer equipped with a temperature-controlled cell holder, with the temperature maintained at 30°C. A solution containing 40 mM sodium formate, 20 mM NAD$^+$, 75 mM KPO$_4$ pH 7.7 was used as the assay mix. Formation of NADH was monitored at 340 nm ($\varepsilon = 6{,}022$ M^{-1} cm^{-1}), with the slopes obtained from the first 10 seconds after addition of enzyme. Pure and active FdsDABG exhibits around 70 units per mg of protein, calculated based on an extinction coefficient 51,500 M^{-1} cm^{-1} at 410 nm (Niks et al. 2016).

2.1.4. pH stability of FdsDABG

An overlapping system of buffers was used to determine the pH dependence of FdsDABG, consisting of 75 mM of each of the following: Tris, potassium phosphate, maleate, and glycine over the pH range 5.0 to 10.5 (Niks et al. 2016). The pH was adjusted in each case using potassium hydroxide or concentrated hydrochloric acid, as appropriate. In order to investigate the stability of FdsDABG, the enzyme was incubated in each buffer for one hour and the UV/Vis spectrum recorded to assess turbidity. To be certain that the enzyme was fully active and stable in the range mentioned above, the formate/NAD$^+$ assay was conducted in each pH by adjusting the assay mix to the desired pH that the enzyme is at any given sample. Due to the high concentrations of salt used, the correct pH of each buffer was determined from a 1:5 dilution.

2.1.5. pH dependence of reductive half reaction

For all rapid-reaction experiments, SX-20 stopped-flow spectrophotometer (Applied Photophysics Ltd., Leatherhead, Surrey, UK) was incubated with buffer containing catalytic amounts of glucose oxidase (*Aspergillus niger*, Sigma, G2133), catalase and 10 mM glucose the day before. The day of the experiment, the lamp was turned on at least 3 hours before the start of the experiment and the water bath was bubbled with UHP-grade nitrogen gas for 3 hours prior to the experiment.

To perform the stopped-flow experiment, FdsDABG in 20 mM HEPES buffer pH 7.2 with 10 mM KNO_3 was transferred to the anaerobic chamber and KNO_3 removed by running through a PD-10 column. The enzyme was sequentially diluted into each overlapping system buffer with appropriate pH (from ~5.7 to 9.3) to give a final concentration of 4 µM, placed in an anaerobic tonometer, removed from the anaerobic chamber and immediately transferred to the stopped-flow spectrophotometer. For this experiment, a photomultiplier tube detector was given the expected fast rates of reaction. In a typical experiment, an anaerobic solution of buffer with 4 mM sodium formate was mixed with the enzyme and the reaction monitored by the absorbance decrease at 450 nm. The steady-state activity of the enzyme was measured prior to the experiment by the formate/NAD^+ assay described above, with enzyme typically exhibiting an activity of 90 % or more.

2.1.6. Steady state assay monitoring reduction of carbon dioxide

The reduction of CO_2 by FdsDABG was previously demonstrated the 6xhis-linker-6xhis construct of FdsDABG (Yu et al. 2017). In the present work, a different construct for recombinant FdsDABG that was twin-Strep tagged FdsDABG. In addition, catalytic amounts of carbonic anhydrase were added to one of the samples. This steady state assay was done using a UV/Vis spectrophotometer (a Hewlett-Packard 8452A diode array spectrophotometer). All samples contained 1.6 nM of FdsDABG and 200 μM of NADH in a sealed cuvette (purged with argon gas prior to the experiment) under anaerobic conditions at 30 °C, the reaction being monitored at 340 nm. One consisted of 100 mM of sodium bicarbonate at pH 7.0, and a second one as a control, consisting of the same solution, but aerobic. Another solution was made anaerobically including the NADH but no sodium bicarbonate. One sample was made with saturated CO_2. In order to achieve CO_2 saturation, the sample was bubbled with CO_2 gas, and the pH was measured simultaneously until it was stabilized at 6.3. The sample's pH was manipulated with KOH. The concentration of CO_2 was approximately 29.5 mM. At last, a sample was made with 10 μM carbonic anhydrase, 100 mM sodium bicarbonate and 1 minute incubation (Yu et al. 2017; Niks et al. 2016).

2.1.7. Sample preparation for EXAFS

In order to determine the optimum pH for maximal Mo (V) formation in FdsDABG for XAS analysis, three EPR samples were prepared in 4 mm precision quartz (PQ) EPR tubes. Each contained 14.0 μM FdsDABG in 50 mM MES buffer pH 6.5, 50 mM HEPES buffer pH 7.5 or 50 mM Tris pH 9 respectively were prepared; each sample contained 10

mM final potassium nitrate (KNO_3). Samples were made anaerobic by purging argon gas for 30 minutes at which dithionite was added to a final concentration of 2 mM and flash-frozen in dry ice/acetone after a 2-minute incubation. EPR spectra were recorded at 30 K temperature, averaging nine spectra.

Four different EXAFS samples, in each case 1.1 mM (measured by (UV/Vis) with 100% activity (measured by the formate/NAD^+ assay) FdsDABG were prepared. The first three samples were in 50 mM HEPES buffer pH 7.5 with 10 mM KNO_3, and included the oxidized form of the enzyme, enzyme reduced by formate (anaerobic) and a form that had been inactivated by treatment with superoxide ion. For this third sample, 330 M xanthine and 0.01 M xanthine oxidase were added after the removal of KNO_3. After 10 minutes of incubation, the enzyme was fully inactivated and the 10 mM KNO_3 was added back to the sample to have a homogenous set of samples. A fourth sample was prepared in 50 mM MES buffer pH 6.5, again with 10 mM KNO_3. All samples were flash frozen in their corresponding cuvettes and stored in the liquid nitrogen Dewar until shipment to Stanford synchrotron radiation light source (SSRL) for use by our collaborator, Dr. Graham George (University of Saskatchewan).

2.1.8. Electrochemistry

Electrochemical studies of FdsDABG have been conducted with a second collaborator, Dr. Paul Bernhardt in University of Queensland. Dr. Bernhardt and coworkers have conducted UV/Vis electrochemistry, EPR redox titration and cyclic voltammetry for the aims mentioned above. The goal is, among other things, to determine

the reduction potentials of the several redox-active centers in the enzyme as well as to illustrate that the conversion between formate and CO_2 is reversable for FdsDABG.

In a typical experiment, FdsDABG is mixed with 4 mM solutions of mediator dyes such as methylene blue, 2,5-dihydrobenzoquinone, 2-hydroxynaphthoquinone, anthraquinone-2-sulfonate, indigo-5,5′,7-trisulfonate, benzyl viologen and methyl viologen, then titrated with 10 mM sodium dithionite until a stable oxidation-reduction potential is achieved. Once equilibrium is reached samples are withdrawn for EPR spectroscopy, the intensity of each EPR signal being potential dependent. The method is described in detail in a publication from a previous collaboration with Dr. Bernhardt (Kalimuthu et al. 2020).

This experiment is conducted with a Pine instruments quartz spectroelectrochemical cell (1.7 mm optical path length). A Pt working electrode, a Pt auxiliary electrode and an Ag/AgCl reference electrode calibrated with quinhydrone were utilized. The UV/Vis spectra of FdsDABG were acquired in an anaerobic chamber after the potentials with a certain increment via a potentiostat had been set and applied. The signals in the spectra were correlated to the potentials employed (Kalimuthu et al. 2020).

Cyclic voltammetry (CV) experiments were conducted using either a BAS 100B/W or BASi Epsilon Eclipse potentiostat. A three-electrode system was used, consisting of a glassy carbon (GC) disk as the working electrode, a platinum wire as the counter electrode, and an Ag/AgCl reference electrode. The reference electrode was calibrated using quinhydrone, with a potential of +285 mV versus the normal hydrogen electrode (NHE) at

pH 7. All applied potentials are reported relative to the NHE. Prior to the experiments, the solutions were purged with argon (Ar) gas for a duration of 30 minutes. A small amount of active FdsDABG was immobilized on a glass carbon (GC) electrode. The optimal composition of the film included 2 µL of chitosan (0.25%), 2 µL of GTA (0.25%), and 3 µL of FdsDABG (86 µM). Methyl viologen (MV), methylene blue (MB), and phenazinium (PMS) were utilized as redox mediators to facilitate artificial electron transfer in place of NAD^+ during the FdsDABG catalytic process.

2.1.9. Aerobic inactivation of FdsDABG

Four samples of 1 µM FdsDABG were prepared and incubated overnight at 4 °C. All samples were in 50 mM HEPES buffer, pH 7.2. One sample contained superoxide dismutase (from bovine erythrocytes, Worthington Biochemical Co.) and 4 nM of catalase (from bovine liver, Sigma, C-40). The remaining samples contained 10 mM KNO_3, 4 nM catalase, and two samples of no additives (enzyme only) respectively. UV/Vis absorbance and activity assays were obtained using a Hewlett-Packard 8452A diode array spectrophotometer. The formate/NAD^+ assay was used to assess the activity of the samples. One sample with no additives was incubated in the dark while the other was left in ambient light. To verify that the sample in the presence of the superoxide dismutase retained activity after the overnight incubation, samples containing dismutase, KNO_3 and no additives were purged with argon gas for 15 minutes to become anaerobic, subsequently reduced with 2 mM sodium formate and analyzed spectroscopically (Hakopian, Niks, and Hille 2022).

In a second experiment, three samples of 1 μM FdsDABG were each incubated with (1) 100 units of superoxide dismutase, (2) 10 mM KNO_3 and (3) no additive overnight at 4 °C. The next day they were purged with argon gas for 15 minutes to become anaerobic, subsequently reduced with 2 mM sodium formate and analyzed spectroscopically (Hakopian, Niks, and Hille 2022).

2.1.10. Protection against external source of superoxide

All samples contained 1 μM FdsDABG, 330 μM of xanthine, 4 nM catalase and 0.1 μM of xanthine oxidase in 50 mM HEPES buffer, pH 7.2. The samples were incubated with 100 units of superoxide dismutase, 10 mM KNO_3 and no additive, respectively. Two additional samples were made with 0.01 μM xanthine oxidase and no xanthine oxidase. All samples were incubated at 4 °C for 60 minutes, with activities measured every 15 minutes (Hakopian, Niks, and Hille 2022).

2.1.11. Detection of superoxide:

1 μM of active FdsDABG was incubated with 40 mM sodium formate and 25 μM cytochrome *c* (from horse heart, Sigma, C-7752) both in the presence and absence of 500 units of superoxide dismutase, respectively. The reactions were carried out in 50 mM HEPES buffer, pH 7.7 with 10 mM KNO_3 and 4 nM catalase. The reduction of cytochrome *c* was monitored at 550 nm at 20 °C for 10 minutes (Hakopian, Niks, and Hille 2022).

2.1.12. Detection of intermolecular electron transfer by stopped-flow spectrophotometry

Reduction of cytochrome c by FdsDABG was performed under anaerobic conditions using a SX-20 stopped-flow spectrophotometer equipped with PDA detector. The spectrophotometer was made anaerobic by overnight incubation with 50 mM HEPES buffer, pH 7.2 containing 10 mM glucose and catalytic amounts of catalase and glucose oxidase (*Aspergillus niger*, Sigma, G2133). 5 μM of active FdsDABG was incubated with 40 mM sodium formate and loaded on to a PD-10 column to remove the excess sodium formate after reduction of FdsDABG in the anaerobic chamber. The PD-10 column was incubated in 50 mM HEPES buffer, pH 7.2 with 10 mM of glucose and catalytic amounts of catalase and glucose oxidase three days prior to the experiment. As a consequence, FdsDABG was incubated in 50 mM HEPES buffer, pH 7.2 containing 40 nM glucose oxidase, 8 nM catalase and 30 units of superoxide dismutase. 25 μM of oxidized cytochrome c was also made anaerobic by being purged with argon gas prior to being transferred to the stopped-flow spectrophotometer. The reaction was performed at 20°C (Hakopian, Niks, and Hille 2022).

2.1.13. Reduction of FdsDABG by superoxide

2.3 μM of FdsDABG was reduced by 0.01 μM of xanthine oxidase under anaerobic conditions in the presence of 10 mM KNO_3. Both enzymes were incubated in 50 mM HEPES buffer, pH 7.2, including 330 μM xanthine and 4 nM catalase. UV/Vis spectra were obtained after 60 minutes of incubation (Hakopian, Niks, and Hille 2022).

2.1.14. Sulfite generation

5-10 mM sodium formate in 50 mM HEPES buffer, pH 7.2 was mixed with > 10 μM of FdsDABG and incubated at 4 °C under aerobic conditions. The enzyme was inactivated after 24 hours and removed by a 30 kDa MWCO AmiconUltra. The flowthrough containing sulfite was made anaerobic and transferred to the anaerobic chamber. The atmosphere in the anaerobic chamber consists of 2.5% H_2/N_2 (Coy Labs, Inc). Approximately 20 μM of human sulfite oxidize (hSO) in the presence catalytic amounts of glucose oxidase and catalase and 10 mM glucose was mixed with the flowthrough and incubated for an hour in the anaerobic chamber. Next, the sample was sealed in a quartz cuvette with a septum and transferred outside. After the necessary correction for the hSO absorbance in the absence of sulfite, meaning that the control sample was diluted to the same amount of hSO present in the mixture with the flowthrough, under anaerobic conditions the formation of reduced hSO at 556 nm was monitored (Hakopian, Niks, and Hille 2022).

2.1.15. Crystallization

The crystallography plates were transferred into the anaerobic chamber at least a week prior to the experiment to ensure that the O_2 embedded in the plastic was scrubbed. All solutions and chemicals used were bubbled with ISP-grade nitrogen gas for at least 20 minutes and incubated in the anaerobic chamber for at least three days prior to use. The day of the experiment, 10-15 mg / mL of active FdsDABG, in 50 mM HEPES buffer, pH 7.2 including 10 mM KNO_3 was thawed on ice. The enzyme was centrifuged at 14000 rpm for 30 minutes at 4 °C. Next, the enzyme was transferred into a V-shaped glass vial

and was sealed with a septum. The enzyme was made anaerobic by purging argon gas into the vial for 20 minutes while the vial was incubated on ice. Subsequently, the vial was transferred into the anaerobic chamber on to the cooling beads at 4 °C. After the oxygen levels were stabilized and the extra amount was scrubbed, the enzyme was ready to be pipetted into 24 well or 96 well sitting drop plates. The crystallization buffers kit used for initial screening were: The AmSO$_4$ suite from QIAGEN, The Hampton CSI, CSII, SaltRx1 and SaltRx2. Table 3-5 are the main buffers, salts and additives used after the initial screens for not only for FdsDABG but also for FdhF from *P. atrosepticum*.

Sodium actetate pH=4.6	Sodium actetate pH=4.7	Sodium actetate pH=5.0	Sodium actetate pH=5.2	Sodium actetate pH=5.4	Sodium actetate pH=5.6
MES pH=5.64	MES pH=5.8	MES pH=6.0	MES pH=6.1	MES pH=6.2	MES pH=6.3
MES pH=6.4	MES pH=6.5	MES pH=6.6	MES pH=6.7	MES pH=6.8	HEPES pH=6.8
HEPES pH=7.0	HEPES pH=7.1	HEPES pH=7.3	HEPES pH=7.5	HEPES pH=7.8	Tris-HCl pH=8.5

Table 3. Buffers used for both formate dehydrogenase crystallization.

Magnesium formate dihydrate	Magnesium chloride	Magnesium acetate trihydrate
Lithium chloride	Lithium sulfate	Iron (III) chloride hexahydrate
Sodium formate	Sodium phosphate monobasic	Sodium acetate trihydrate
Sodium citrate tribasic dihydrate	Potassium phosphate monobasic	Potassium tartrate tetrahydrate
Zinc acetate dihydrate	Cobalt (II) chloride hexahydrate	Cadmium chloride hydrate
Cesium chloride	Nickel (II) chloride hexahydrate	Cadmium sulfate hydrate
Ammonium sulfate	Ammonium acetate	Ammonium phosphate monobasic
Ammonium formate	Calcium acetate hydrate	Calcium chloride dihydrate

Table 4. Salts used for both formate dehydrogenase crystallization.

1,4-Dioxane	Polyethylene glycol 400	Polyethylene glycol 1500	Polyethylene glycol 2000
Polyethylene glycol 3350	Polyethylene glycol 4000	n-propanol	2-propanol
Triethylamine	Dimethyl sulfoxide	Methanol	Ethanol
Ethylene glycol	Polypropylene glycol	Glycerol	MPD

Table 5. Organic compounds used for both formate dehydrogenase crystallization.

2.2. FdsBG from *Cupriavidus necator*

2.2.1. Cloning and expression

The starting plasmid, pTrc12HLB-FdsDABG was modified such that the genes encoding the D and A subunits were deleted and the 6xHis-linker-6xHis tag was replaced with a Twin-Strep tag (IBA, Gottingen, Germany) on FdsG to give a plasmid designated pTrc-strep-FdsBG. Construction of this plasmid was outsourced (Epoch Life Science, Sugar Land, TX).

The plasmid was transformed into *E. coli* DH5α cells and overexpressed. 50 mL of preculture consisting of LB (Luria broth) medium supplemented with 100 μg/mL of ampicillin was grown overnight at 300 rpm and 37°C. The overnight culture was used to inoculate two 6 L Erlenmeyer flasks, each containing 2 L of TB (terrific broth) medium supplemented with 100 μg/mL of ampicillin. These cells were grown at 30°C, 200 rpm to an $OD_{600} = 0.4$ when they were induced with 0.25 mM IPTG. After induction, the cells were grown for an additional 16 hours at 30°C, 160 rpm to final OD_{600} anywhere from 12 to 16. Cells were harvested, flash frozen in liquid nitrogen and stored in -80°C freezer (Young et al. 2020).

2.2.2. Cell lysis and purification

All steps were performed at 4°C or on ice. Cells were thawed and resuspended in 50 mM HEPES buffer pH 7.5 in the presence of DNase I, lysozyme, 1 mM NaF, 1 mM benzamidine HCl and 1 mM PMSF. The cells were pressed once through a French press at 15000 psi. The cells debris was removed by ultracentrifugation, at 179200xg, for one hour and the supernatant loaded on a 12 mL Strep Tactin® XT Superflow® resin (IBA,

Gottingen, Germany) in a 2.5-cm diameter gravity column which had been equilibrated in the same buffer that the cells were resuspended with. After 30 column volumes of washing with the same buffer, the protein was eluted with 50 mM HEPES buffer pH 7.5 with 50 mM biotin. The eluent was concentrated by ultrafiltration with an Amicon Ultra with a 50,000 Da cutoff and buffer exchanged using a PD-10 column into 10 mM HEPES buffer pH 7.2. The enzyme was aliquoted and flash frozen in liquid nitrogen and stored under liquid nitrogen (Young et al. 2020).

2.2.3. Crystallization

The Strep-tagged FdsBG was crystallized by vapor diffusion in a sitting drop method under anaerobic condition. 2 μL of FdsBG with 15 mg / mL concentration were mixed with 1 μL of the reservoir solution and set up over 500 μL of reservoir solution. All the solutions and chemicals used were bubbled as mentioned earlier prior to use. 5 mM DTT was added to the enzyme stock solution before the plates were set up. The condition that resulted in FdsBG crystals was 2-3 % isopropyl alcohol, 1.4 M ammonium sulfate in 100 mM HEPES buffer, pH 7.5 at 14 °C. Crystals were formed within three days. Before preparing the crystals for X-ray diffraction collection, they were stabilized in additional reservoir solution with no isopropyl alcohol but increasing concentration of glycerol to a final of 24% (v/v). After stabilization, the crystals were mounted, and flash frozen in liquid nitrogen.

For the NADH-bound complex, the pre-formed crystals which were achieved from the procedure mentioned above, were soaked for 45 minutes in final stabilization solution

containing 10 mM NADH before mounting and flash freezing in liquid nitrogen (Young et al. 2020).

2.3. FdhF from *Pectobacterium atrosepticum*

2.3.1. Cloning and expression

Two plasmids are required for expression of functional FdhF from *Pectobacterium atrosepticum*, PEQ80 and a second encoding the FdhD sulfurase inserts the catalytically essential Mo=S sulfur into the molybdenum center of FdhF. PEQ80 was modified so that the Twin-Strep tag (IBA, Gottingen, Germany) was changed to Strep-SUMO-FdhF. Both plasmids were chemically transformed into *E. coli* CLK002 cells and glycerol stocks were made. 80 mL of preculture consisting of TGYEP medium described in Table 2, supplemented with 100 μg/mL of ampicillin and 50 μg/mL of kanamycin, 10 μM of sodium molybdate was grown overnight at with shaking 300 rpm and 37°C. The overnight culture was used to inoculate two 3 L Erlenmeyer flasks, each containing 2.0 L of TGYEP medium supplemented with 100 μg/mL of ampicillin, 50 μg/mL of kanamycin, 10 μL of sodium molybdate and 50 μM of IPTG. The starting OD_{600} for the large-scale growth was 0.2 and right after inoculation the flasks were made anaerobic by purging argon gas into the sealed, vented flasks. The flasks were continuously grown at room temperature for 24 hours after induction. 1 L centrifugal bottles were transferred to the anaerobic chamber at least one day prior to harvesting cells. The culture flasks were placed in an anaerobic chamber and the cultures transferred to 1 L centrifugal bottles fitted with silicon O-rings that had equilibrated in the anaerobic chamber for at least one day. After centrifugation (outside the anaerobic chamber) the harvest cells were transferred to 40 mL centrifugal tubes fitted

with silicon O-rings. They were flash frozen in liquid nitrogen after being taken out of the anaerobic chamber and stored under liquid nitrogen until needed.

2.3.2. Cell lysis and purification

All steps were performed on cooling beads or in chilled centrifuge rotors at 4°C. All buffers were bubbled with N_2 gas for at least 20 minutes prior being transferred to the anaerobic chamber and contained 10 mM glucose. Buffers were purged with argon gas for 15 minutes and placed in the anaerobic chamber, then treated with a solution containing catalytic amounts of glucose oxidase from *Acidaminococcus niger*, bovine liver catalase and DTT (Dithiothreitol) to scrub residual O_2. 50 mM MES buffer pH 6.5 with 300 mM potassium chloride (KCl), 1mM DTT, in the presence of DNase I, lysozyme, 1 mM NaF, 1 mM benzamidine HCl and 1 mM AEBSF (4-benzenesulfonyl fluoride hydrochloride) was used to resuspend the cell pellets. Containers were kept closed until the O_2 level in the anaerobic chamber was stable and below 2 ppm. The French press in the anaerobic chamber was incubated with buffer for 30 minutes in order to scrub any oxygen in it and cells were incubated with the buffer for 10 minutes before lysis. Cells were pressed at 40,000 psi and the lysate was transferred outside the anaerobic chamber inside sealed ultracentrifuge tubes and centrifugated at 42,000 rpm for 30 minutes at 4°C. The clarified supernatant was returned to the anaerobic chamber, transferred into centrifuge tubes with silicon O-rings, then removed, flash frozen and stored under liquid nitrogen until needed. For purification all the glassware and plastics were transferred to the anaerobic chamber 3 days prior to use. A 5 mL Twin-Strep column was equilibrated with 50 mM MES buffer pH 6.5 with 300 mM potassium chloride (KCl), 1mM DTT, 1 mM glucose and catalytic

amounts of glucose oxidase and catalase. The supernatant was thawed in the anaerobic

chamber, placed in sealed centrifuge tubes and centrifuged at 15000 rpm for 15 minutes.

The clarified supernatant was then loaded at ~0.5 mL/min via a peristaltic tubing pump and

the column was washed with 20 column volumes of buffer at 1 mL/min. Protein was eluted

with 50 mM MES buffer pH 6.5 with 300 mM potassium chloride (KCl) and 1mM DTT

containing 25 mM biotin. The eluate was concentrated in Amicon Ultra centrifugal

concentrator with a MWCO of 50,000 Da that had been incubated with anaerobic buffer

and centrifuged for 6,500 rpm for 15 minutes. Once the concentrator with the protein was

transferred back to the anaerobic chamber, the purified FdhF was buffer exchanged on a

PD-10 column to remove the biotin equilibrated with the binding buffer.

2.3.3. Activity assay

Benzyl viologen (1-benzyl-4-(1-benzylpyridin-1-ium-4-yl) pyridin-1-ium 1,1'-

Bis(phenylmethyl)-4,4'-bipyridinium, BV) was used to measure the activity of FdhF. The

assay solution consisted of 2 mM BV, 40 mM sodium formate and 75 mM HEPES buffer

pH 7.5. The activity of FdhF was assessed by monitoring the reduction of BV by the

absorbance increase at 600 nm ($\varepsilon = 10{,}000\ M^{-1}\,cm^{-1}$). The slopes were calculated from the

first 10 seconds of the time course after the initiation of the reaction by addition of enzyme.

The enzyme concentration can be calculated based on the extinction coefficient $15{,}000\ M^{-1}\,cm^{-1}$ at 400 nm.

The activity of FdhF was independently gauged by the extent of spectral change

induced by formate as compared to dithionite. In a typical experiment, the absorption

spectrum of 6 μM of FdhF in 50 mM MES buffer pH 6.5 with 300 mM KCl and 1 mM

DTT was obtained using an Interstellar UV/Vis spectrophotometer inside the anaerobic chamber, and the protein then reduced with 5 mM final concentration of sodium formate. A second spectrum was recorded, after which the enzyme was reduced by excess sodium dithionite and a third spectrum recorded. Fractional activity was estimated by assuming the dithionite reduced spectrum is where enzyme is fully (100%) reduced and comparing the reduction level of the formate reduced sample to it.

2.3.4. Crystallography

The preparation of the crystal plates and solutions were done as mentioned earlier for the enzyme FdsDABG. Tables 2-4 represent the conditions tried for the inactive enzyme in addition to the original screens. 10 mg/mL of enzyme was used for crystallography with variation of 1:1 or 2:1 in the drops of protein versus reservoir solution.

2.3.5. Electron paramagnetic resonance

All EPR spectra were recorded via Bruker Magnettech ESR500 spectrometer equipped LTR-MS-5000. Acquisition software, ESR Studio 1.80.0, was used to baseline correct and process spectra as well as for the manipulation of spectra. The temperature was controlled via Bruker variable temperature unit and a liquid nitrogen cryostat. For anaerobic samples the PQ EPR tubes were left in the anaerobic chamber for at least 24 hours prior to sample preparation. Samples were prepared at 4°C. After the samples were transferred into the EPR tubes by Hamiltonian syringes, the tubes were sealed with rubber septa and transferred outside of the anaerobic chamber into dry ice / ethanol bath. After the samples were frozen the septa were removed carefully and the tubes were transferred into a liquid nitrogen Dewar.

EPR samples of 126 μM as-isolated FdhF enzyme reduced with 5 mM sodium formate were made in PQ EPR tubes in the anaerobic chamber and immediately upon being taken out. Spectra were recorded using a Bruker Magnettech ESR500 spectrometer.

CHAPTER 3

Protein purification and catalytic properties

3.1. FdsDABG expression and purification

The 6xHis-linker-6xHis tag of FdsDABG was successfully replaced with an N-terminal Twin-Strep tag since with the previous construct there were precipitation issues during protein purification. There was no precipitation observed with the new construct. Figure 25 shows the chromatogram from an anion exchange Fractogel TMAE 650 (S) column (Sigma-Millipore) column. The left-most peak is the FdsBG subcomplex which also gets expressed during the bacterial growth and gets co-purified with FdsDABG since the Twin-Strep tag is on the G subunit. The next two peaks are both FdsDABG, for reasons that are not clear. However, there is a correlation between the number and pattern of the peaks and the growth conditions: if the incubation time is anywhere between 1 h to 12 h starting when the OD_{600} is around 0.2-0.5, then there are only two peaks which are fairly well-separated. Otherwise, three peaks tend to be observed that bleed into each other. At this point, the protein is sufficiently pure (~95-100%) for kinetic experiments, but for crystallography experiments the protein is passed through a Superdex 200 PG gel filtration column (GE healthcare), which separates monomeric and dimeric forms of FdsDABG. The activity of each sample is monitored by the formate/NAD^+ assay as described in the experimental procedures section. The yield from 60 to 70 grams of cells is 10-15 mg of 100% active FdsDABG.
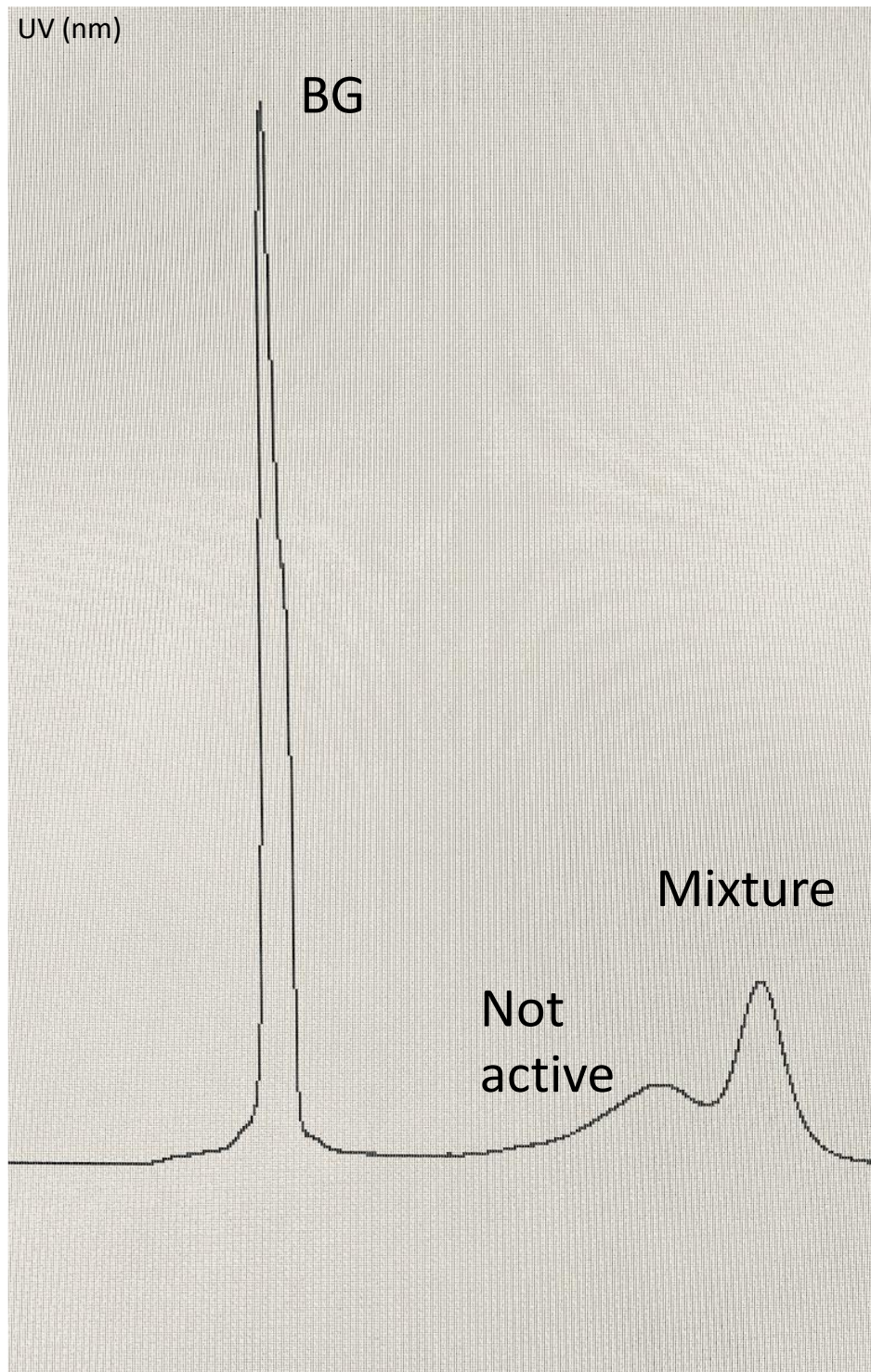
Figure 25. The chromatogram of FdsDABG purification. The eluate from the strep column runs through the TAME anion exchange column. From left, FdsBG, 0%-70% active FdsDABG and last peak contains 90%-100% active FdsDABG.

3.2. FdsDABG catalysis in the reverse direction

We first investigated the effectiveness of bicarbonate vs. CO_2 as a substrate in the reverse reaction, generating formate. As shown in Figure 26, samples with bicarbonate exhibited comparable activity to CO_2 under aerobic conditions, whereas the activity levels dropped close to zero with bicarbonate under anaerobic conditions. This indicates that with bicarbonate as a source for carbon dioxide, the activity observed from the aerobic sample is due to the diaphorase (NADH-O_2 oxidoreductase) activity of FdsDABG. On the other hand, when CO_2 is directly utilized under anaerobic conditions NADH consumption remains high. Addition of catalytic amounts of carbonic anhydrase under anaerobic conditions, greatly accelerating the aqueous interconversion of bicarbonate and CO_2, resulted in significant levels of consumption of NADH, affirming that CO_2 is the substrate for FdsDABG in the reverse direction.
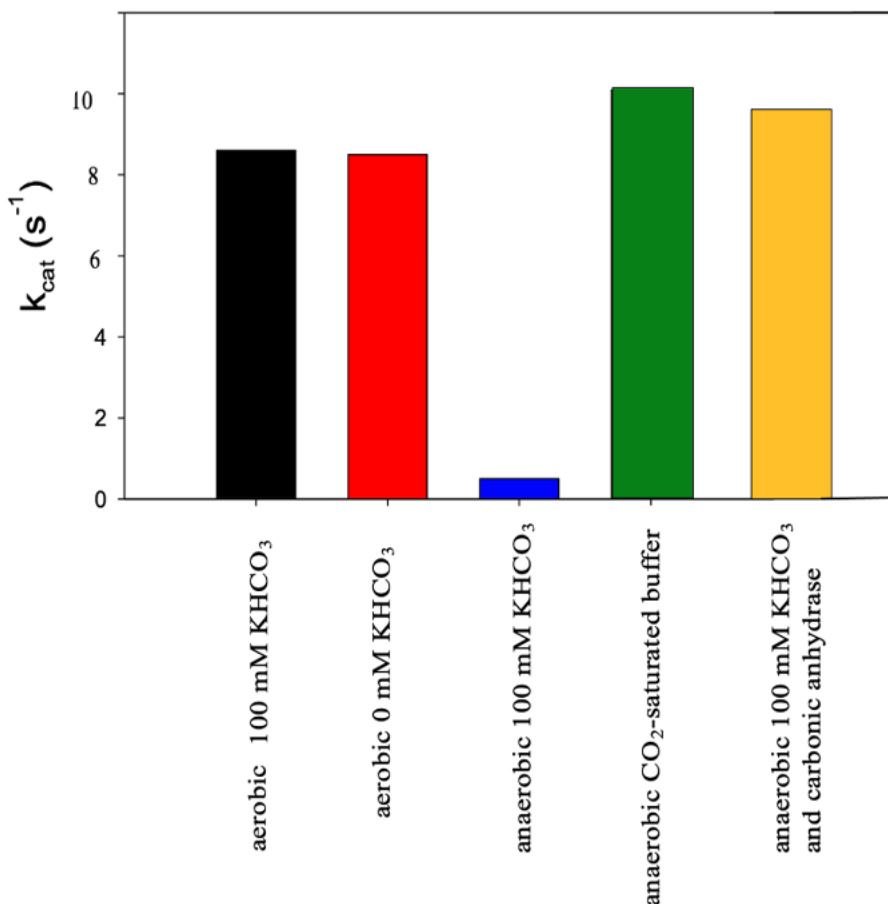
Figure 26. Reverse catalysis of FdsDABG. All reactions were started with the addition of 200 µM NADH, following the absorbance change at 340 nm due to NADH consumption (0.1 M potassium phosphate, pH 7.0 at 30°C). From left the samples are: aerobic, 100 mM KHCO₃(black) aerobic 0 mM KHCO₃ (red), anaerobic 100 mM KHCO₃(blue), anaerobic CO₂-saturated buffer (29.5 mM) (green), anaerobic 100 mM KHCO₃ and carbonic anhydrase (yellow).

3.2.1. Discussion

The outcome of this experiment has demonstrated that the substrate for the catalysis of the reverse reaction by FdsDABG is exclusively CO_2. Bicarbonate only gets utilized in the reverse reaction once processed by carbonic anhydrase to produce CO_2. Also, steady-state assays should be done under anaerobic conditions because FdsDABG exhibits considerable NADH:O_2 oxidoreductase ("diaphorase"). Both these factors are important

to keep in mind since many have claimed that formate dehydrogenases do not catalyze the reverse reaction and the evidence provided to support this conclusion when in fact most formate dehydrogenases likely catalyzed CO_2 reduction when CO_2 rather than bicarbonate is used as substrate without also adding carbonic anhydrase. It remains for future work to repeat the experiments done here with FdsDABG using other formate dehydrogenases such as FdhF from *E. coli*, or FdhF from *P. atrosepticum* to assess the general validity of these results.

3.3. pH dependence of the reduction of FdsDABG by formate

In order to determine the pH dependence of the rate of reduction of FdsDABG by formate, the pH-stability of the protein was first determined. In Figure 27 and 28, the UV/Vis spectra of FdsDABG diluted in an overlapping system of buffers over the pH range 5.7 to 10.3. It can be concluded that the protein is stable within the pH range of 5.7 to 10.3 with the exception of pH 8.3. At this pH, the enzyme gets precipitated, thus, the absorption levels decrease after centrifugation and removal of the pellet. Table 6 shows the percentage of active enzyme according to the formate/NAD^+ assay in the basic pH range mentioned above. In line with the data in the table the enzyme loses activity above pH 7.5 after within 30 minutes. This narrows down the range selected for the rapid reaction experiment in order to investigate the pH dependence of the reductive half reaction of the enzyme from pH 5.7 to ~9.3.

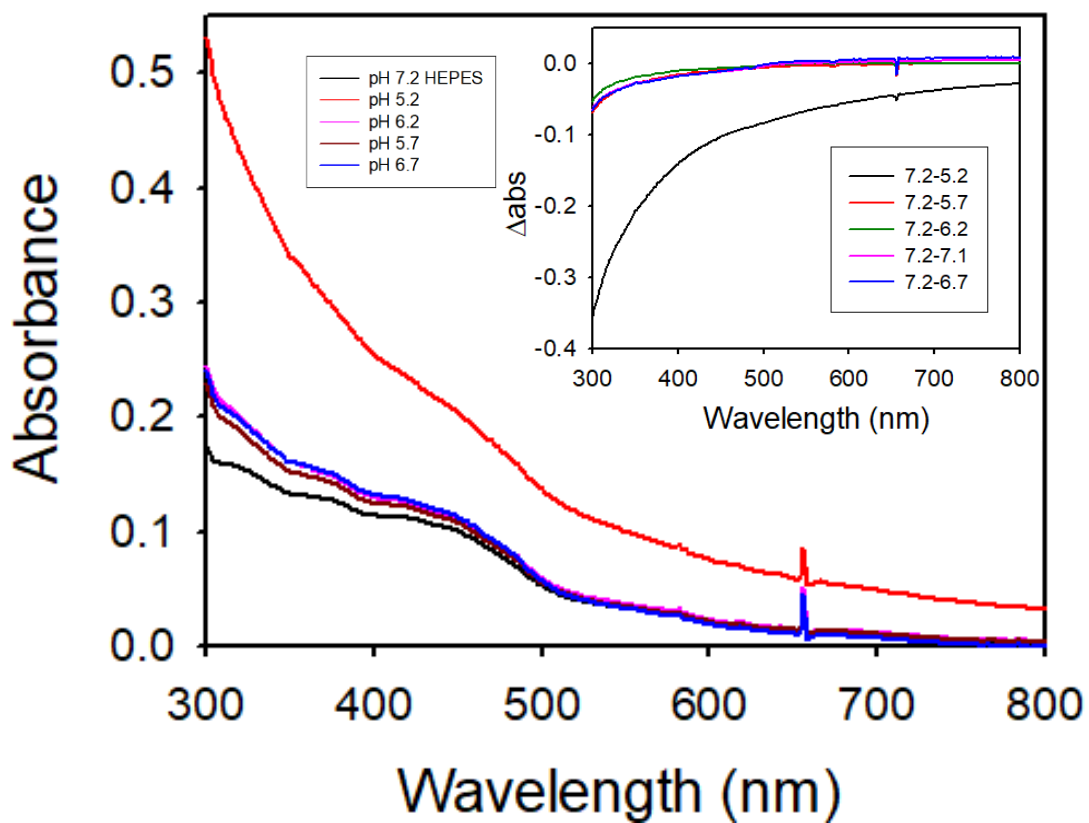**Figure 27.** UV/Vis spectra of FdsDABG in acidic pH. UV/Vis spectra of FdsDABG in the acidic pH range of the overlapping system were recorded after one hour of incubation. The inset represents the difference spectra during that one-hour incubation.

Figure 28. UV/Vis spectra of FdsDABG in basic pH. UV/Vis spectra of FdsDABG in the basic pH range of the overlapping system were recorded after one hour of incubation. The inset represents the difference spectra during that one-hour incubation.
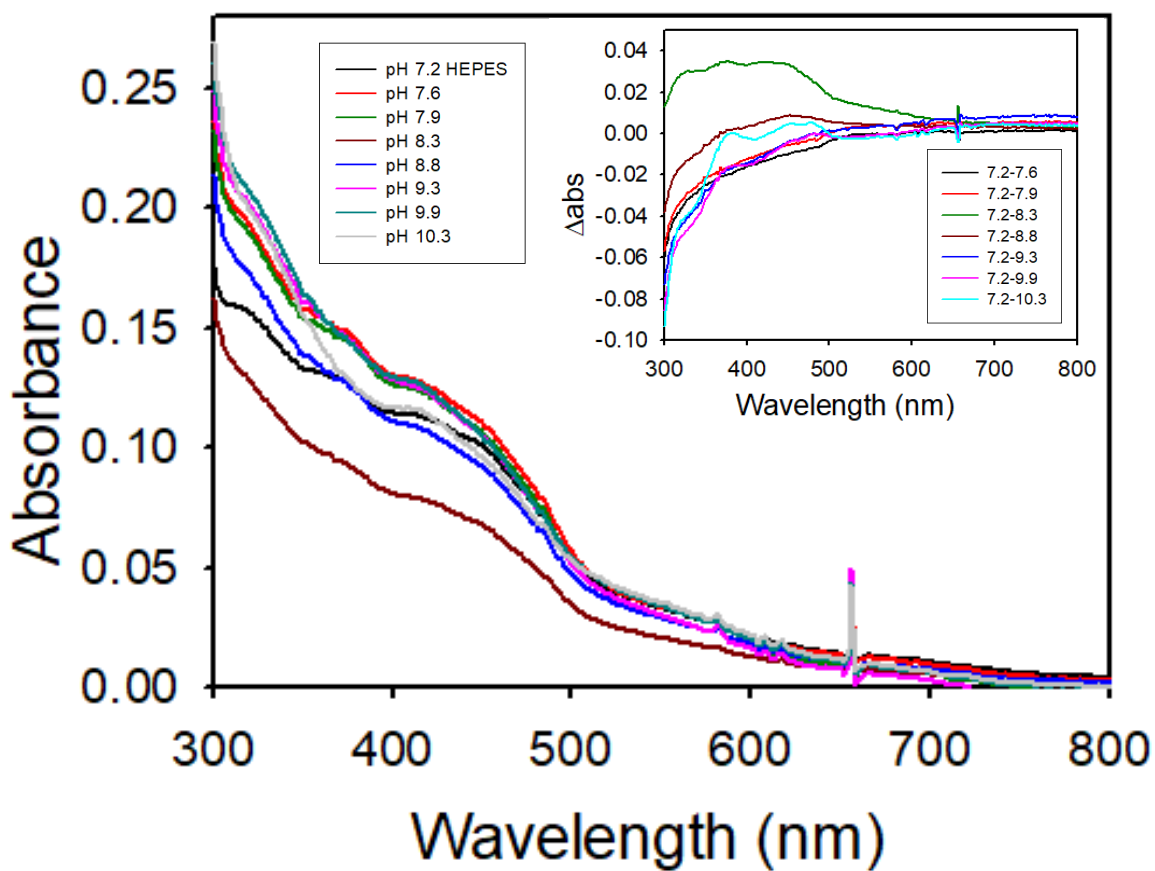
pH	% Activity (Immediately)	% Activity (30 minutes)
8.3	67.4	23%
8.8	52.9	12.5
9.3	41.2	0
9.9	17.94	0
10.3	0	0

Table 6. Percentage of activity of FdsDABG. Percentage of activity for FdsDABG in the basic pH range of the overlapping system was calculated. The activity is measured based on the formate/NAD$^+$ assay which its pH was also adjusted to pH in question. The activity levels were measured 30 minutes and 60 minutes after incubation.

The buffer systems used had pH values that empirically were found to be somewhat concentration-dependent. In Table 7, the pH measurements after dilution of the overlapping system buffer can be seen. These measurements were recorded before the rapid reaction experiment in the stopped-flow spectrophotometer was conducted to learn about whether the reductive half reaction of FdsDABG with sodium formate is pH dependent or not.

pH (expected)	pH (measured)
6.0	6.3
6.5	6.7
7.0	7.2
7.5	7.5
8.0	7.9
8.5	8.4
9.0	8.8
9.5	9.3

Table 7. pH discrepancies in overlapping buffer systems. Differences between the expected pH and the reality in the overlapping system buffer used for investigating the pH dependence of the reductive half reaction of FdsDABG were calculated and recorded. The high concentration of salt hence increase in the ionic strength interactions causes error while using the pH meter.

Having done the above, the rate of reduction of FdsDABG by formate was examined. The reaction is multiphasic, owing to the need for the enzyme to react with saturated amount of formate to become fully reduced. Only the fastest phase, corresponding to the reaction of the first equivalent of formate with fully oxidized enzyme, was analyzed in detail (Yu et al. 2017). The observed limiting rate at high [formate] exhibited only a modest pH dependence (Figure 29), decreasing from ~500 s^{-1} at pH 6 to 200 s^{-1} above pH 9. The time scale of the data collected is 10 seconds. The percentage of the total absorbance change occurring in the fast phase of the reaction as a function of pH

is presented in Table 8. The trend of the k_{obs} versus pH is shown Figure 29. All data was

repeated in triplicate.

pH	Percentage of fast phase
6.3	75
6.7	71
7.2	86
7.5	88
7.9	75
8.8	57
9.3	33

Table 8. Fast phase percentage of reductive half reaction for FdsDABG. The percentage of the fast phase of the reductive half reaction for FdsDABG with sodium formate was measured for buffers with different pH values. The highest percentage of fast phase belongs to the sample with pH 7.5.
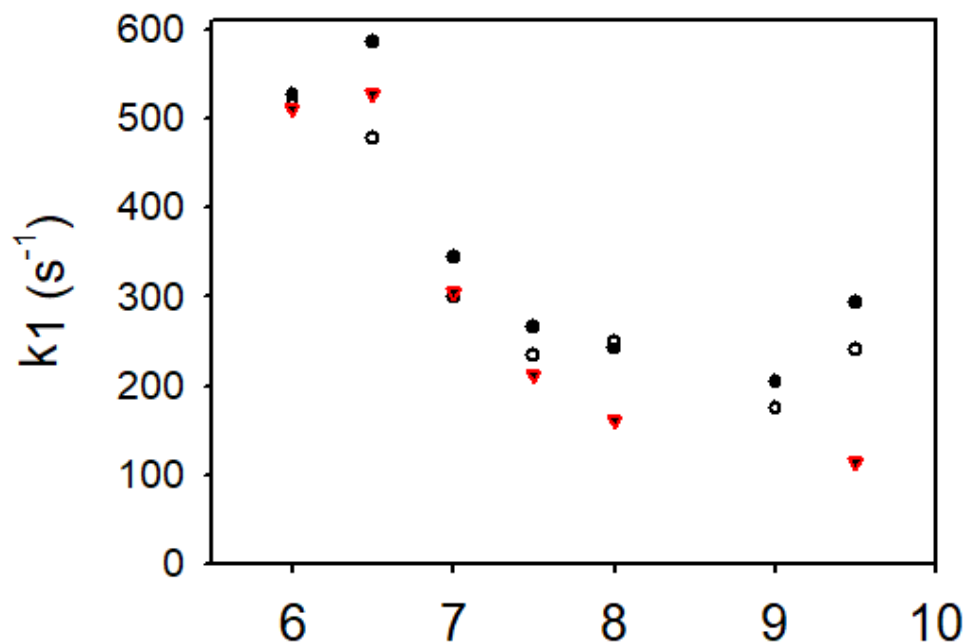
Figure 29. k_{obs} versus pH for the reductive half reaction of FdsDABG with sodium formate. Each dataset has been collected three times. The spread of the data is shown per pH in black dot, circle and red triangle. The catalysis is mildly acid facilitated.

3.3.1. Discussion

The pH dependence of the reductive half-reaction of FdsDABG indicates that acid/base catalysis does not contribute significantly to the mechanism of formate oxidation, a result consistent with a direct hydride transfer mechanism, but inconsistent with any mechanism involving base-assisted attack of, say, a Mo-OH group on formate. The modest, approximately threefold reduction in k_{red} in going from pH 6 to 9 may instead be due to the overall preference of the enzyme for more acidic environment rather than basic. In addition, there is always the increased risk of losing the catalytically relevant and labile sulfido ligand at higher pH. Future directions again include an examination of other formate dehydrogenases, in particular the formate dehydrogenase FdhF from *P. atrosepticum* since it is very similar to FdsDABG in possessing a cysteine coordinated to

the molybdenum, yet is a much simpler system containing only one iron-sulfur cluster rather than seven.

3.4. Ideal pH for Mo(V) signal

Detecting the Mo(V) signal will provide greater assurance for the proposed hydride transfer mechanism demonstrated in Figure 4 in the introduction section. It will affirm that during the reduction of the enzyme, the hydride actually gets transferred and is part of the molybdenum active site until the second electron oxidation step occurs. For the EXAFS experiment examining the partially reduced molybdenum center of FdsDABG, it is crucial to have as much of the sample as possible in the Mo(V) state, and so the pH dependence of Mo(V) generation was investigated. In Figure 30 the EPR signal of formate-reduced FdsDABG at three different pH values is shown. All three samples contain 14 μM of FdsDABG and were reduced with 10 mM sodium formate. The largest signal is seen with FdsDABG prepared in 50 mM HEPES buffer pH 7.5 with 10 mM KNO_3 in (green). The following samples have been prepared await EXAFS analysis by our collaborator Graham George (University of Saskatchewan). The EXAFS experiments will be performed either in CLS (Canadian Light Source) or in SSRL (Stanford Synchrotron Radiation Lightsource) centers.
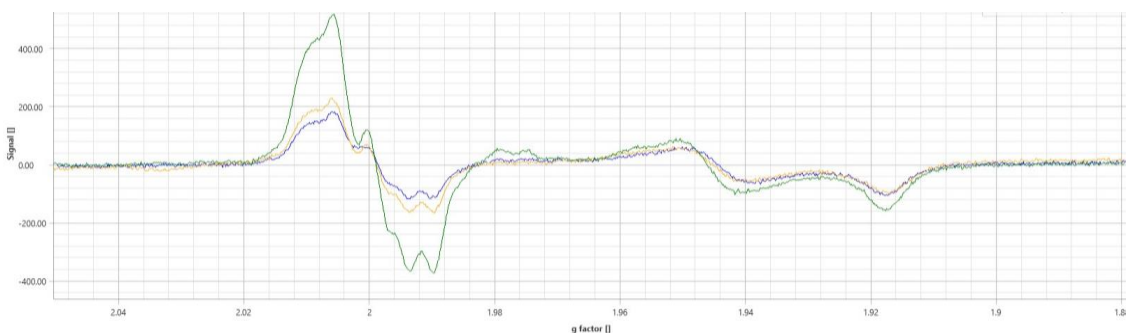
Figure 30. EPR spectra of FdsDABG in pH-varied buffers. EPR spectra of 14 μM FdsDABG in 50 mM MES buffer pH 6.5 (yellow), in 50 mM HEPES buffer pH 7.5 (green) and in 50 mM TRIS buffer pH 9.0 (blue). All samples contained 40 M of FdsDABG, 10 mM sodium formate and 10 mM KNO_3. EPR spectra were recorded via Bruker Magnettech ESR500 spectrometer Advanced Research Systems (ARS) set at 80 K, modulation amplitude of 0.3 mT and a power of 4 mW.

3.4.1. Discussion

For the purpose of achieving the greatest extent of Mo(V) accumulation in FdsDABG for EXAFS studies, (to obtain detailed structural information about the immediate molybdenum coordination sphere, it is crucial to have a very strong signal for the Mo (V) signal. We find maximal accumulation of the Mo(V) EPR signal to be at pH 7.5, and hence the sample of FdsDABG being reduced with sodium formate was made with buffer with that pH.

CHAPTER 4

O$_2$ inactivation of FdsDABG is mediated by superoxide

Native FdsDABG is notably less sensitive to inactivation by O$_2$ compared to other formate dehydrogenases, but it does slowly lose activity in air in the absence of stabilizing compounds such as KNO$_3$ or sodium azide. Unfortunately, both these compounds are inhibitors of the enzyme, and therefore unsuitable for use in kinetic studies of the enzyme. FdsDABG with no KNO$_3$ loses approximately 80% of its activity in a 24-hour aerobic incubation at 4 °C. In order to determine the nature of this inactivation, enzyme was incubated with superoxide dismutase, catalase or a combination of the two. Figure 31 shows that superoxide dismutase significantly protects FdsDABG from inactivation during air exposure over 24 hours, presumably scavenging the reactive O$_2$•$^-$. Catalase alone could not protect the enzyme from inactivation, but it does augment protection of FdsDABG by superoxide dismutase by scavenging peroxide generated by the dismutase. It is known that many flavoproteins are prone to photoreduction, even under ambient light, and in air will reoxidize to form both superoxide and peroxide. To investigate this as a possible source of superoxide in the inactivation process, a sample was left in the dark for 24 hours to compare to an identical sample left in the presence of light. The sample in the absence of light maintained only ~5% more activity relative to the sample in the presence of light, indicating that light is not the main factor causing loss in activity under aerobic conditions.
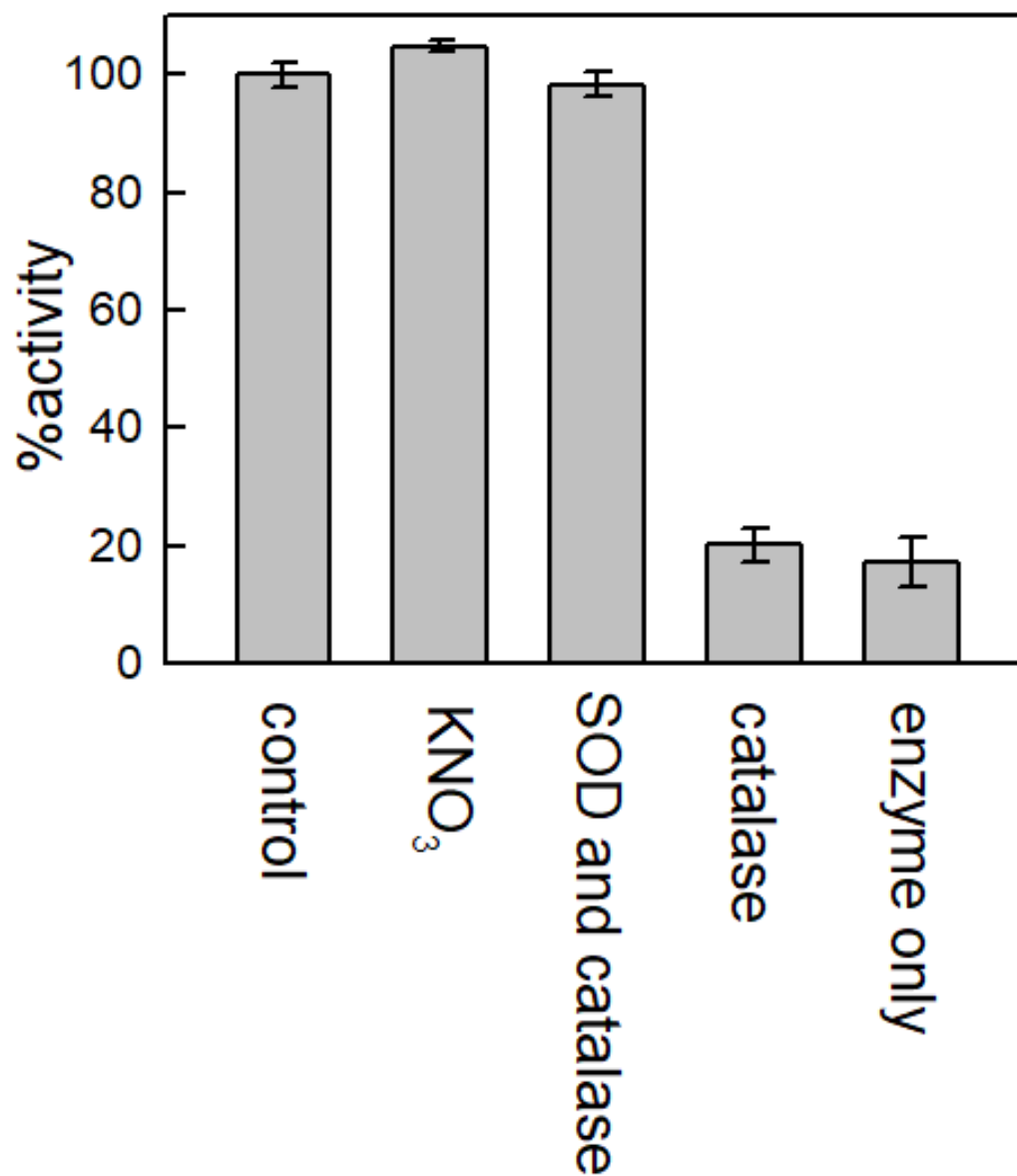
Figure 31. Activity percentage of air-exposed FdsDABG Inactivation of FdsDABG due to air exposure overnight. All samples were incubated in 50 mM HEPES pH 7.2 at 4 ℃. The percentage of active enzyme after 24-hour air exposure from left to right, in the presence of: 10 mM KNO3 (control), 100 units of superoxide dismutase and 4 nM catalase, 4 nM catalase, enzyme only and enzyme only in the absence of light. The activity was measured by utilizing formate/NAD$^+$ assay.

To confirm that superoxide dismutase is indeed able to protect the enzyme from air-inactivation, samples treated in several ways were exposed to air for 24 hours, made anaerobic and reduced by sodium formate, the amount of active enzyme being determined by the magnitude of the absorbance change. Figure 32 depicts the oxidized and reduced spectra for three different samples: enzyme in the presence of the stabilizer KNO_3, with superoxide dismutase and a control with no stabilizing compound. For convenient analysis of the data, the oxidized-minus-reduced difference spectra for each sample were obtained. It is clear from Figure 32B that the difference spectra for the sample containing superoxide dismutase was identical to the that containing KNO_3. This clearly demonstrates that superoxide dismutase is just as effective in stabilizing FdsDABG as KNO_3. We note that the control sample containing neither dismutase or KNO_3 had lost all activity (Figure 32B, blue difference spectrum).
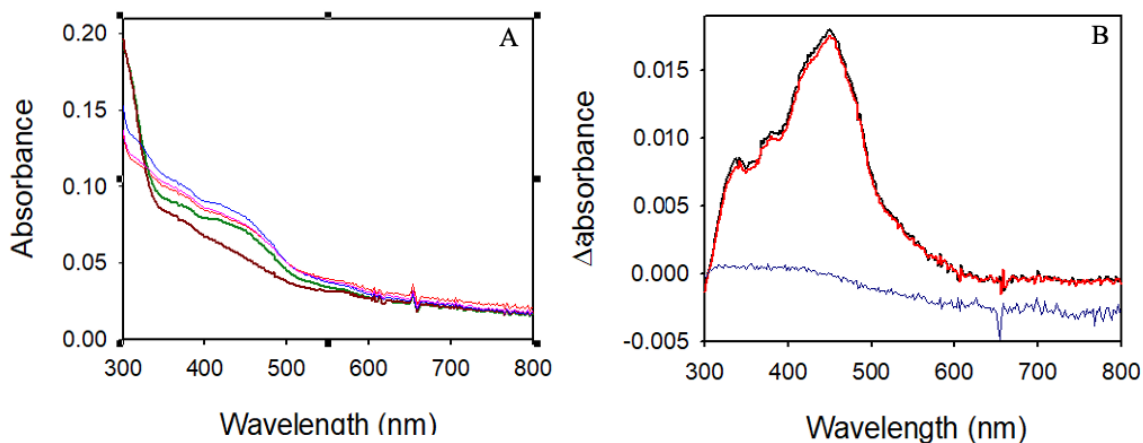
Figure 32. UV/Vis spectra of anaerobic reduced FdsDABG. A. The UV/Vis spectra of anaerobic reduction of FdsDABG samples by sodium formate after aerobic incubation overnight at 4 ℃. Sample in the presence of 100 units of superoxide dismutase (blue: oxidized, black: reduced), 10 mM KNO_3 (oxidized: dark green, reduced: dark red), enzyme only (oxidized: magenta, reduced: red). B. difference spectra of the spectra in A. Oxidized minus reduced for FdsDABG in the presence of superoxide dismutase (black), KNO_3 (red) and enzyme only (blue). All spectra were acquired in 50 mM HEPES pH 7.2 containing 4 nM catalase at 20 °C.

An external source for superoxide production was utilized to study how susceptible FdsDABG is against superoxide. The external source is xanthine oxidase producing superoxide in the course of turnover with xanthine in the presence of oxygen. FdsDABG was incubated with catalytic amounts of xanthine oxidase in the presence of xanthine under aerobic condition. The activity of the enzyme was assessed at various time points throughout the 60 minutes by utilizing the formate/NAD$^+$ mix. The graph in Figure 33 demonstrates that the loss of activity is very rapid in the presence of xanthine oxidase. On the other hand, 100 units of superoxide dismutase protected FdsDABG, resulting 100 % activity. KNO_3 was a bit less effective and resulted in 80% activity remaining. The black trace was a control to compare the rate of inactivation of enzyme with no protection and no external source of superoxide. The concentration of xanthine oxidase seemed to not

have a significant impact since the sample with 10 times less xanthine oxidase only maintained some activity around 7 minutes longer.
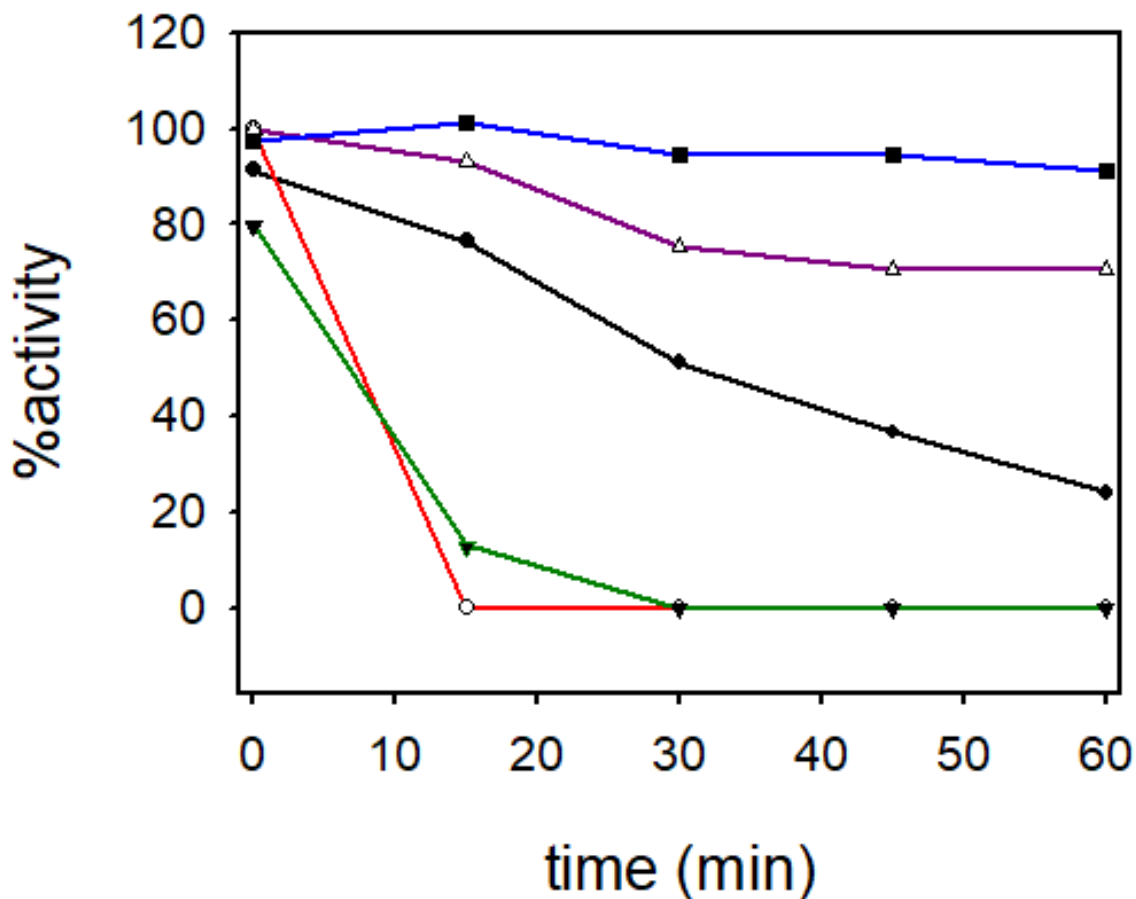

Figure 33. Inactivation of FdsDABG by superoxide exposure. Inactivation of FdsDABG by superoxide. Percentage of activity versus time of aerobic incubation with 0.1 μM xanthine oxidase and 100 units of superoxide dismutase (blue trace) , 0.1 μM xanthine oxidase and 10 mM KNO_3 (purple trace), enzyme only with no xanthine oxidase (black trace), 0.01 μM xanthine oxidase (green trace) and 0.1 μM xanthine oxidase (red trace). All samples were incubated in 50 mM HEPES pH 7.2 containing 4 nM catalase and 330 μM of xanthine. The activity was measured based on the formate/NAD^+ assay explained in the methods section.

To examine how superoxide might be generated by FdsDABG, the following experiment was performed, taking advantage of the known ability of superoxide to reduce cytochrome *c,* which can be conveniently monitored by UV/Visible spectroscopy at 550 nm. Cytochrome *c* was thus added to an aerobic sample of FdsDABG, and sodium formate

then introduced to reduce the enzyme. Catalase was included to prevent reoxidation of any reduced cytochrome c that accumulated by peroxide. The time courses thus obtained are shown in Figure 34A for samples in the absence and presence of superoxide dismutase. While the extent of cytochrome c reduction in the absence or presence of superoxide dismutase is the same using both formate and NADH to reduce the active and inactive enzyme respectively, it is clear that dismutase significantly reduces the rate of cytochrome c reduction. In the presence of superoxide dismutase, we attribute reduction of cytochrome c to direct intermolecular electron transfer between FdsDABG and cytochrome c. A control was performed with inactivated FdsDABG using NADH to reduce the enzyme (via its FMN site), as shown in Figure 34B, the results indicate that FdsDABG generates superoxide in a manner that is not strictly dependent on a functional molybdenum center, most likely the FMN site itself.
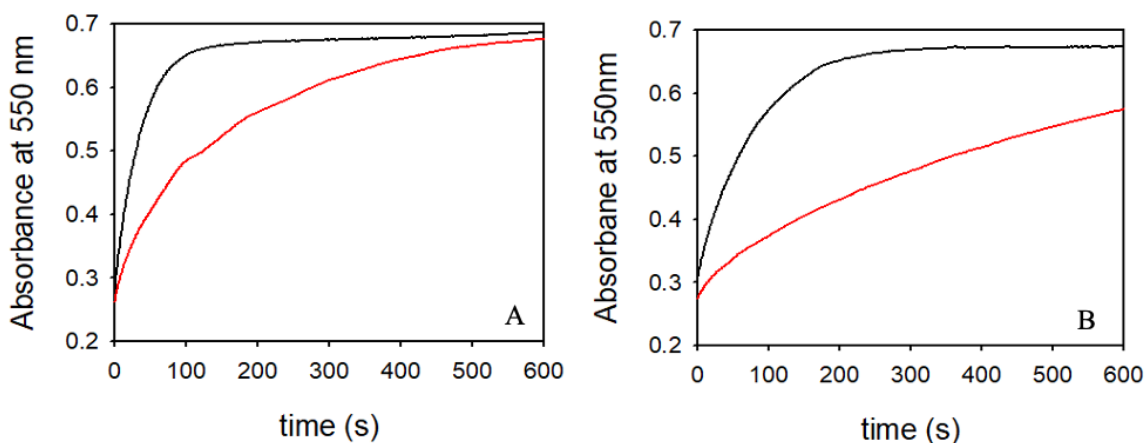

Figure 34. Cytochrome c reduction by FdsDABG. Cytochrome c reduction by FdsDABG in the absence (black) and presence of superoxide dismutase. A. reduction of cytochrome c by active FdsDABG reduced with 2 mM sodium formate. B. reduction of cytochrome c by inactive FdsDABG reduced with 1 mM NADH. All reactions were performed in 50 mM HEPES pH 7.7 at 20°C.

113

To examine the direct electron transfer between FdsDABG and cytochrome c, the reaction of reduced FdsDABG with oxidized cytochrome c was investigated by stopped-flow kinetics. This was done under anaerobic conditions, including the use of a glucose oxidase/glucose to scrub residual O_2, superoxide dismutase to avoid any production of superoxide and catalase to prevent enzyme damage by peroxide. FdsDABG was made anaerobic and transferred in the anaerobic chamber, then treated with excess sodium formate to reduce it; excess formate was removed chromatographically prior to the transfer to the stopped-flow instrument. Figure 35 depicts the absorption change that occurs on mixing FdsDABG thus reduced with cytochrome c, and it is clear that cytochrome c is effectively reduced by direct electron transfer from reduced FdsDABG, as reflected in the large absorbance increase at 550 nm, and on the same timescale as cytochrome c reduction in the presence of superoxide dismutase in the experiments shown in Figure 34.
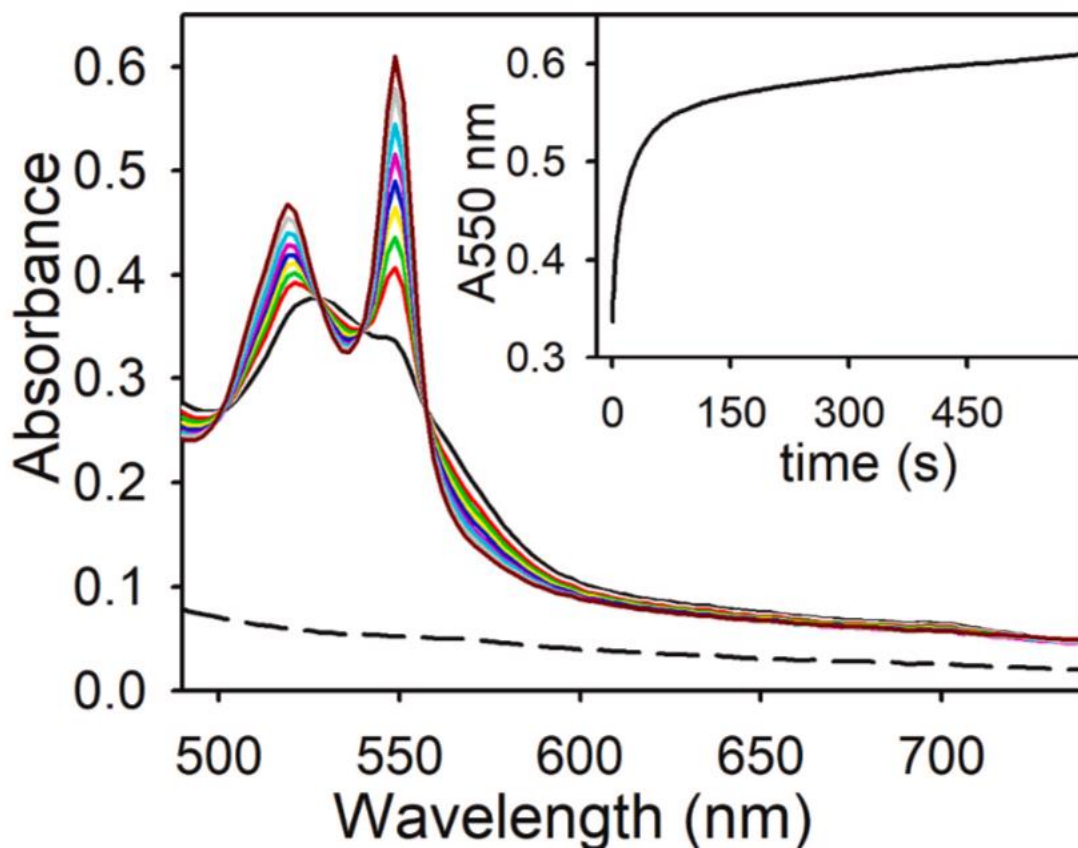
Figure 35. Detection of intermolecular electron transfer by stopped-flow spectrophotometry. Anerobic reduction of 25 μM of cytochrome c with 5 μM pre-reduced FdsDABG. FdsDABG was pre-reduced with excess amount of sodium formate which was removed prior to the rapid reaction kinetics experiment in the stopped-flow spectrophotometer. The spectrum of the pre-reduced FdsDABG is shown in black dashes as reference. The inset shows the time course at 550 nm extracted from the PDA. The experiment was conducted in 50 mM HEPES buffer pH 7.2 with 30 units of superoxide dismutase, 8 nM catalase, 40 nM glucose oxidase, and 10 mM glucose at 20 ℃.

To determine whether superoxide reduces FdsDABG in the course of inactivation, FdsDABG was incubated with xanthine oxidase and xanthine, a known superoxide-generating system, under aerobic conditions. To keep FdsDABG active in the presence of the superoxide generated, KNO_3 was included in the reaction mix. The reaction was monitored spectroscopically, and as shown in Figure 36 we find that FdsDABG is indeed at least partially reduced by superoxide, as reflected in the absorbance decrease over time. The spectral change reflects the reduction of iron-sulfur clusters in the protein.
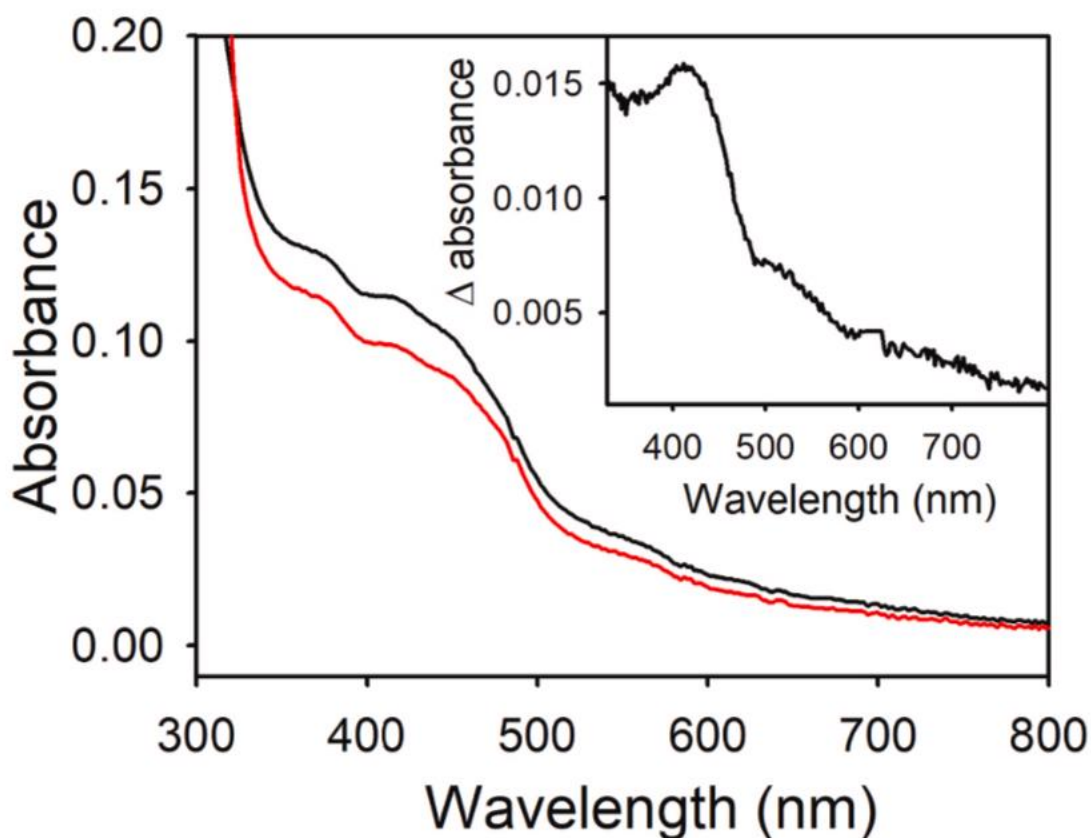
Figure 36. Reduction of FdsDABG by superoxide. 2.3 μM of FdsDABG was incubated with 0.01 μM xanthine oxidase, 330 μM xanthine and 4 nM catalase in the presence of 10 mM KNO_3. The enzymes were incubated for 60 minutes. The UV/Vis spectrum of oxidized FdsDABG is shown in black and the reduced spectrum after 60 minutes is shown in red. The inset depicts the difference spectrum oxidized minus reduced. The experiment was done in 50 mM HEPES buffer pH 7.2 with 10 mM KNO_3 at 20°C.

EXAFS work with xanthine oxidase (R. Hille et al. 1989) and CODH (Kreß et al. 2014) has demonstrated that the catalytically essential Mo=S group can be replaced with an oxygen atom in the course of inactivation, yielding so-called desulfo forms of these enzymes. FdsDABG from *Rhodobactor capsulatus* loses the sulfido ligand during inactivation as well. The enzyme is more vulnerable when it is reduced, likely because protonation of the sulfido ligand to Mo(IV)-SH makes it more easily displaced by hydroxide from solvent, particularly at higher pH. FdsDABG also loses activity faster at higher pH. One possible mechanism for the loss of the sulfido ligand in the presence of superoxide is that the Mo=S ligand gets oxidized and SO_2 is produced as a result, which gets ultimately hydrated to sulfite. In order to examine this, FdsDABG was inactivated over 24 hours by exposure to air, then assayed for sulfite utilizing human sulfite oxidase (hSO). hSO possesses a b-type heme in addition to its molybdenum center where the sulfite is oxidized. This becomes reduced in reaction of the enzyme with sulfite after electrons transfer out of the now-reduced molybdenum center, giving rise to a large spectral change. It was necessary to first make the FdsDABG sample anaerobic after air-inactivation since hsO is reoxidized relatively quickly by O_2. As shown in Figure 37, we find that sulfite is indeed generated in the course of air-inactivation of FdsDABG. The analysis of the UV/Vis spectra indicate that 2.2 equivalents of reduced cytochrome *c* is generated per inactivate enzyme which results in 1.1 equivalents of sulfite.
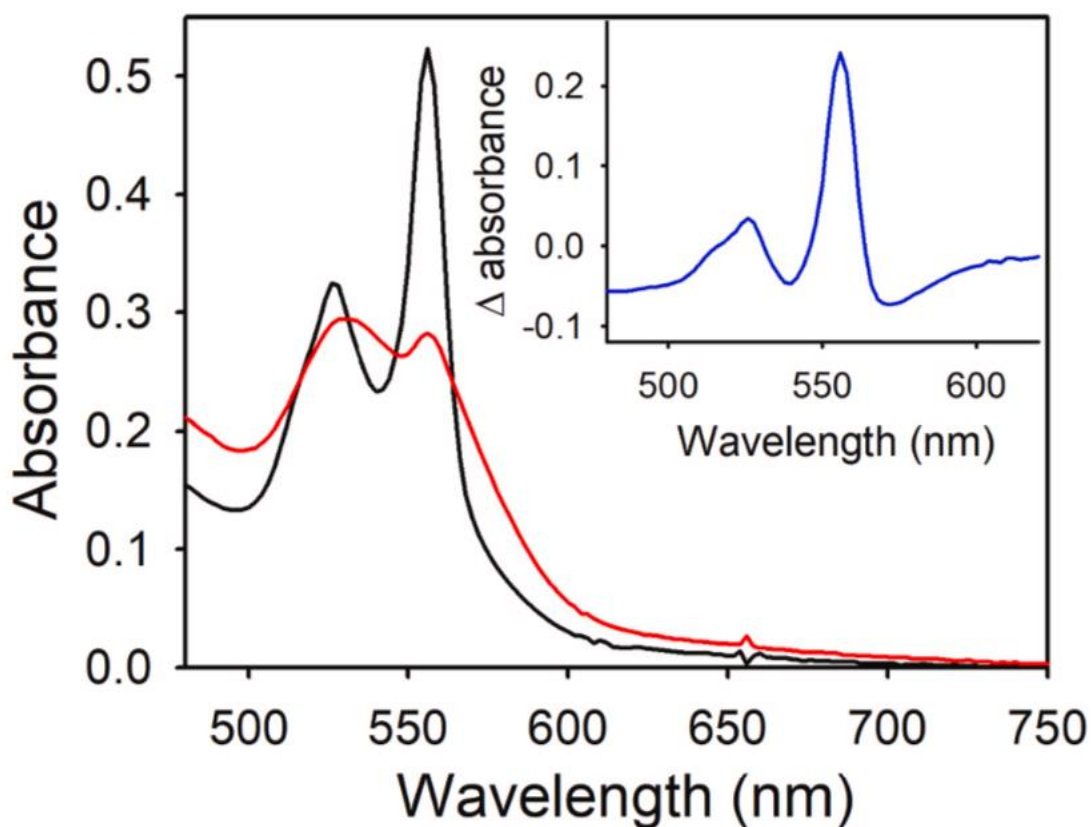
Figure 37. Sulfite generation by inactivated FdsDABG. FdsDABG was inactivated with sodium formate for ~ 24 hours aerobically and the flowthrough containing the result of the inactivation without the enzyme was transferred to the anaerobic chamber and was incubated with hSO (black spectrum). The spectrum in red represents hSO with buffer as the control, adjusted to the same concentration used for the incubation with FdsDABG. All reactions were done in 50 mM HEPES buffer pH 7.2.

4.1. Discussion

KNO_3 is a mixed competitive non-competitive inhibitor of FdsDABG, but protects the enzyme from inactivation when exposed to air, presumably by binding at or near the molybdenum center. It is thus of interest to find alternate ways to protect the enzyme from air-inactivation that do not interfere with activity. It is also of intrinsic interest to understand the specific mechanism of air-inactivation of the enzyme. We have shown here that superoxide dismutase is an extremely effective alternative to protection of FdsDABG

against air-inactivation, and that the superoxide-mediated loss of enzyme activity results in oxidation of the Mo=S sulfur to sulfite. Superoxide is generated by FdsDABG, but this is not exclusively due to the molybdenum center. Many simple flavoproteins generate superoxide upon air-reoxidation, and the FMN is the likeliest site of the additional superoxide generation seen with FdsDABG. It would next be interesting to see if the FdsBG subcomplex, which lacks the molybdenum active, but is in possession of the FMN also generates superoxide.

CHAPTER 5

Electrochemical studies of FdsDABG

We have established a collaboration with Dr. Bernhardt, Department of Chemistry, University of Queensland, Australia, an expert in electrochemical applications to biological systems, the reduction potentials of FdsDABG. An update of this work is included below. In optical spectroelectrochemical titrations (shown in Figure 38) the flavin mononucleotide (FMN) is seen to go through a two-step reduction with the one-electron reduced flavin semiquinone as an intermediate in formation of the two-electron reduced flavin hydroquinones, with half- potentials for the quinone-semiquinone and semiquinone/hydroquinone couples of -270 and -390 mV, respectively. It appears that the iron sulfurs are not visible due to difference in their extinction coefficient.
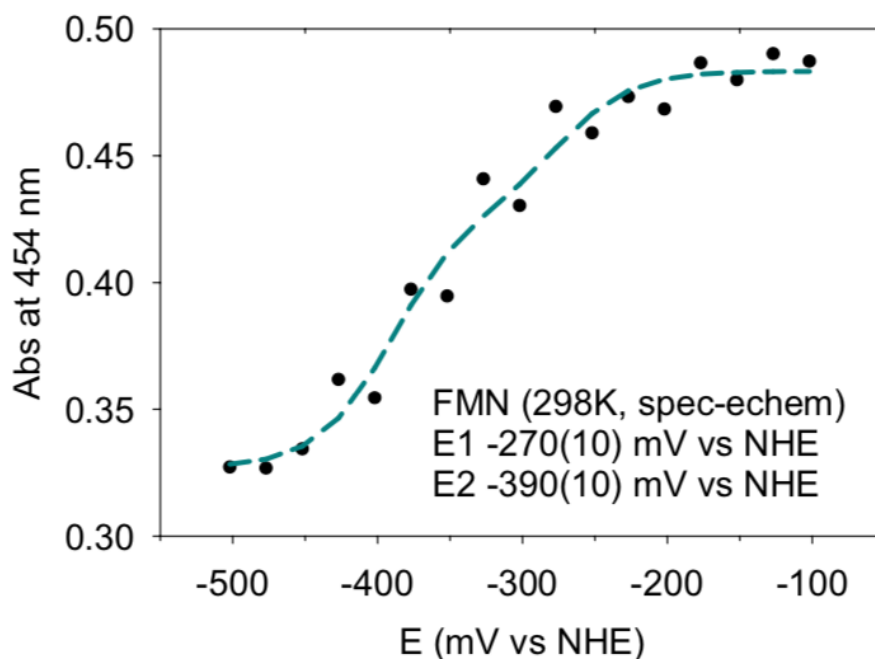

Figure 38. Two-step reduction of FMN in FdsDABG. The experiment was conducted at 25 ℃. The two midpoint potentials are at -270 and -390 mV. The iron sulfurs are not visible due to difference in their extinction coefficient.

120

Figure 39 illustrates the data acquired from EPR redox titration and the obtained potentials are shown. The data result in a redox potential for the molybdenum cofactor and four of the iron-sulfur clusters. The [2Fe-2S] in the G subunit has the highest midpoint potential (panel B in Figure 39). Full reduction of molybdenum to Mo (IV) is a bit challenging.
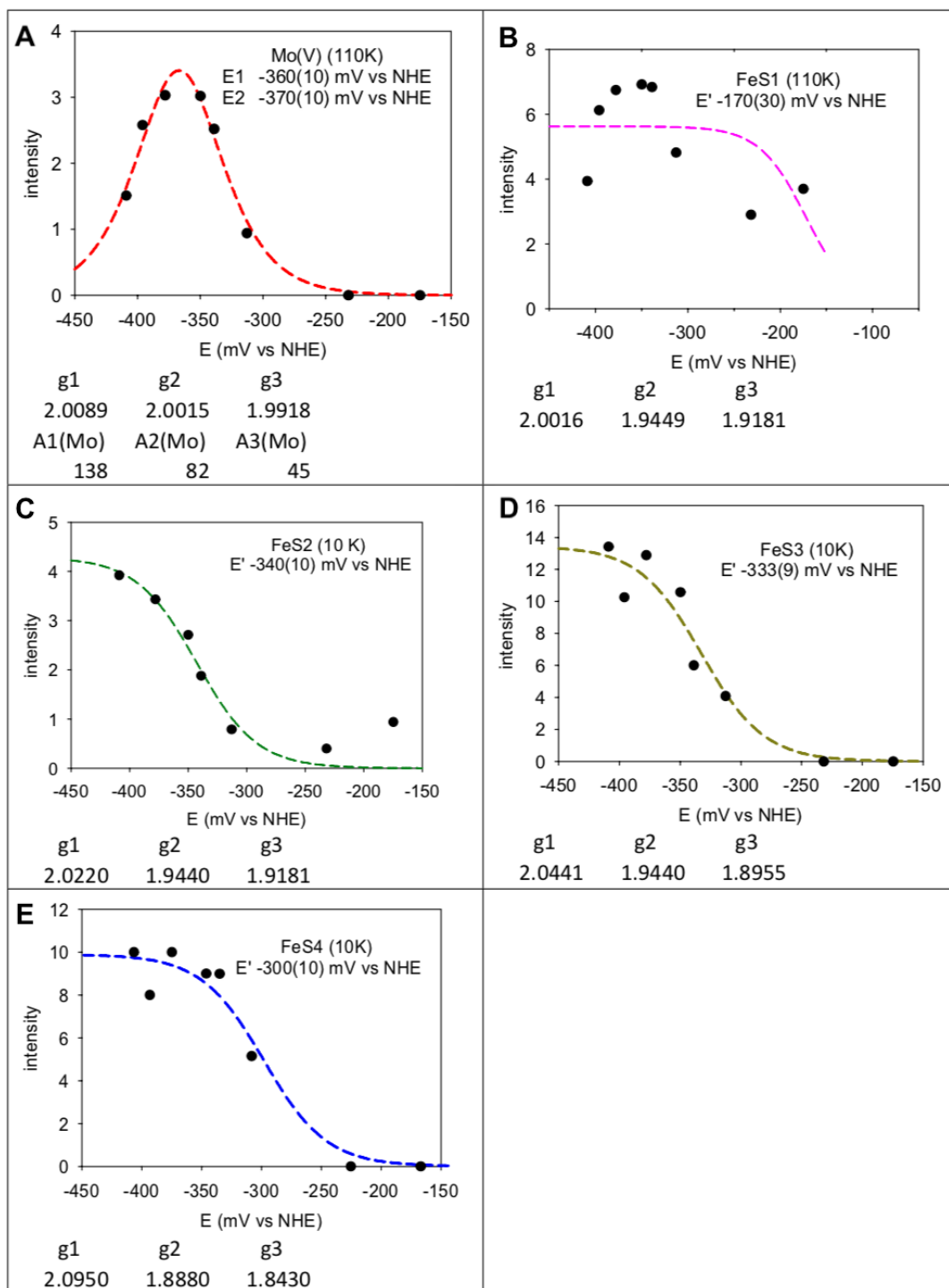
Figure 39. Redox potentials for molybdenum and the iron sulfur clusters. Redox potentials for molybdenum (A), and the iron sulfur clusters in panel B through E. The highest potential belongs to [2Fe-2S] in the G subunit of FdsDABG.

The electrochemical interconversion of formate and CO_2 by FdsDABG has also been investigated via cyclic voltammetry (CV). As shown in Figure 40, this work has demonstrated both catalytic anodic (formate oxidation) and catalytic cathodic (CO_2 reduction) currents in the same cyclic voltammogram, with formate and bicarbonate both present in the bulk solution. Methyl viologen serves as a mediator between enzyme and electrode in this experiment since its reduction potential is close to that of the $HCOO^-/CO_2$ couple (-410 mV, pH 7). Moreover, methyl viologen is not biased towards either direction of the reactions. This study gives a midpoint potential of -420 mV for the catalytic interconversion of formate and CO_2, in good agreement with the thermodynamic potential of the $HCOO^-/CO_2$ couple at pH 7. Studies on the formate concentration dependence of the catalytic voltammetry have also been performed, using methyl viologen, methylene blue or phenazinium as mediators, with K_M values of 281, 416 and 898 μM, respectively, obtained. The variation in K_M is yet to be explored since the substrate binding or enzyme turn overs should be identical for all three and they all therefore should produce the same value. In normal steady-state assays in the forward direction with NAD^+ as oxidizing substrate, $K_M^{formate}$ is 310 μM (Niks et al. 2016).
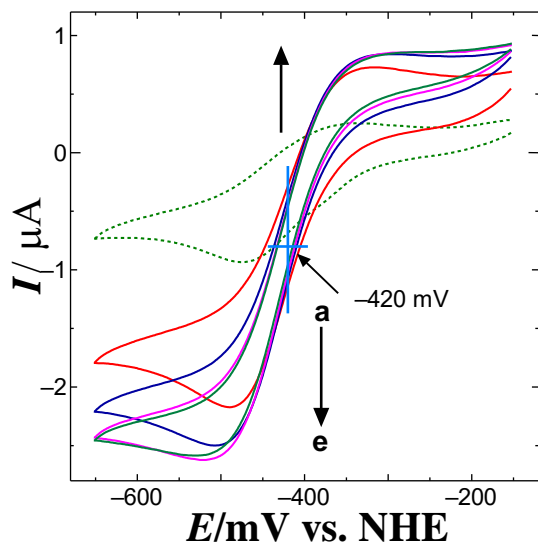
Figure 40. Interconversion of formate and CO_2 via cyclic voltammetry. Cyclic voltammetry with 50 μM MV^{2+} as the mediator was performed.. The concentrations for formate and HCO_3^- were as follows: (a) 0 (broken line), (b) 200 μM and 2 mM, (c) 400 μM and 4 mM (d) 800 μM and 8 mM and (e) 800 μM and 8 mM at a scan rate of 5 mV s^{-1} in 100 mM phosphate buffer solution (pH 7.0) and 25 $^\circ$C. The electrode used was GC/Chit+FdsDABG+GTA.

The pH dependence in both formate oxidation and CO_2 reduction directions have also been examined, with the results shown in Figure 41. Catalysis in both directions result in a bell-shaped curve with pH 7.5 being the optimum pH for formate oxidation and pH 6.5 for CO_2 reduction.
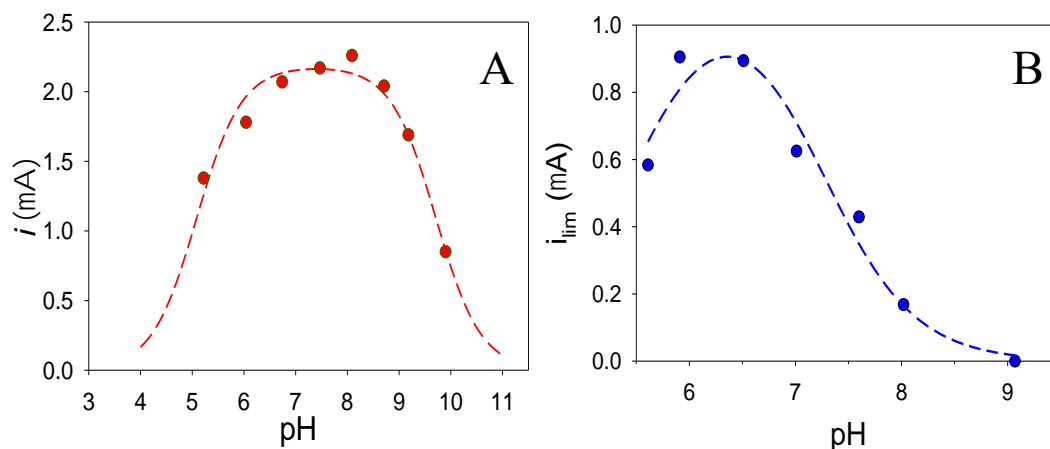
Figure 41. pH dependence cyclic voltammetry: A. Formate oxidation, 20 µM methylene blue and 2.4 mM sodium formate. B.CO2 reduction, 20 µM methyl viologen and 24 mM $NaHCO_3$. For both experiments the electrode was GC/FdsDABG and scan rate of was 10 mV s^{-1} in 100 mM mixed buffer solution.

5.1. Discussion

Determination of the reduction potentials of any oxidoreductase enzyme is an integral part of its characterization, particularly in the case of enzymes possessing multiple redox-active centers, and specifically when electron transfer from one site to another is an integral aspect of catalysis as is the case with FdsDABG. The electrochemical work with FdsDABG described here is an important first step in elucidating and confirming information on the path the electrons take while the hydride transfer is in action. More importantly, these studies, specifically spectroelectrochemistry will allow us to observe any transient species or radicals by manually applying potentials and looking at the enzyme's UV/Vis spectra. Moreover, the cyclic voltammetry analysis demonstrated that the conversion between formate and CO_2 is reversable, consistent with a simple hydride transfer mechanism which enables the enzyme to switch directions according to the poised

system potential, *in vitro* or *in vivo*. In all, these results suggest that formate dehydrogenase (or synthetic catalysts that function in a way that mimics enzyme action) may provide an efficient solution the remediation of atmospheric CO_2 and global warming.

CHAPTER 6

Crystallographic studies of FdsBG

Repeated efforts to crystallize FdsDABG have been unsuccessful, but we have been able to obtain crystals of the FdsBG fragment, containing the FMN as well as individual [2Fe-2S] and [4Fe-4S] clusters. As discussed in Chapter 2, protein was expressed with a 6xHis-linker-6xHis tag on the N-terminal of the G subunit of FdsBG, with 4 L of culture yielding 40 gram of cells and 83 mg of pure FdsBG complex (Young et al. 2020).

The structure of FdsBG complex with the 6xHis-linker-6xHis tag was determined by X-ray crystallography to 2.3 Å, with the structure shown in Figure 42. The rotation axis (in red) passes through the N-terminal domains of the two FdsB subunits, which overall fold is very similar to thioredoxin. The dimensions of the crystal are 82 Å x 64 Å x 62 Å with two heterodimers related by a pseudo 2-fold symmetry rotation. A [4Fe-4S] is clearly identified in the B subunit and a [2Fe-2S] in the G subunit, along with the FMN, also in FdsB. The published structure of *A. aeolicus* NuoEF from the organism's NADH dehydrogenase complex was used as initial search model, due to the homologies of its subunits to those of FdsBG, NuoE is homologous to FdsG and NuoF to FdsB. This is illustrated in Figure 43, panels A and B (Young et al. 2020).
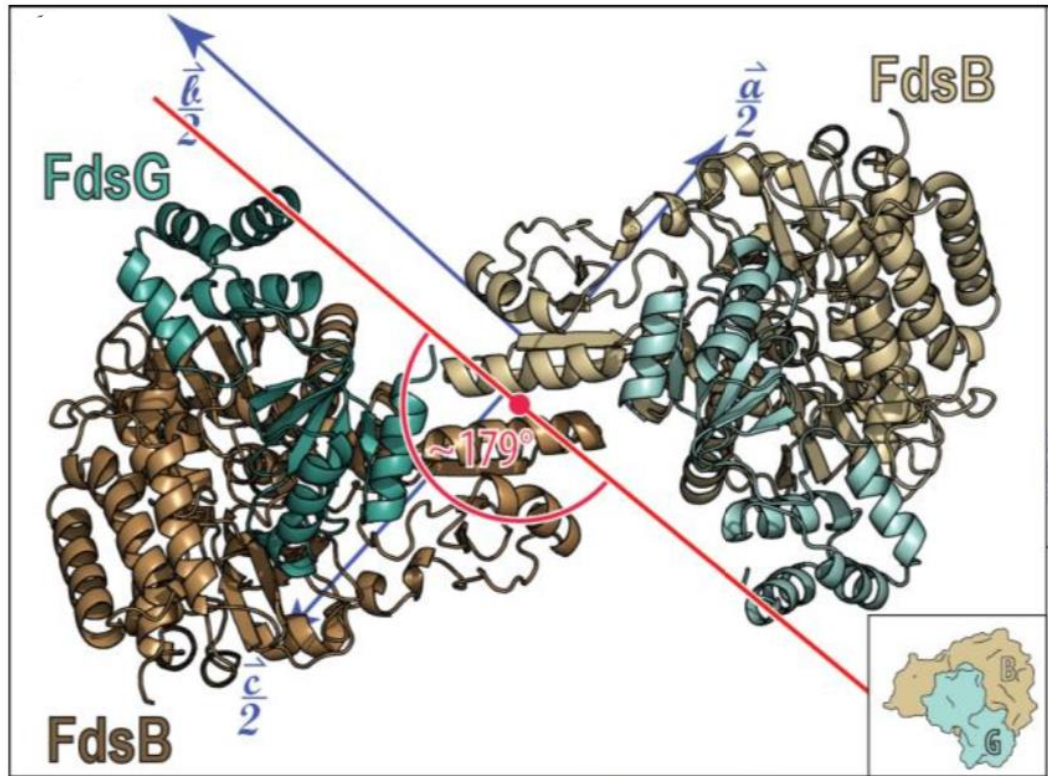
Figure 42. The arrangement of dimer FdsBG complex. The orientation of the two FdsBG complexes of the asymmetric unit and the corresponding electron density maps is demonstrated. The arrangement of the two FdsBG complexes of the asymmetric unit in the unit cell from the viewpoint of the ~179° rotation axis (red). All crystallographic axes are drawn in blue. The b axis is the two-fold crystallographic axis. The angle between the rotation axis and b axis is approximately 92° (Young et al. 2020).

Figure 43. Structural comparison of FdsBG and NuoEF complexes. The differences in A. the Rossmann-like domain and the location of [4Fe-4S], B. Ubiquitin and four helical bundle domains and the [4Fe-4S]. The Rossmann-like domain (white), ubiquitin (green), the four-helical bundle domains of FdsB (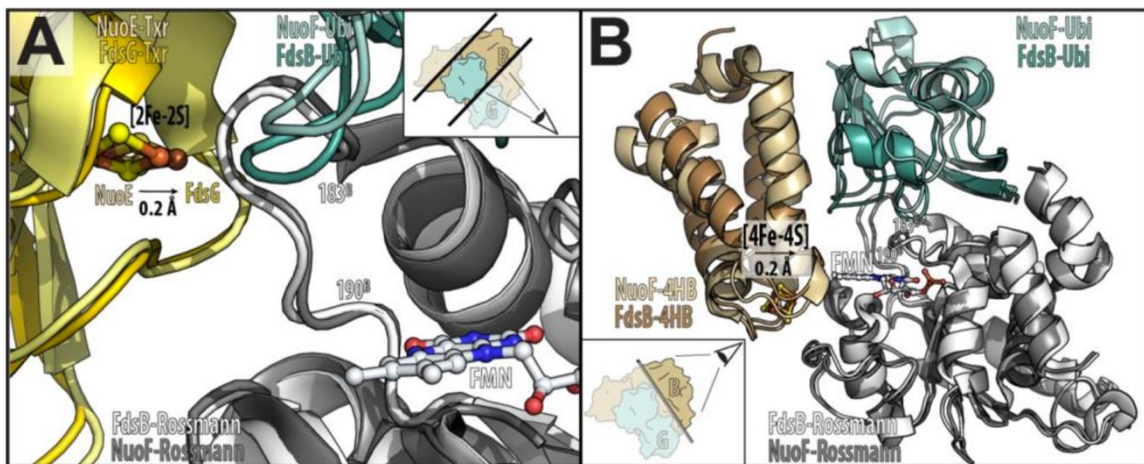brown), and the C-terminal domain of FdsG (gold). The corresponding domains in NuoF and NuoE are displayed in gray, light green, beige and pale yellow respectively (Young et al. 2020).

In the structure of FdsBG, the FMN is found in a solvent accessible cavity where it is held in place by a web of interactions. In addition to FMN, the cavity can accommodate NADH/NAD$^+$. The two iron-sulfur cluster of FdsBG are within 12 Å of the isoalloxazine ring of FMN. The C8-methyl of the dimethylbenzene faces towards the [4Fe-4S] (5.9 Å) and the N5- containing edge looks on to [2Fe-2S] (12.1 Å) whereas the ribityl phosphate tail distances itself from both clusters as demonstrated in Figure 44.
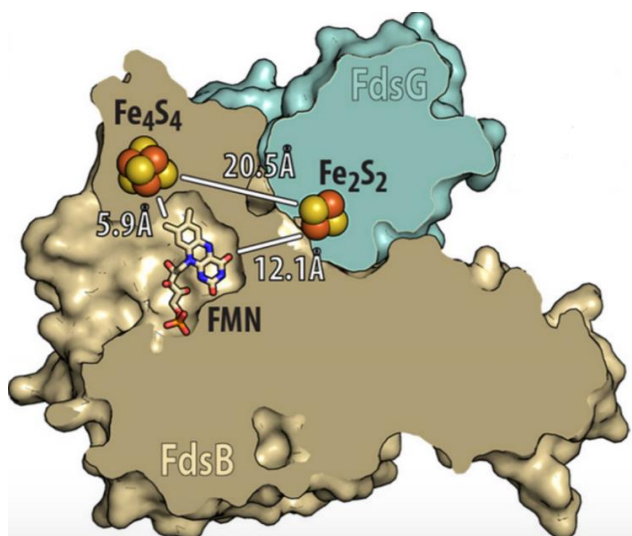
Figure 44. Overall orientation of iron-sulfur clusters in FdsBG. The C8-methyl group of the dimethylbenzene is oriented towards the [4Fe-4S] cluster at 5.9 Å, while the N5-containing edge is positioned in proximity to the [2Fe-2S] cluster, which is 12.1 Å away. In contrast, the ribityl phosphate tail moves away from both clusters.(Young et al. 2020).

In order to ascertain how NADH binds to FdsBG, preformed crystals were soaked with 10 mM NADH for approximately two hours prior to being flash frozen in liquid nitrogen. X-ray diffraction data to a resolution of 2 Å were remotely collected at ALS. The structure was solved by molecular replacement using the FdsBG as initial model. Figure 45 shows some of the crystals that were used for this experiment (Young et al. 2020). The overall structures of FdsBG in the presence and absence of NADH were virtually identical. The electron density map (Figure 46A) shows that the adenosine diphosphate moiety of NADH adjacent to the FMN, with a salt bridge between the β phosphate of NADH and Lys-292 of FdsB and two hydrogen bonds between NADH and O2′ and O4′ of the ribityl moiety of FMN. Only weak electron density is visible for nicotinamide portion of NADH.

However, the positioning of the ADP moiety of NADH clearly indicates that the nicotinamide ring is directed toward the *re*-face of the isoalloxazine ring of FMN.
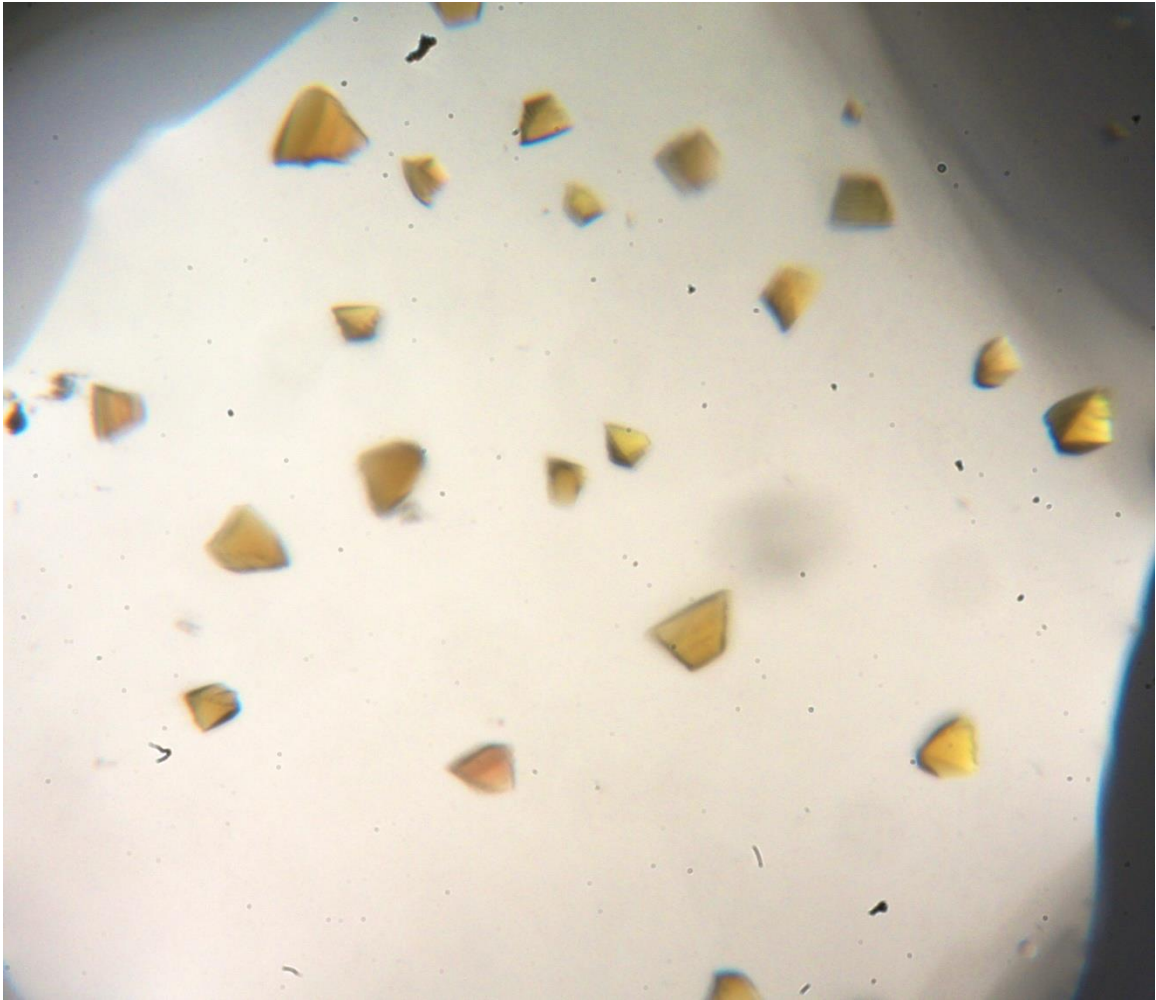
Figure 45. FdsBG crystals used for NADH soaking. The crystals were obtained from 100 mM HEPES buffer pH 7.5, 1.3 M ammonium sulfate and 5.2 % [v/v] isopropanol. The crystals once formed were incubated in stabilization solution consisting of the reservoir solution without the isopropanol and increasing levels of glycerol to a final of 2.4 % [v/v]. The stabilized crystals were soak with 10 mM NADH for 45 minutes before mounting and flash freezing in liquid nitrogen.
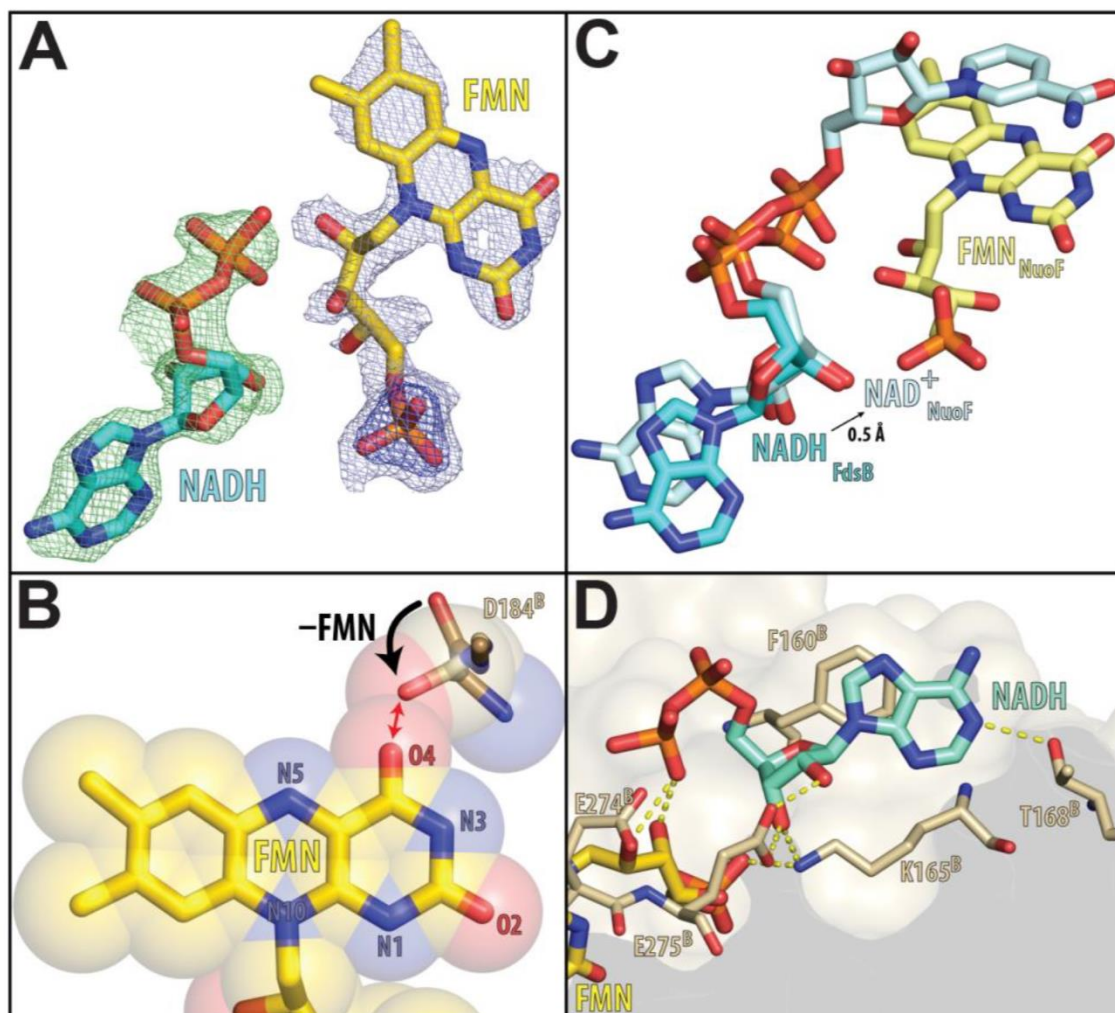
Figure 46. NADH binding site. The Electron difference maps resulted from the unbiased (F_o-F_c)- and ($2F_o$-F_c) for FdsBG crystals soaked with NADH. FMN and the adenosine diphosphate of NADH are displayed in gold and cyan ball-and-stick. B. Steric overlap between the D184-E185 peptide bond in FdsB with FMN in crystals of FdsBG complex soaked with NADH. C. The position of NADH and NAD$^+$ relative to FMN in the FdsBG versus NuoEF complexes respectively (bound form). D. Adenosine diphosphate of NADH (blue) bound to FMN (gold). The binding site is displayed in beige (Young et al. 2020).

6.1. Discussion

An atomic-resolution structure of an enzyme reveals a great amount of information about its function. One of the interesting points arising from determination of the X-ray crystal structure of FdsBG learned in the present work was establishing the location and position of the cofactors, the FMN, [4Fe-4S] and [2Fe-2S], including their distances from

and orientations with respect to each other. In addition, it showed that while the adenosine diphosphate portion of NADH was better resolved in the electron density than the nicotinamide portion of the cofactor it nevertheless accesses the *re* face of the flavin rather than the *si*. We note that since publication of our X-ray crystal structure for the FdsBG fragment of FdsDABG the structure of the full structure of FdsDABG has been determined by cryoelectron microscopy has been reported (Radon et al. 2020) The structure of the FdsBG fragment within the FdsDABG complex is fully consistent with our crystallographic results.

Chapter 7

Expression and purification of FdhF from *Pectobacterium atrosepticum*

The FdhF component of the formate:hydrogen lyase complex of *P. atrosepticum*, like FdsDABG, has cysteine coordinated to the molybdenum rather than selenocysteine. It was of interest to compare and contrast the molybdenum centers of the two proteins, and to that end, PEQ80 construct encoding both FdhF and the FdhD sulfurase that inserts the catalytically essential Mo=S into the molybdenum coordination sphere were obtained and the N-terminal twin Strep tag on FdhF was replaced with a Strep-SUMO tag. This plasmid was transformed into CLK002 cells and expression of FdhF induced under anaerobic conditions with IPTG. From 4 L of culture (TGYEP medium) 18 grams of cells were harvested and lysed anaerobically, with a final yield was 30 mg of pure FdhF which according to the BV assay explained in Chapter 2 maintained 83 % of the activity present in the supernatant. Figure 47 shows the UV/Visible absorption spectra of oxidized enzyme thus obtained before and after reduction with 5 mM sodium formate; a total of 50 % reduction was observed.
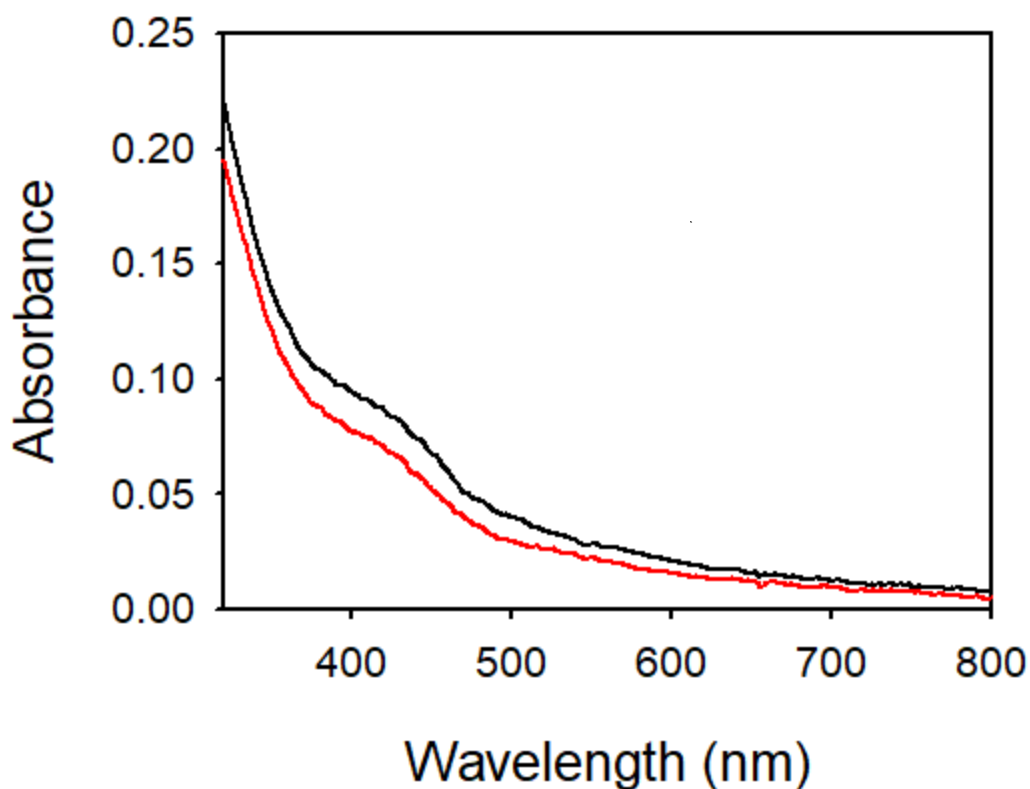
Figure 47. UV/Vis spectra of FdhF. 6 µM FdhF was reduced with 5 mM sodium formate. Oxidized spectrum (black) and reduced spectrum (red).

Figure 48 shows the EPR spectra of 126 µM oxidized FdhF (black) and of enzyme that was reduced with sodium formate (blue). Significantly, the Strep-SUMO tagged FdhF is the first recombinant form of the enzyme that after purification does not contain a large free radical signal that overlaps with the molybdenum signal. Figure 49 shows a comparison of the EPR spectra seen with FdhF and FdsDABG, where it can be seen that both exhibit a Mo(V) signal centered on g~2. It is to be noted that features in the EPR signal of FdsDABG in the 1.96-1.90 region are due to iron-sulfur clusters.

Figure 48. EPR spectra of FdhF. Oxidized 126 μM FdhF (black) and reduced with 5 mM sodium formate (blue). EPR spectra were recorded via Bruker Magnettech ESR500 spectrometer Advanced Research Systems (ARS) set at 80 K, modulation amplitude of 0.4 mT and a power of 2 mW
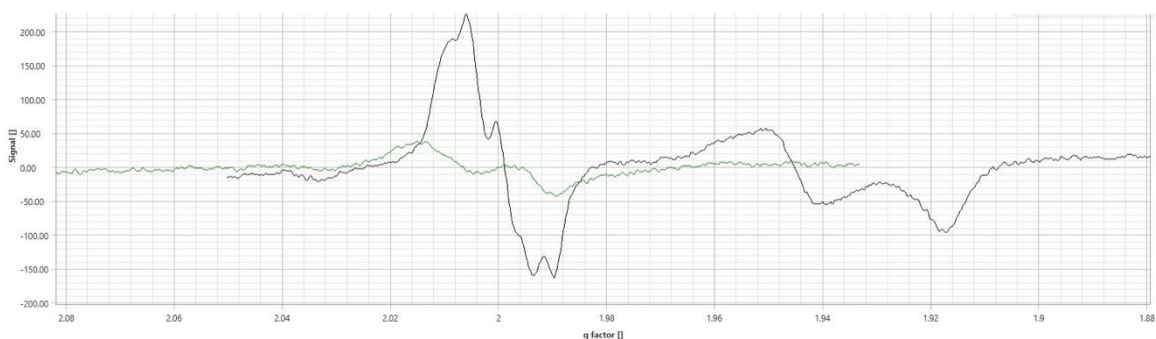
Figure 49. EPR spectra comparison of FdsDABG and FdhF. EPR spectra of 14 μM FdsDABG (black) and 126 μM FdhF (green) are depicted. Both enzymes were in 50 mM MES buffer pH 6.5. The Fd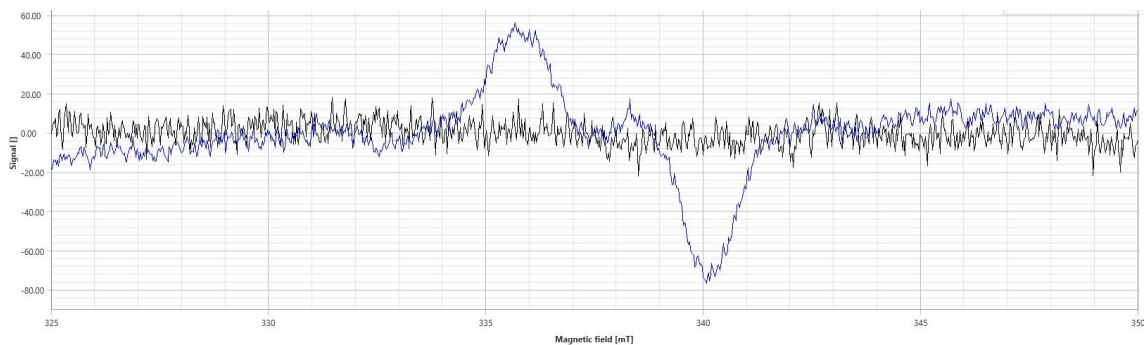sDABG sample contained 10 mM KNO_3. EPR spectra were recorded via Bruker Magnettech ESR500 spectrometer Advanced Research Systems (ARS) set at 80 K, for FdhF: modulation amplitude of 0.4 mT and a power of 2 mW and for FdsDABG: modulation amplitude of 0.3 mT and a power of 4 mW.

7.1. Discussion

The *P. atrosepticum* FdhF is in principle a stripped-down version of FdsDABG in that it possesses only a single [4Fe-4S] cluster in addition to its cysteine-coordinated molybdenum center. This removes the complexity of the six other iron-sulfur clusters and FMN which are present in FdsDABG. These two systems' molybdenum centers are virtually identical, particularly with regard to the cysteine coordination to the molybdenum. Studying the structure and function of FdhF will allow us to compare and contrast its behavior with that of FdsDABG and furthermore, will allow us to identify commonalities

and ascertain the extent to which the things learned about FdsDABG are generally applicable not only to other molybdenum-containing formate dehydrogenases and CO_2 reductases but possibly to tungsten-containing formate dehydrogenases and even Mo/W-containing formylmethanofuran dehydrogenases (which catalyze the first step in CO_2 assimilation by methanogenic bacteria). Development of a suitable expression system for the *P. atrosepticum* FdhF has been extremely difficult, owing to the extreme O_2-sensitivity of the enzyme and differences in the behavior of the recombinant expressions under anaerobic versus aerobic conditions. Still, we have recently made important progress along these lines, and have obtained significant levels of expression of functional protein. The UV/Visible absorption spectrum of oxidized FdhF agrees well with that expected from similar systems, and formate reduction results a significant bleaching throughout the visible, again as expected. This helps establish the minimal level of functionality for the enzyme, presently at least 50%, but possibly significantly greater depending on the equilibrium between Mo(IV) and oxidized [4Fe-4S] on the one hand and Mo(V) and reduced [4Fe-4S] on the other with the two-electron reduced FdhF generated on reaction with formate. The EPR spectrum of formate-reduced FdhF exhibits a clearly identifiable Mo(V) signal at liquid nitrogen temperatures. The goal of future work will be to increase the amount of active enzyme to attain higher Mo(V) levels so as to fully characterize the EPR signal and determine whether there is proton-coupled hyperfine structure. With sufficient amounts of active FdhF successfully purified and a method to maintain the activity after being taken out of the anaerobic chamber has been established, it will be possible to perform rapid-reaction kinetic work and eventually pursue XAS and

crystallographic studies. The stopped-flow experiments will be extremely useful in permitting a comparison of the kinetic parameters obtained, the k_{red} and $k_d^{formate}$, with the corresponding parameters for FdsDABG. Moreover, investigating kinetic isotope effects might also be interesting.

CHAPTER 8

Conclusions

8.1. Summary

In conclusion, studying FdsDABG, FdsBG from *C. necator* and FdhF from *P. atrosepticum* has provided valuable insight into the catalysis of formate to CO_2 as well as the reverse direction. Understanding their catalytic mechanism has crucial implications for addressing the pressing issue of climate crisis and possibly offering a solution for it. Analyzing the structure and function of these molybdenum-containing formate dehydrogenases has shed light on the number and orientation of cofactors, inactivation mechanisms, kinetic parameters and nature of transient molybdenum intermediates accumulating during reduction.

Investigating the reverse direction of catalysis has demonstrated that FdsDABG exclusively utilizes CO_2 as the substrate, and that bicarbonate can only be used after it is processed by carbonic anhydrase to generate CO_2. These findings challenge previously made claims that formate dehydrogenases are not able to catalyze the reverse reaction.

The pH dependence study revealed that acid/base catalysis does not have a notable contribution to the mechanism of the formate oxidation. This finding provides additional support for the direct hydride transfer mechanism rather than the attack of a hydroxyl group on molybdenum.

Exploring alternative ways to safeguard the enzyme from air-inactivation is an area of interest. This study has shown that superoxide dismutase is highly effective in protecting

FdsDABG in air and that the inactivation mechanism involves oxidation of the catalytically essential Mo=S sulfur to sulfite.

The electrochemical characterization of FdsDABG enzyme can provide key insight into understanding its electron transfer pathways and catalytic mechanisms. The cyclic voltametric work described here confirms the reversibility of formate to CO_2 conversion, again supporting a hydride transfer mechanism and the enzyme's ability to switch directions based on the system potential.

X-ray crystallography of FdsBG has yielded significant insight into the function of the subcomplex as well as the intact FdsDABG complex by yielding information on the orientation and distances of between the iron-sulfur clusters and the FMN cofactor. In addition, it has revealed details regarding the binding site of NAD^+/NADH.

Despite the challenges in expressing the enzyme owing to its extreme O_2-sensitivity, we have succeeded in obtaining a recombinant form of the *P. atrosepticum* FdhF in *E.* coli. Characterization of FdhF has provided valuable insight into the behavior of molybdenum-containing formate dehydrogenases and promises to be an extremely useful model for understanding the more complex FdsDABG system.

Our findings not only provide deeper insight into the intricate behavior of these formate dehydrogenases but also contribute to the broader field of catalysis. They have provided a promising amount of evidence for the proposed hydride transfer mechanism for these enzymes. Overall, this research has contributed to the development of bio-inspired catalysts and energy storage methods, providing promising avenues to pursue addressing the anthropogenic CO_2 emissions and advancing solutions for global warming.

8.2. Future directions

Future research in this field should focus on expanding the studies conducted with FdsDABG to include other molybdenum-containing formate dehydrogenases, such as FdhF from *E. coli* or FdhF from *P. atrosepticum*. These comparative studies will help verify and generalize the conclusions arrived in this work. Of particular interest is the study of the FdhF enzyme from *P. atrosepticum*, which shares similarities with FdsDABG, specifically having a cysteine coordinated to the molybdenum active site, but has a significantly simpler structure in that it contains only a single iron-sulfur cluster instead of seven as seen in FdsDABG.

It would also be intriguing to explore whether the FdsBG subcomplex, lacking the molybdenum active site, also generates superoxide. This investigation could uncover more on the specific role of the molybdenum center in superoxide production. In regard to FdhF, to conduct more detailed kinetic studies, it will be essential to successfully purify sufficient amounts of active FdhF for study and develop a method to maintain its activity outside the anaerobic chamber. This would enable a variety of rapid-reaction kinetic experiments, as well as the possibility of pursuing EPR, X-ray absorption spectroscopy (XAS) and crystallographic studies.

The application of stopped-flow kinetic approaches would be particularly valuable in comparing the kinetic parameters, such as k_{red} and $k_d^{formate}$ between different formate dehydrogenases, providing a comprehensive understanding of their catalytic behaviors, and investigating kinetic isotope effects could provide further insights into the mechanistic

details of the enzymatic reactions. Such work would offer a thorough understanding of the role of isotopic substitution in influencing reaction rates and pathways.

By addressing these future directions, we can improve our level of understanding of formate dehydrogenases and their potential applications, including the remediation of atmospheric CO_2 and thus tackling the ongoing global warming.

Chapter 9

References

Aitipamula, Srinivasulu, and Venu R. Vangala. 2017. "X-Ray Crystallography and Its Role in Understanding the Physicochemical Properties of Pharmaceutical Cocrystals." *Journal of the Indian Institute of Science* 97 (2): 227–43. https://doi.org/10.1007/s41745-017-0026 4.

Ali, Asif, Yi Wai Chiang, and Rafael M. Santos. 2022. "X-Ray Diffraction Techniques for Mineral Characterization: A Review for Engineers of the Fundamentals, Applications, and Research Directions." *Minerals* 12 (2): 205. https://doi.org/10.3390/min12020205.

Anet, Frank Al. 2004. "The Place of Metabolism in the Origin of Life." *Current Opinion in Chemical Biology* 8 (6): 654–59. https://doi.org/10.1016/j.cbpa.2004.10.005.

Bergmann, Justin, Esko Oksanen, and Ulf Ryde. 2022. "Combining Crystallography with Quantum Mechanics." *Current Opinion in Structural Biology* 72 (February): 18–26. https://doi.org/10.1016/j.sbi.2021.07.002.

Bernhardt, Harold S. 2012. "The RNA World Hypothesis: The Worst Theory of the Early Evolution of Life (except for All the Others)a." *Biology Direct* 7 (1): 23. https://doi.org/10.1186/1745-6150-7-23.

Bray, Robert C., and Graham N. George. 1985. "Electron-Paramagnetic-Resonance Studies Using Pre-Steady-State Kinetics and Substitution with Stable Isotopes on the Mechanism of Action of Molybdoenzymes." *Biochemical Society Transactions* 13 (3): 560–67. https://doi.org/10.1042/bst0130560.

Britannica, T. Editors of Encyclopaedia. "Bragg law." *Encyclopedia Britannica*, March 15, 2022. https://www.britannica.com/science/Bragg-law.

Brito, José A., and Margarida Archer. 2020. "Structural Biology Techniques: X-Ray Crystallography, Cryo-Electron Microscopy, and Small-Angle X-Ray Scattering." In *Practical Approaches to Biological Inorganic Chemistry*, 375–416. Elsevier. https://doi.org/10.1016/B978-0-444-64225-7.00010-9.

Brünger, Axel T. 1992. "Free R Value: A Novel Statistical Quantity for Assessing the Accuracy of Crystal Structures." *Nature* 355 (6359): 472–75. https://doi.org/10.1038/355472a0.

Butler, Colin. 2018. "Climate Change, Health and Existential Risks to Civilization: A Comprehensive Review (1989–2013)." *International Journal of Environmental Research and Public Health* 15 (10): 2266. https://doi.org/10.3390/ijerph15102266.

Chayen, Naomi E, and Emmanuel Saridakis. 2008. "Protein Crystallization: From Purified Protein to Diffraction-Quality Crystal." *Nature Methods* 5 (2): 147–53. https://doi.org/10.1038/nmeth.f.203.

Clegg, w., 1998. crystal structure determination, oxford university press.

Clegg, William, Alexander J Blake, Jacqueline M Cole, John S O Evans, Peter Main, Simon Parsons, and David J Watkin. 2009. *Crystal Structure Analysis*. Oxford University Press. https://doi.org/10.1093/acprof:oso/9780199219469.001.0001.

Finney, Alexander J., Rebecca Lowden, Michal Fleszar, Marta Albareda, Sarah J. Coulthurst, and Frank Sargent. 2019. "The Plant Pathogen *Pectobacterium Atrosepticum* Contains a Functional Formate Hydrogenlyase-2 Complex." *Molecular Microbiology* 112 (5): 1440–52. https://doi.org/10.1111/mmi.14370.

Friedrich, W., P. Knipping, and M. von Laue. "Sitzungsberichte der Math. Phys. Klasse (Kgl.), Bayerische Akademie der Wissenschaften." (1912): 303-322.

Gladyshev, Vadim N., Jeffrey C. Boyington, Sergei V. Khangulov, David A. Grahame, Thressa C. Stadtman, and Peter D. Sun. 1996. "Characterization of Crystalline Formate Dehydrogenase H from Escherichia Coli." *Journal of Biological Chemistry* 271 (14): 8095–8100. https://doi.org/10.1074/jbc.271.14.8095.

Govada, Lata, and Naomi Chayen. 2019. "Choosing the Method of Crystallization to Obtain Optimal Results." *Crystals* 9 (2): 106. https://doi.org/10.3390/cryst9020106.

Graham, Joel E., Dimitri Niks, Grant M. Zane, Qin Gui, Kellie Hom, Russ Hille, Judy D. Wall, and C. S. Raman. 2022. "How a Formate Dehydrogenase Responds to Oxygen: Unexpected O_2 Insensitivity of an Enzyme Harboring Tungstopterin, Selenocysteine, and [4Fe–4S] Clusters." *ACS Catalysis* 12 (16): 10449–71. https://doi.org/10.1021/acscatal.2c00316.

Griscom, Bronson W., Justin Adams, Peter W. Ellis, Richard A. Houghton, Guy Lomax, Daniela A. Miteva, William H. Schlesinger, et al. 2017. "Natural Climate Solutions." *Proceedings of the National Academy of Sciences* 114 (44): 11645–50. https://doi.org/10.1073/pnas.1710465114.

Hakopian, Sheron, Dimitri Niks, and Russ Hille. 2022. "The Air-Inactivation of Formate Dehydrogenase FdsDABG from Cupriavidus Necator." *Journal of Inorganic Biochemistry* 231 (June): 111788. https://doi.org/10.1016/j.jinorgbio.2022.111788.

Higgs, Paul G., and Niles Lehman. 2015. "The RNA World: Molecular Cooperation at the Origins of Life." *Nature Reviews Genetics* 16 (1): 7–17. https://doi.org/10.1038/nrg3841.

Hille, R., G. N. George, M. K. Eidsness, and S. P. Cramer. 1989. "EXAFS Analysis of Xanthine Oxidase Complexes with Alloxanthine, Violapterin, and 6-Pteridylaldehyde." *Inorganic Chemistry* 28 (21): 4018–22. https://doi.org/10.1021/ic00320a016.

Hille, Russ, James Hall, and Partha Basu. 2014. "The Mononuclear Molybdenum Enzymes." *Chemical Reviews* 114 (7): 3963–4038. https://doi.org/10.1021/cr400443z.

Hille, Russ, Takeshi Nishino, and Florian Bittner. 2011. "Molybdenum Enzymes in Higher Organisms." *Coordination Chemistry Reviews* 255 (9–10): 1179–1205. https://doi.org/10.1016/j.ccr.2010.11.034.

Hou, Hai, Miao Shi, Shan-Yang Hu, Fiaz Ahmad, Bin Zhang, Zhong-Hao Chen, and Da-Chuan Yin. 2019. "A Systematic Comparison of Sitting and Hanging-Drop Crystallization Using Traditional and Cross-Diffusion Microbatch Crystallization Plates." *Journal of Crystal Growth* 521 (September): 1–8. https://doi.org/10.1016/j.jcrysgro.2019.05.011.

Hu, Yilin, Aaron W. Fay, Chi Chung Lee, Janice Yoshizawa, and Markus W. Ribbe. 2008. "Assembly of Nitrogenase MoFe Protein." *Biochemistry* 47 (13): 3973–81. https://doi.org/10.1021/bi7025003.

Iobbi-Nivol, Chantal, and Silke Leimkühler. 2013. "Molybdenum Enzymes, Their Maturation and Molybdenum Cofactor Biosynthesis in Escherichia Coli." *Biochimica et Biophysica Acta (BBA) - Bioenergetics* 1827 (8–9): 1086–1101. https://doi.org/10.1016/j.bbabio.2012.11.007.

Jaskolski, Mariusz, Zbigniew Dauter, and Alexander Wlodawer. 2014. "A Brief History of Macromolecular Crystallography, Illustrated by a Family Tree and Its Nobel Fruits." *FEBS Journal* 281 (18): 3985–4009. https://doi.org/10.1111/febs.12796.

Jheeta, Sohan. 2017. "The Landscape of the Emergence of Life." *Life* 7 (2): 27. https://doi.org/10.3390/life7020027.

Kalimuthu, Palraj, Mélanie Petitgenet, Dimitri Niks, Stephanie Dingwall, Jeffrey R. Harmer, Russ Hille, and Paul V. Bernhardt. 2020. "The Oxidation-Reduction and Electrocatalytic Properties of CO Dehydrogenase from Oligotropha Carboxidovorans." *Biochimica et Biophysica Acta (BBA) - Bioenergetics* 1861 (1): 148118. https://doi.org/10.1016/j.bbabio.2019.148118.

Kammerer, S., I. Borho, J. Jung, and M. S. Schmidt. 2022. "Review: CO2 Capturing Methods of the Last Two Decades." *International Journal of Environmental Science and Technology*, December. https://doi.org/10.1007/s13762-022-04680-0.

Khosroabadi, Faezeh, Alireza Aslani, Kaveh Bekhrad, and Zahra Zolfaghari. 2021. "Analysis of Carbon Dioxide Capturing Technologies and Their Technology

Developments." *Cleaner Engineering and Technology* 5 (December): 100279. https://doi.org/10.1016/j.clet.2021.100279.

Kim, Sunghwan, Jie Chen, Tiejun Cheng, Asta Gindulyte, Jia He, Siqian He, Qingliang Li, et al. 2023. "PubChem 2023 Update." *Nucleic Acids Research* 51 (D1): D1373–80. https://doi.org/10.1093/nar/gkac956.

Kisker, Caroline, Hermann Schindelin, and Douglas C. Rees. 1997. "MOLYBDENUM-COFACTOR–CONTAINING ENZYMES: Structure and Mechanism." *Annual Review of Biochemistry* 66 (1): 233–67. https://doi.org/10.1146/annurev.biochem.66.1.233.

Kreß, Oliver, Manuel Gnida, Astrid M. Pelzmann, Christian Marx, Wolfram Meyer-Klaucke, and Ortwin Meyer. 2014. "Reversible Inactivation of CO Dehydrogenase with Thiol Compounds." *Biochemical and Biophysical Research Communications* 447 (3): 413–18. https://doi.org/10.1016/j.bbrc.2014.03.147.

Leimkühler, Silke. 2020. "The Biosynthesis of the Molybdenum Cofactors in *ESCHERICHIA COLI* ." *Environmental Microbiology* 22 (6): 2007–26. https://doi.org/10.1111/1462 2920.15003.

Mailloux, Nicholas A., Colleen P. Henegan, Dorothy Lsoto, Kristen P. Patterson, Paul C. West, Jonathan A. Foley, and Jonathan A. Patz. 2021. "Climate Solutions Double as Health Interventions." *International Journal of Environmental Research and Public Health* 18 (24): 13339. https://doi.org/10.3390/ijerph182413339.

Majumdar, Amit, and Sabyasachi Sarkar. 2011. "Bioinorganic Chemistry of Molybdenum and Tungsten Enzymes: A Structural–Functional Modeling Approach." *Coordination Chemistry Reviews* 255 (9–10): 1039–54. https://doi.org/10.1016/j.ccr.2010.11.027.

Mayr, Simon J., Ralf-R. Mendel, and Guenter Schwarz. 2021. "Molybdenum Cofactor Biology, Evolution and Deficiency." *Biochimica et Biophysica Acta (BBA) - Molecular Cell Research* 1868 (1): 118883. https://doi.org/10.1016/j.bbamcr.2020.118883.

McDowall, Jennifer S., Bonnie J. Murphy, Michael Haumann, Tracy Palmer, Fraser A. Armstrong, and Frank Sargent. 2014. "Bacterial Formate Hydrogenlyase Complex." *Proceedings of the National Academy of Sciences* 111 (38). https://doi.org/10.1073/pnas.1407927111.

Miralles-Robledillo, Jose María, Javier Torregrosa-Crespo, Rosa María Martínez-Espinosa, and Carmen Pire. 2019. "DMSO Reductase Family: Phylogenetics and Applications of Extremophiles." *International Journal of Molecular Sciences* 20 (13): 3349. https://doi.org/10.3390/ijms20133349.

Naidu, G S N, and T Panda. 1998. "Production of Pectolytic Enzymes ± a Review." *Bioprocess Engineering*.

Ngadze, Elizabeth, Carrie L. Brady, Teresa A. Coutinho, and Jacquie E. Van Der Waals. 2012. "Pectinolytic Bacteria Associated with Potato Soft Rot and Blackleg in South Africa and Zimbabwe." *European Journal of Plant Pathology* 134 (3): 533–49. https://doi.org/10.1007/s10658-012-0036-z.

Niks, Dimitri, Jayant Duvvuru, Miguel Escalona, and Russ Hille. 2016. "Spectroscopic and Kinetic Properties of the Molybdenum-Containing, NAD+-Dependent Formate Dehydrogenase from Ralstonia Eutropha." *Journal of Biological Chemistry* 291 (3): 1162–74. https://doi.org/10.1074/jbc.M115.688457.

Niks, Dimitri, and Russ Hille. 2019. "Molybdenum- and Tungsten-containing Formate Dehydrogenases and Formylmethanofuran Dehydrogenases: Structure, Mechanism, and Cofactor Insertion." *Protein Science* 28 (1): 111–22. https://doi.org/10.1002/pro.3498.

Okamoto, Ken, Teruo Kusano, and Takeshi Nishino. 2013. "Chemical Nature and Reaction Mechanisms of the Molybdenum Cofactor of Xanthine Oxidoreductase." *Current Pharmaceutical Design* 19 (14): 2606–14. https://doi.org/10.2174/1381612811319140010.

Ooi, Li-ling. 2010. *Principles of X-Ray Crystallography*. Oxford ; New York: Oxford University Press.

Panda, Preetinanda, Bhanupratap R. Vanga, Ashley Lu, Mark Fiers, Peter C. Fineran, Ruth Butler, Karen Armstrong, Clive W. Ronson, and Andrew R. Pitman. 2016. "Pectobacterium Atrosepticum and Pectobacterium Carotovorum Harbor Distinct, Independently Acquired Integrative and Conjugative Elements Encoding Coronafacic Acid That Enhance Virulence on Potato Stems." *Frontiers in Microbiology* 7 (March). https://doi.org/10.3389/fmicb.2016.00397.

Pearce, Ben K.D., Andrew S. Tupper, Ralph E. Pudritz, and Paul G. Higgs. 2018. "Constraining the Time Interval for the Origin of Life on Earth." *Astrobiology* 18 (3): 343–64. https://doi.org/10.1089/ast.2017.1674.

Petrov, N. I. 2021. "Synchrotron Mechanism of X-Ray and Gamma-Ray Emissions in Lightning and Spark Discharges." *Scientific Reports* 11 (1): 19824. https://doi.org/10.1038/s41598-021-99336-3.

Powell, Harold R. 2017. "X-Ray Data Processing." *Bioscience Reports* 37 (5): BSR20170227. https://doi.org/10.1042/BSR20170227.

Radon, Christin, Gerd Mittelstädt, Benjamin R. Duffus, Jörg Bürger, Tobias Hartmann, Thorsten Mielke, Christian Teutloff, Silke Leimkühler, and Petra Wendler. 2020. "Cryo-EM Structures Reveal Intricate Fe-S Cluster Arrangement and Charging in Rhodobacter

Capsulatus Formate Dehydrogenase." *Nature Communications* 11 (1): 1912. https://doi.org/10.1038/s41467-020-15614-0.

Rissa, Kati. 2002. "CHARACTERIZATION OF WATER-BASED BARRIER COATINGS." https://doi.org/10.13140/RG.2.2.12963.91681.
Roessler, Maxie M., and Enrico Salvadori. 2018. "Principles and Applications of EPR Spectroscopy in the Chemical Sciences." *Chemical Society Reviews* 47 (8): 2534–53. https://doi.org/10.1039/C6CS00565A.
Rowlands, Christopher C., and Damien M. Murphy. 1999. "EPR Spectroscopy, Theory." In *Encyclopedia of Spectroscopy and Spectrometry*, 445–56. Elsevier. https://doi.org/10.1006/rwsp.2000.0080.

Santos, Rafael M., and Reza Bakhshoodeh. 2021. "Climate Change/Global Warming/Climate Emergency versus General Climate Research: Comparative Bibliometric Trends of Publications." *Heliyon* 7 (11): e08219. https://doi.org/10.1016/j.heliyon.2021.e08219.

Schwarz, Günter, Ralf R. Mendel, and Markus W. Ribbe. 2009. "Molybdenum Cofactors, Enzymes and Pathways." *Nature* 460 (7257): 839–47. https://doi.org/10.1038/nature08302.

Shirokanev, A S, D V Kirsh, and A V Kupriyanov. 2019. "The Study of Effectiveness of a High-Performance Crystal Lattice Parametric Identification Algorithm Based on CUDA Technology." *Journal of Physics: Conference Series* 1368 (5): 052040. https://doi.org/10.1088/1742-6596/1368/5/052040.

Souza, Dulce H.F., Heloisa S. Selistre-de-Araujo, and Richard C. Garratt. 2000. "Determination of the Three-Dimensional Structure of Toxins by Protein Crystallography." *Toxicon* 38 (10): 1307–53. https://doi.org/10.1016/S0041-0101(99)00200-7.

Styring, P., J, D., de Conick, H., Reith, H., Armstrong, K., 2011. Carbon Capture and Utilization in the Green Economy. Centre for Low Carbon Futures.

Taylor, Garry. 2003. "The Phase Problem." *Acta Crystallographica Section D Biological Crystallography* 59 (11): 1881–90. https://doi.org/10.1107/S0907444903017815.

Teo, Boon-Keng. 1981. "Extended X-Ray Absorption Fine Structure (EXAFS) Spectroscopy: Techniques and Applications." In *EXAFS Spectroscopy*, edited by B. K. Teo and D. C. Joy, 13–58. Boston, MA: Springer US. https://doi.org/10.1007/978-1-4757-1238-4_3.

Thomas, John Meurig. 2012. "The Birth of X-Ray Crystallography." *Nature* 491 (7423): 186–87. https://doi.org/10.1038/491186a.

Thompson, Lonnie G. n.d. "Climate Change: The Evidence and Our Options." *CLIMATE CHANGE*.

Vlaic, Gilberto, and Luca Olivi. 2004. "EXAFS Spectroscopy: A Brief Introduction." *Croat. Chem. Acta*.

Weiss, Madeline C., Filipa L. Sousa, Natalia Mrnjavac, Sinje Neukirchen, Mayo Roettger, Shijulal Nelson-Sathi, and William F. Martin. 2016. "The Physiology and Habitat of the Last Universal Common Ancestor." *Nature Microbiology* 1 (9): 16116. https://doi.org/10.1038/nmicrobiol.2016.116.

Weiss, Madeline C., Martina Preiner, Joana C. Xavier, Verena Zimorski, and William F. Martin. 2018. "The Last Universal Common Ancestor between Ancient Earth Chemistry and the Onset of Genetics." Edited by Mark Achtman. *PLOS Genetics* 14 (8): e1007518. https://doi.org/10.1371/journal.pgen.1007518.

Wlodawer, Alexander, Wladek Minor, Zbigniew Dauter, and Mariusz Jaskolski. 2008. "Protein Crystallography for Non-Crystallographers, or How to Get the Best (but Not More) from Published Macromolecular Structures: Protein Crystallography for Non-Crystallographers." *FEBS Journal* 275 (1): 1–21. https://doi.org/10.1111/j.1742-4658.2007.06178.x.

Wlodawer, Alexander, Wladek Minor, Zbigniew Dauter, and Mariusz Jaskolski. 2013. "Protein Crystallography for Aspiring Crystallographers or How to Avoid Pitfalls and Traps in Macromolecular Structure Determination." *FEBS Journal* 280 (22): 5705–36. https://doi.org/10.1111/febs.12495.

Wu, Hao Bin, and Xiong Wen (David) Lou. 2017. "Metal-Organic Frameworks and Their Derived Materials for Electrochemical Energy Storage and Conversion: Promises and Challenges." *Science Advances* 3 (12): eaap9252. https://doi.org/10.1126/sciadv.aap9252.

Yano, Junko, and Vittal K. Yachandra. 2009. "X-Ray Absorption Spectroscopy." *Photosynthesis Research* 102 (2–3): 241–54. https://doi.org/10.1007/s11120-009-9473-8.

Young, Tynan, Dimitri Niks, Sheron Hakopian, Timothy K. Tam, Xuejun Yu, Russ Hille, and Gregor M. Blaha. 2020. "Crystallographic and Kinetic Analyses of the FdsBG Subcomplex of the Cytosolic Formate Dehydrogenase FdsABG from Cupriavidus Necator." *Journal of Biological Chemistry* 295 (19): 6570–85. https://doi.org/10.1074/jbc.RA120.013264.

Yu, Xuejun, Dimitri Niks, Ashok Mulchandani, and Russ Hille. 2017. "Efficient Reduction of CO2 by the Molybdenum-Containing Formate Dehydrogenase from Cupriavidus

Necator (Ralstonia Eutropha)." *Journal of Biological Chemistry* 292 (41): 16872–79. https://doi.org/10.1074/jbc.M117.785576.

Yu, Xuejun, Dimitri Niks, Xin Ge, Haizhou Liu, Russ Hille, and Ashok Mulchandani. 2019. "Synthesis of Formate from CO_2 Gas Catalyzed by an O_2-Tolerant NAD-Dependent Formate Dehydrogenase and Glucose Dehydrogenase." *Biochemistry* 58 (14): 1861–68. https://doi.org/10.1021/acs.biochem.8b01301.